SISSA ISAS

SCUOLA INTERNAZIONALE SUPERIORE DI STUDI AVANZATI
INTERNATIONAL SCHOOL FOR ADVANCED STUDIES

Large Scale First-Principles Simulations of Water and Ammonia at High Pressure and Temperature

Thesis submitted for the degree of
"Doctor Philosophiæ"

CANDIDATE
Carlo Cavazzoni

SUPERVISORS
Dr. Guido L. Chiarotti
Dr. Sandro Scandolo

October 1998

This thesis is available on the Web at the URL: http://www.sissa.it/cm/thesis/1998/

a Roberta ed ai miei genitori

Contents

1 Introduction **1**

2 Theory **5**

2.1 Parrinello–Rahman Molecular Dynamics 5

2.2 Car–Parrinello Molecular Dynamics 9

2.3 Constant Pressure *Ab initio* Molecular Dynamics 11

3 Parallel Implementation of CP algorhitm. **15**

3.1 Reciprocal space representation 16

3.2 Parallelization strategy 19

3.3 Data distribution 25

3.4 The FFT routine 28

3.5 Orthogonalization 31

4 Water and Ammonia **35**

4.1 Ammonia 40

4.2 Water 55

4.3 Planetary Physics 70

5 Conclusions **73**

6 Appendix **77**

6.1 Orthogonalization and Parallel Diagonalization 77

6.2 Code benchmarks 82

6.3 Forces and Stress. 85

List of Figures

3.1 CP Flow chart 20
3.2 Code structure 23
3.3 $\mathbf{G}$ vectors distribution 27
3.4 Real space grid distribution 28
3.5 Communications Flow chart 29
3.6 FFT implementation 32

4.1 Neptune 37
4.2 Ammonia IV 41
4.3 Ammonia Experimental PT 42
4.4 Ammonia IV structure factor 44
4.5 Ammonia EOS 300K 45
4.6 Ammonia Bond symmetrization 46
4.7 Superionic Ammonia: MSD 49
4.8 Ammonia Phase Diagram 54
4.9 Conductivity 55
4.10 Water ice X structure 57
4.11 Order parameter 59
4.12 Density of Hydrogens 61
4.13 O-O and O-H pair correlation functions at 300 GPa 63

4.14 O-O pair correlation functions at 150 GPa 64
4.15 O-O pair correlation functions at 300 GPa 65
4.16 Water Phase Diagram 66
4.17 Water Kohn-Sham states 68
4.18 Water DOS 69
4.19 Planetary equations of state 71

6.1 Diagonalization routine 80
6.2 Diagonalization routine speed-up 81
6.3 Code benchmark 83
6.4 Code speed-up 84
6.5 New Code benchmark 86
6.6 New Code Speed-Up 87

Chapter 1

Introduction

In the last years the behavior of simple molecular systems at high pressures and temperatures has become increasingly attractive, thanks to the development of new experimental and theoretical tools. Numerous shock-wave and diamond anvil cell experiments have been carried out on these systems, and many observed phenomena still lack a theoretical explanation. Moreover, pressures and temperatures reached in the laboratory are now comparable to those of the planetary deep interiors, and the interplay between high-pressure and planetary physics is, therefore, increasing. On the theoretical side, *ab initio* techniques are now extremely effective in determining structural properties and phase transitions of molecular and other systems at high pressure. Among others, constant pressure *ab initio* molecular dynamics, a recently developed computational scheme combining Car-Parrinello (CP) and Parrinello-Rahman (PR)

molecular dynamics, has been shown to be quite accurate and predictive. This scheme borrows from PR the idea of treating the edges of the molecular dynamics simulation cell as additional degrees of freedom, and from CP the quantomechanical calculation of the internal stress driving the cell as to equilibrate the external pressure (introduced here as a parameter). This allows phase transitions to take place even during the short time scales of *ab initio* simulations.

In this thesis we present results of extensive constant pressure *ab initio* molecular dynamics simulations of water and ammonia at high pressures and temperatures. New superionic, ionic and metallic phases will be presented and characterized, and their possible consequences on planetary physics discussed.

Water and ammonia, together with hydrogen and methane, are the most abundant simple molecules in the universe. They are largely present especially in the interiors of the giant planets. Two planets in the solar system, Uranus and Neptune, are supposed to be composed mainly of a mixture of water, ammonia and methane (also called “ices”); the properties of these planets are therefore linked to the behavior of these molecules in the ranges of pressures and temperatures typical of their interiors (T: 2000-8000 K, P: 20-800 GPa). The simulations of water and ammonia in these conditions are precisely aimed to study the properties relevant for planetary physics, like electrical conductivity and density. In this regard, the present work is the natural extension of a recent theoretical study of methane, the other component of ices. Using constant pressure *ab initio* molecular dynamics, Ancilotto *et al.* [1] have shown that, inside Neptune, methane dissociates into hydrocarbons of higher molecular weight, suggesting that this could be the source of the anomalous atmospheric abundance of ethane observed by the Voyager II spacecraft.

While the structure of solid water at high pressure has been extensively stud-

ied both theoretically and experimentally, the structure of solid ammonia is still not known above a few GPa. We performed simulations at high pressures and room temperature of ammonia to individuate possible new solid structures. In particular the possibility of a symmetric hydrogen bond phase has been investigated.

The work presented in this thesis was made possible by the design and the implementation of an architecture-free parallel code, able to exploit the computational power of modern massively parallel computers, which use is mandatory for intensive *ab initio* simulations of large systems.

In Chapter 2 I give a brief review of the Constant Pressure *ab initio* Molecular Dynamics, together with the key ideas of the original Parrinello-Rahman and Car-Parrinello Molecular Dynamics methods. In Chapter 3 the main features of the parallel implementation of the code are presented. In Chapter 4 the results of the simulations on water and ammonia are presented and discussed with particular attention to their implications on the physics of Uranus and Neptune. Finally, in Chapter 5 conclusions are outlined. An appendix follows with some benchmarks of the code on different architectures.

Chapter 2

Theory

Constant pressure *ab initio* Molecular Dynamics, used in this work to simulate water and ammonia systems, is a theoretical scheme recently introduced by Focher *et al.* [2, 3] that extends the well-known Car–Parrinello [4] method including the Parrinello–Rahman [5] scheme for molecular dynamics. In this chapter we briefly review, as in the original work of Focher *et al.* [3], first the Parrinello–Rahman and the Car–Parrinello molecular dynamics schemes, and then the Constant Pressure *ab initio* Molecular Dynamics.

2.1 Parrinello–Rahman Molecular Dynamics

The Parrinello–Rahman method (PR) is the natural extension of Andersen [6] molecular dynamics. In the original Andersen method the simulation cell is allowed to change its size *isotropically*, by equilibrating the calculated internal

pressure to an assigned value representing the external pressure. This is done by introducing the volume of the cell as a new dynamical variable, still preserving the periodic boundary conditions. In the PR method, the cell can change, more generally, both its shape and its size. This is done, according to PR, in the following way.

Let us consider a generic simulation cell for Molecular Dynamics (MD), which fill all the space by repeating it at infinity with periodic boundary conditions. The MD cell is described by the three primitive Bravais vectors $(\mathbf{a}, \mathbf{b}, \mathbf{c})$. Defining the matrix

$$\mathbf{h} = (\mathbf{a}, \mathbf{b}, \mathbf{c}) \tag{2.1}$$

(where the vectors constitute the columns of the matrix), the real space position of a generic particle in the box, **R**, can be written as:

$$\mathbf{R} = \mathbf{h}\mathbf{S}, \tag{2.2}$$

S being the vector of the so called *scaled* coordinates of the particle, whose components assume values between 0 and 1 inside the cell. (In other words, in the scaled variable space, the cell is always a cube of side 1.) The relation between distances in real and in scaled coordinates will be determined by the metric tensor $\mathbf{G} = \mathbf{h}^t\mathbf{h}$, so that:

$$(\mathbf{R}_i - \mathbf{R}_j)^2 = (\mathbf{S}_i - \mathbf{S}_j)^t\mathbf{G}(\mathbf{S}_i - \mathbf{S}_j). \tag{2.3}$$

Since we want the cell to change in time, the basic idea of the PR method, in analogy with Andersen dynamics, is to consider an *extended* Lagrangian system, where the nine components of the matrix $\mathbf{h}$ are classical degrees of freedom, whose trajectories are determined by appropriate generalized forces. This

is obtained by writing the Lagrangian L of the extended system as:

$$L = \frac{1}{2}\sum_{i=1}^{N} M_i(\dot{\mathbf{S}}^t \mathbf{G}\dot{\mathbf{S}}_i) - V(\mathbf{R}_1, ..., \mathbf{R}_N) + \frac{1}{2}W\mathrm{Tr}(\dot{\mathbf{h}}^t\dot{\mathbf{h}}) - p\Omega, \tag{2.4}$$

where M_i is the mass of i-th particle, V the inter-particle potential, W an inertia parameter controlling the cell motion, p the external pressure, and $\Omega = \det \mathbf{h}$ the volume of the simulation cell.

The first two terms of Eq. 2.4 define the Lagrangian for the usual fixed cell molecular dynamics. Note however that when the cell varies in time, the kinetic energy term in Eq. 2.4 does not correspond to the actual kinetic energy of the particles in the real system.

The Euler-Lagrange equations of motion derived from Eq. 2.4 are:

$$\ddot{\mathbf{S}}_i^\alpha = -\frac{1}{M_i}\frac{\partial V}{\partial \mathbf{R}_i^\beta}\left(\mathbf{h}^t\right)^{-1}_{\beta\alpha} - \mathbf{G}^{-1}_{\alpha\beta}\dot{\mathbf{G}}_{\beta\gamma}\dot{\mathbf{S}}_i^\gamma, \tag{2.5}$$

$$\ddot{\mathbf{h}}_{\alpha\beta} = \frac{1}{W}\left(\Pi_{\alpha\gamma} - p\delta_{\alpha\gamma}\right)\Omega\left(\mathbf{h}^t\right)^{-1}_{\gamma\beta}, \tag{2.6}$$

where:

$$\Pi_{\alpha\gamma} = \frac{1}{\Omega}\left(\sum_i M_i \mathbf{v}_i^\alpha \mathbf{v}_i^\gamma - \frac{\partial V}{\partial \mathbf{h}_{\alpha\delta}}\mathbf{h}^t_{\delta\gamma}\right) \tag{2.7}$$

and

$$\mathbf{v}_i^\alpha = \mathbf{h}_{\alpha\gamma}\dot{\mathbf{S}}_i^\gamma \tag{2.8}$$

(Greek indices indicate the components of vectors and matrices, and the convention of implicit sum over repeated indices is assumed). Interpreting $M_i\mathbf{v}_i$ as the momentum of i-th particle, it can be shown [3] that Π coincides with the stress tensor.

$$\frac{\partial V}{\partial \mathbf{h}}\mathbf{h}^t = \frac{\partial V}{\partial \epsilon}. \tag{2.9}$$

The time variation of the cell matrix $\mathbf{h}$ (Eq. 2.6) is driven by the imbalance between the external pressure p (a fix parameter of the simulation) and the instantaneous value of the stress tensor (Π).

The Lagrangian (Eq. 2.4) is conservative with the constant of motion given by:

$$H = \frac{1}{2}\sum_i M_i \mathbf{v}_i^2 + V(\mathbf{R}_1, ..., \mathbf{R}_N) + \frac{1}{2} W \mathrm{Tr}(\dot{\mathbf{h}}^t \dot{\mathbf{h}}). \tag{2.10}$$

Physically $\langle H \rangle$ corresponds to the enthalpy of the system [7], apart for the last term, which becomes negligible for large N.

The key point of the above scheme [8, 6] is that trajectories generated with the PR dynamics give averages of thermodynamical quantities that are equivalent, in the thermodynamical limit, to Gibbs averages in the (H,p,N) statistical ensemble, i.e. the ensemble where enthalpy, pressure and number of particles are fixed.

The parameter W in the equations is related to the *inertia* of $\mathbf{h}$. It is clear that W does not influence equilibrium properties. For an optimal choice of W (i.e. faster equilibration of the combined cell and ions system) Andersen has suggested that W should be tuned so as to obtain a relaxation time of the cell of the order of $\tau = L/c$, where L is the linear dimension of the cell and c the sound velocity of the system. One can estimate the characteristic frequency of the cell by linearizing Eq. 2.6. Assuming this frequency to be roughly $1/\tau$, one obtains [7]: $W = 3\sum_i M_i / 4\pi^2$.

Additional comments on the applicability of the method can be found in Ref. [9].

2.2 Car–Parrinello Molecular Dynamics

The Car–Parrinello method (CP) [4, 10, 11] is a very elegant and powerful scheme for *ab initio* MD simulations, successfully used in the last years in a wide variety of problems otherwise inaccessible to standard simulation methods (see, for example, Ref. [12] and references therein). In the CP method the forces acting on the atoms are not calculated from a parameter-dependent potential — usually determined via an empirical *ad hoc* procedure — but from the full quantum treatment of the electronic system, based on Density Functional Theory (DFT) [13, 14, 15]. This is done by introducing a *fictitious* dynamical system, associated with the *physical* system, whose potential energy surface E is an appropriate functional of both ionic and electronic degrees of freedom, with electronic wave-functions treated as classical fields. The fictitious system is devised in such a way that the ionic trajectories generated by its dynamics reproduce very closely those of the physical system in the Born–Oppenheimer (BO) approximation, that is in the approximation where the energy surface V for the atomic dynamics is defined by

$$V(\{\mathbf{R}_I\}) = \min_{\{\psi_i\}} E\left[\{\psi_i\}, \{\mathbf{R}_I\}\right]. \tag{2.11}$$

The generalized classical Lagrangian of the fictitious system is defined as:

$$\begin{aligned} L &= \mu \sum_i^{occ} \int d\mathbf{r} \left|\dot{\psi}_i(\mathbf{r})^2\right| + \frac{1}{2}\sum_I M_I \dot{\mathbf{R}}_I^2 - E\left[\{\psi_i\}, \{\mathbf{R}_I\}\right] \\ &\quad + \sum_{ij} \Lambda_{ij}\left(\int d\mathbf{r}\psi_i^*(\mathbf{r})\,\psi_j(\mathbf{r}) - \delta_{ij}\right), \end{aligned} \tag{2.12}$$

L depends on the ionic positions $\mathbf{R}_I$ and electronic wave-functions ψ_i. The parameter μ (of units mass $\times$ length^2) is a generalized mass for the electronic degrees of freedom. The sums over i and j are taken on the occupied electronic states, and the sum over I on the ions. The first and second term in Eq. 2.12 are

the (classical) kinetic energy of the electronic and ionic degrees of freedom; E, given by the DFT total energy functional, is the potential energy of the coupled electron–ion fictitious system. Λ_{ij} are Lagrangian multipliers associated with the orthonormalization constraints of the wave-functions[1]. The Euler–Lagrange equations of motion derived from Eq. 2.12 are:

$$\mu\ddot{\psi}_i(\mathbf{r}) = -\frac{\delta E}{\delta \psi_i^*(\mathbf{r})} + \sum_j \Lambda_{ij}\psi_j(\mathbf{r}), \tag{2.13}$$

$$\ddot{\mathbf{R}}_I = -\frac{1}{M_I}\frac{\partial E}{\partial \mathbf{R}_I}. \tag{2.14}$$

In general, the ionic trajectories generated by Eq. 2.14 and those obtained by:

$$\ddot{\mathbf{R}}_I = -\frac{1}{M_I}\frac{\partial V\left(\{\mathbf{R}_I\}\right)}{\partial \mathbf{R}_I}, \tag{2.15}$$

do not coincide, unless $E\left[\{\psi_i\}, \{\mathbf{R}_I\}\right]$ is fully minimized with respect to $\{\psi_i\}$ (see Eq. 2.11). However, the *mass* μ and the initial conditions on the wave-functions can be chosen in such a way that the dynamics of the electronic degrees of freedom is much faster than that of the ions, allowing the electrons, initially lying on the BO surface, to follow adiabatically the ionic motion remaining close to the instantaneous ground state. If this condition for the adiabatic motion is satisfied, the instantaneous value of the forces acting on the ions does not exactly coincide with the Hellmann–Feynman forces, but their *average* value does to a very high degree of accuracy [16, 12].

Although entirely classical, the fictitious dynamics of the electronic wave-functions accounts for the properties of the quantum eigenvalue spectrum of the electrons. It has been shown [17] that for small deviations from the ground state, the dynamics of the wave-functions can be well described as a superposition of

[1]The Lagrangian in Eq. 2.12 is correct for a system where the occupied electronic states are described by a set of mutually orthogonal wave-functions.

oscillations whose frequency is given by:

$$\omega_{ij} = \left(\frac{2(\epsilon_j - \epsilon_i)}{\mu} \right)^{\frac{1}{2}}, \tag{2.16}$$

where ϵ_j and ϵ_i are the eigenvalue of an empty and an occupied state respectively. From Eq. 2.16 one gets that the lowest characteristic frequency for the electronic degrees of freedom is: $\omega_{\min} = (2E_g/\mu)^{\frac{1}{2}}$, where E_g is the energy gap.

Since the condition for the adiabatic separation of electronic and ionic degrees of freedom is that $\omega_{\min}$ is much higher than the highest ionic frequency, the CP method works well, with a proper choice of parameter μ, for systems with a clearly defined single-particle gap, like semiconductors and insulators. The use of CP for metals is more subtle due to an irreversible transfer of energy between ions and electrons [17, 12, 3]. To overcome this problem the use of two different Nosé [18] thermostats has been proposed [19]: one coupled to the ions, to keep them at the desired temperature, and the other to the electronic wave-functions, to keep them "cold", which means close to the BO surface.

2.3 Constant Pressure *Ab initio* Molecular Dynamics

In this section we present the recent extension, introduced by Focher *et al.* [3], of the Parrinello–Rahman method to the case of Car–Parrinello *ab initio* MD described above.

In Ref. [3] a new classical Lagrangian is introduced where the degrees of freedom are the scalar fields ψ (not explicitly dependent on $\mathbf{h}$) associated to the electrons, the scaled ionic coordinates $\mathbf{S}$ and the cell matrix $\mathbf{h}$. This Lagrangian preserves the physical meaning of the PR equations of motion, and reduces to the original CP Lagrangian (Eq. 2.12) in the fixed cell case. This was obtained by substituting the original wave-functions $\psi_h(\mathbf{r})$ (where the lower index h now

indicates a wave-function defined and normalized on the cell generated by $\mathbf{h}$) with new wave-functions ψ defined onto the scaled variable space $\mathbf{s} = \mathbf{h}^{-1}\mathbf{r}$ (normalized on the unitary cube):

$$\psi_h(\mathbf{r}) = \frac{1}{\sqrt{\Omega}}\psi(\mathbf{h}^{-1}\mathbf{r}) = \frac{1}{\sqrt{\Omega}}\psi(\mathbf{s}), \tag{2.17}$$

where the prefactor $1/\sqrt{\Omega}$ preserves the normalization. As required $\psi(\mathbf{s})$ is independent on $\mathbf{h}$. From Eq. 2.17 we obtain the transformation law for the electronic charge density, which appears in the DFT energy functional (see Eq. 3.1 in the next section):

$$\rho_h(\mathbf{r}) = \frac{1}{\Omega}\rho(\mathbf{h}^{-1}\mathbf{r}). \tag{2.18}$$

This choice for the transformation of the wave-functions corresponds to consider that the only *direct* effect of the deformation of the cell on the wave-functions and on the electronic density in real space is a "stretching" of them, in order to satisfy the changed boundary conditions.

The new Lagrangian can be written as:

$$\begin{aligned} L &= \mu \sum_i \int d\mathbf{s}\, |\dot{\psi}_i(\mathbf{s})|^2 + \frac{1}{2}\sum_I M_I(\dot{\mathbf{S}}_I^t \mathbf{G} \dot{\mathbf{S}}_I) - E\left[\{\psi_i\}, \{\mathbf{h}\mathbf{S}_I\}\right] + \\ &\quad \sum_{ij} \Lambda_{ij}\left(\int d\mathbf{s}\, \psi_i^*(\mathbf{s})\psi_j(\mathbf{s}) - \delta_{ij}\right) + \frac{1}{2} W \mathrm{Tr}(\dot{\mathbf{h}}^t \dot{\mathbf{h}}) - p\Omega, \end{aligned} \tag{2.19}$$

where the integrals are taken on the scaled cell (of volume $\Omega_0 = 1$). Notice that if the cell is kept fixed, Eq. 2.19 reduces to the original CP Lagrangian (Eq. 2.12), written for the scaled wave-functions, apart for the constant term $p\Omega$. From Eq. 2.17 the integrals in the first and fourth term of Eq. 2.19 are, in fact, invariant under scale transformation:

$$\int_{\Omega_0} \psi^*(\mathbf{s})\psi(\mathbf{s}) d\mathbf{s} = \Omega \int_{\Omega_0} \psi_h^*(\mathbf{h}\mathbf{s})\psi_h(\mathbf{h}\mathbf{s}) d\mathbf{s} = \int_{\Omega} \psi_h^*(\mathbf{r})\psi_h(\mathbf{r}) d\mathbf{r}. \tag{2.20}$$

Notice also that using the scaled wave-functions, in the kinetic term (first term of Eq. 2.19) the contribution due to the deformation of the cell is neglected

(exactly in the same way as in Eq. 2.4). This ensures that the equations of motion for the electronic wave-functions are formally the same of the original CP scheme (Eq. 2.13). The equations for the ionic degrees of freedom have exactly the same form as in the PR case (see Eq. 2.5), with the replacement of the classical forces $-\partial V/\partial \mathbf{R}$ by $-\partial E/\partial \mathbf{R}$, which give, as in Eq. 2.14, the actual quantum-mechanical forces acting on the ions [16]. The independence of the integrals in Eq. 2.19 on $\mathbf{h}$ ensures also that no extra terms with respect to Eq. 2.6 appear in the equations for the cell parameters. Here in the tensor Π (Eq. 2.7) $\partial V/\partial \mathbf{h}$ is replaced by $\partial E/\partial \mathbf{h}$:

$$\Pi_{\alpha\gamma} = \frac{1}{\Omega}\left(\sum_i M_i \mathbf{v}_i^\alpha \mathbf{v}_i^\gamma - \frac{\partial E}{\partial \mathbf{h}_{\alpha\delta}}\mathbf{h}^t_{\delta\gamma}\right). \tag{2.21}$$

In the original work of Focher *et al.* [3] it is also shown that the term $(\partial E/\partial \mathbf{h})\mathbf{h}^t$ is the actual quantum-mechanical stress tensor [20, 21]. For this reason, this extension of the PR dynamics in the CP *ab initio* scheme is physically meaningful.

All the equations of motion derived from the Lagrangian in Eq. 2.19 can be formally written as:

$$\mu\ddot{\psi}_i(\mathbf{s}) = -\frac{\delta E}{\delta \psi_i^*(\mathbf{s})} + \sum_j \Lambda_{ij}\psi_j(\mathbf{s}), \tag{2.22}$$

$$\ddot{\mathbf{S}}_i^\alpha = -\frac{1}{M_i}\frac{\partial E}{\partial \mathbf{R}_i^\beta}\left(\mathbf{h}^t\right)^{-1}_{\beta\alpha} - \mathbf{G}^{-1}_{\alpha\beta}\dot{\mathbf{G}}_{\beta\gamma}\dot{\mathbf{S}}_i^\gamma, \tag{2.23}$$

$$\ddot{\mathbf{h}}_{\alpha\beta} = \frac{1}{W}\left(\Pi_{\alpha\gamma} - p\delta_{\alpha\gamma}\right)\Omega\left(\mathbf{h}^t\right)^{-1}_{\gamma\beta}. \tag{2.24}$$

The next chapter is devoted to the description of the implementation of a parallel code in which equations 2.22–2.24 are integrated in time.

Chapter 3

Parallel Implementation of CP algorhitm.

It is well known that *ab initio* molecular dynamics simulations of large systems, such as those presented in this work, are computationally demanding in terms of both memory and CPU time. Today such a computational power is available only on massively parallel computers. To exploit these facilities a parallelization of the codes implementing molecular dynamics algorithms is then required. This porting is not as simple as that between two different scalar computers, because optimization of communications and data distribution imply often a change in the logic flow of the code. In most cases numerical algorithms have to be rewritten.

One of the main achievements of this work is the implementation of an architecture-free parallel version of the SISSA CP code, which contains a constant

pressure variable cell *ab initio* MD as described in the previous chapter and in Ref. [3]. In this chapter we will describe briefly the structure and the characteristics of the new parallel version, while speed-up performance and benchmarks on different architectures are reported in Appendix 6.2.

3.1 Reciprocal space representation

As explained in the previous chapter in the Car-Parrinello molecular dynamics, interactions between ions are calculated through *ab initio* density functional theory (DFT). In the local density approximations (LDA) the energy E of an interacting ionic and electronic system is written as :

$$E\left[\{\psi_i\},\{\mathbf{R}_I\}\right] = \sum_i^{\mathrm{occ}} f_i \int d\mathbf{r}\psi_i^*(\mathbf{r})\left(-\frac{1}{2}\nabla^2 + V_{\mathrm{nl}}^{\mathrm{ps}}\right)\psi_i(\mathbf{r}) + \tag{3.1}$$

$$\int d\mathbf{r} V_{\mathrm{l}}^{\mathrm{ps}}(\mathbf{r})\rho_e(\mathbf{r}) + \frac{1}{2}\int d\mathbf{r}d\mathbf{r}'\frac{\rho_e(\mathbf{r})\rho_e(\mathbf{r}')}{|\mathbf{r}-\mathbf{r}'|} + E_{xc}[\rho_e] + \sum_{I\neq J}\frac{Z_v^2}{|\mathbf{R}_I-\mathbf{R}_J|},$$

where: $\psi_i(\mathbf{r})$ are the Kohn-Sham orbitals, $\mathbf{R}_I$ is the vector position of ion I, $V_{\mathrm{nl}}^{\mathrm{ps}}$ and $V_{\mathrm{l}}^{\mathrm{ps}}$ are the non-local and local ionic potentials respectively; $\rho_e(\mathbf{r}) = \sum_i f_i |\psi_i(\mathbf{r})|^2$ is the electronic charge density, f_i the occupation numbers of electronic states, Z_v is the valence charge density of the atoms, and E_{xc} the exchange-correlation energy functional. Periodic boundary conditions allow the expansion of the electronic wave-functions in plane-waves. As a consequence, considering the Γ-point representation of the Brillouin zone (which will be our practical choice), a generic wave-function is written as:

$$\psi_h(\mathbf{r}) = \frac{1}{\sqrt{\Omega}}\sum_{\mathbf{G}} c_h(\mathbf{G})e^{i\mathbf{G}\cdot\mathbf{r}}, \tag{3.2}$$

where Ω is the volume of the simulation cell, $\mathbf{G}$ the reciprocal lattice vectors, and $c_h(\mathbf{G})$ the coefficient of the plane-waves expansion. The basis set for the

expansion in 3.2 is reduced to a finite set by truncating the sum over $\mathbf{G}$ to include only those plane-waves with a kinetic energy $K = \frac{1}{2}\mathbf{G}^2$ less than a given energy E_c. It is clear that the choice of E_c determines the accuracy of the calculation of the DFT energy. In the present case we are interested in performing calculation of the DFT energy while the simulation cell varies in shape and size. A fixed value of E_c along the simulation would imply that the size of the plane-waves basis set also changes. In the Car-Parrinello method, however, the plane-wave coefficients $c_h(\mathbf{G})$ are the actual Lagrangian electronic degrees of freedom, and their number cannot be varied during the simulation. The fact that the number of wave-functions is no more consistent with a fixed E_c constitutes a source of error. As explained in Ref. [3] this problem has been however solved by modifying the kinetic energy factor G^2 in equations 3.3 in order to force zero occupancy for those plane-waves whose kinetic energy exceeds E_c [22]. This is done by adding to G^2 a smooth step function of height A and width σ, so that:

$$G^2 = G^2 + A[1 + \mathrm{erf}(\frac{G^2/2 - E_0}{\sigma})].$$

In the $A \to 0$ limit, the constant number of plane-waves results are recovered. In the opposite $\sigma \to 0$, $A \to \infty$ limit, all waves with $\frac{1}{2}G^2 > E_0$ drop out from the ground-state wave-function, therefore mimicking a constant E_c. The optimum practical choice lies somewhere in between these two extrema, since one would like to work as close as possible to the constant E_c, while avoiding unphysical discontinuities. Making $A > 0$ introduce an additional term in the stress tensor, which corresponds, in the large-A limit case, to the so called Pulay stress [23] (difference between the stress tensor $\partial E/\partial h$, and the "true" constant cut-off stress). For more details we refer to Ref. [3].

Expression 3.1, shows that some terms are diagonal in reciprocal space and

others are diagonal in real space, therefore computational resources could be saved calculating each quantity in the space where it is diagonal. This is the strategy adopted in our CP algorithm, where a fast Fourier transform (FFT) is used to transform quantities between the two spaces.

Substituting 3.2 into those terms of 3.1 which are diagonal in the reciprocal space one obtains:

$$E = E_{ke} + E_{xc} + E^{ps}_{loc} + E^{ps}_{nl} + E_H + E_{sr} - E_{self},$$

with

$$\begin{aligned}
E_{ke} &= \frac{1}{2}\sum_{i}^{N_b} f_i \sum_{\mathbf{G}} \mathbf{G}^2 c_i^*(\mathbf{G}) c_i(\mathbf{G}), \\
E_{xc} &= \int d\mathbf{r} \epsilon_{xc}(\rho_e(\mathbf{r}))\rho_e(\mathbf{r}), \\
E^{ps}_{loc} &= \Omega \sum_{\mathbf{G}} \rho_e^*(\mathbf{G}) S(\mathbf{G}) v_{loc}(|\mathbf{G}|), \\
E^{ps}_{nl} &= \sum_{I=1}^{N}\sum_{i=1}^{N_b}\sum_{l,m} f_i \alpha_{l,m} \left|F^{l,m}_{I,i}\right|^2, \\
E_H &= \frac{4\pi\Omega}{2} {\sum_{\mathbf{G}}}' \rho_T^*(\mathbf{G}) \frac{1}{\mathbf{G}^2} \rho_T(\mathbf{G}), \\
E_{sr} &= \frac{1}{2}\sum_{J\neq I}^{N} \frac{Z_v^2}{|\mathbf{R}_I - \mathbf{R}_J|} \operatorname{erf c}\left(\frac{|\mathbf{R}_I - \mathbf{R}_J|}{\sqrt{R_c^2 + R_c^2}}\right), \\
E_{self} &= \frac{1}{\sqrt{2\pi}} \frac{N Z_v^2}{R_c};
\end{aligned} \tag{3.3}$$

where N is the number of atoms, N_b the number of electronic states, ϵ_{xc} the exchange correlation energy density, $S(\mathbf{G}) = \sum_I e^{-i\mathbf{G}\cdot\mathbf{R}_I}$ the structure factor, $v_{loc}(|\mathbf{G}|)$ the Fourier components of the local part of the pseudopotential. Moreover,

$$\alpha_{l,m} = \left\langle \varphi_{l,m} \left| \delta v_{nl} \right| \varphi_{l,m} \right\rangle^{-1}$$

and

$$F^{l,m}_{I,i} = \sum c_h\left(\mathbf{G}\right) e^{i\mathbf{G}\cdot\mathbf{R}_I} \left\langle \delta v_{nl} \varphi_{l,m} Y_{l,m} | \mathbf{G} \right\rangle$$

are the contribution to the total energy of the non local part of the pseudo-potential δv_{nl} in the form of Kleinman and Bylander [24], where $Y_{l,m}$ is the spherical harmonic of angular momentum l, while $\left|\varphi_{l,m}\right\rangle$ is the atomic radial pseudo-function, for the same angular momentum. The last three equations in 3.3 are the electrostatic interaction energy. In order to efficiently treat the slowly decaying Coulomb forces the second, third and last term of Eq. 3.1 are rewritten by splitting out from the full ionic core charge a smeared Gaussian distribution of width R_c, centered at the ionic sites:

$$\rho_{ion} = -\sum \frac{Z_v}{\pi^{3/2} R_c^3} \exp\left[-\frac{|\mathbf{r}-\mathbf{R}_I|^2}{R_c^2}\right],$$

that added to the electronic charge density, lead to a total electrostatic pseudo-charge:

$$\rho_T = \rho_e + \rho_{ion}.$$

3.2 Parallelization strategy

The algorithm, that implements the above method is summarized in its essential parts in the flow chart 3.1. All contributions to the total energy, forces, and stress are calculated through the wave-functions coefficients ($c_h(\mathbf{G})$) in reciprocal space, and the charge densities in real ($\rho_T(\mathbf{r})$) and reciprocal space ($\rho_T(\mathbf{G})$), their expressions, as implemented in the code, are reported in appendix 6.3. As a consequence arrays storing wave-functions and charge density are the key quantities to work on for distributing the workload in a parallel implementation of the CP algorithm. Three main parallelization strategies driven by these data structures, as suggested also by other authors [25, 26, 27, 28], could be easily identified:

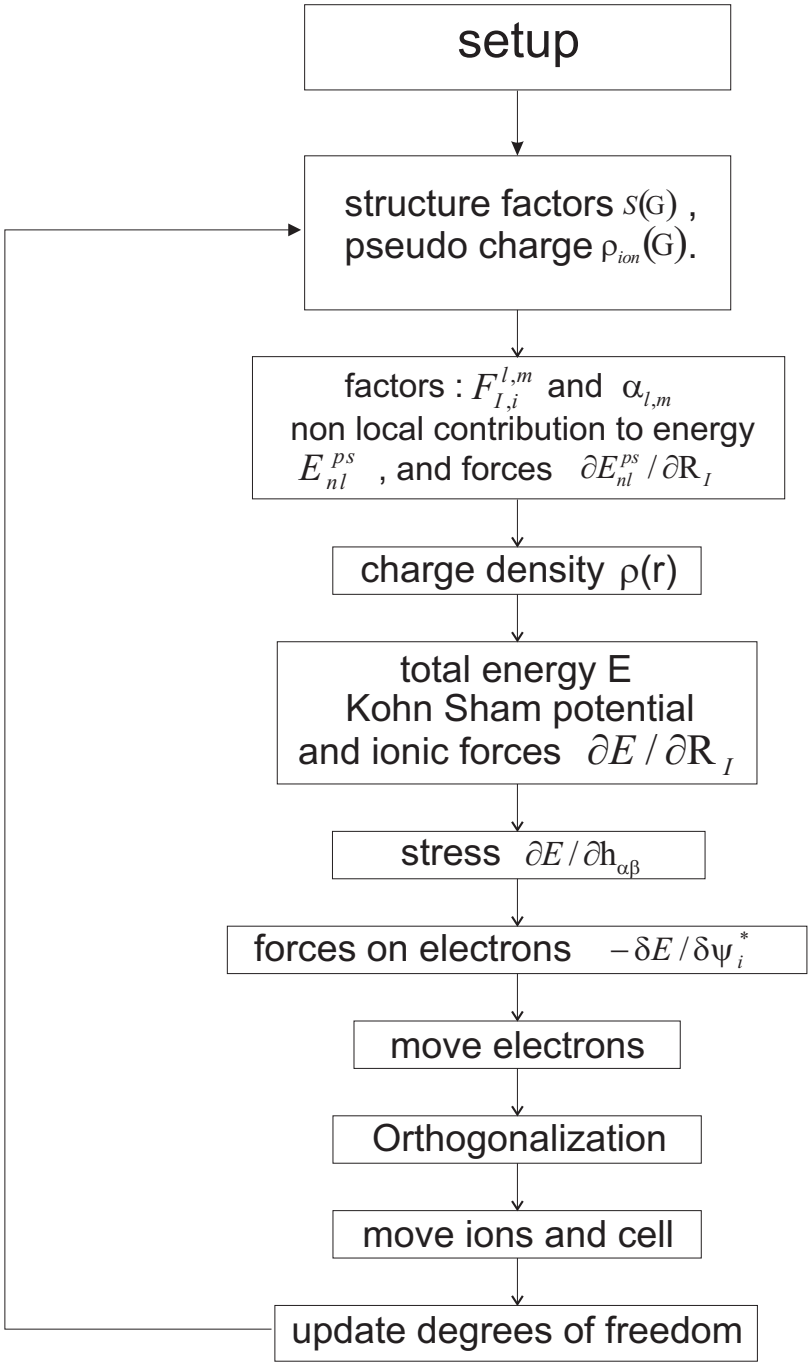

Figure 3.1: Schematic flow chart of our implementation of the CP algorithm.

a) *Distribute bands*. Wave-functions (ψ_i) with different band index (i) could be assigned to different processors. Since the number of bands grows linearly with the system size, this suggests the possibility of obtaining optimal performances keeping constant the number of bands per processor [25]. This strategy has however an intrinsic bottle neck in terms of redundancy and memory allocation, since a copy of the charge density must be present on each processor.

b) *Distribute real space and reciprocal vectors*. Computations involving $\mathbf{G}$ vectors in reciprocal space, and those involving values of the charge density on a grid in real space, are completely independent. It is thus possible to distribute both $\mathbf{G}$ vectors and elements of the charge density grid across processors [27]. This solution does not suffer for the bottle neck of case a) but necessitates of a parallel FFT algorithm, and more complex communications.

c) *Combinations of* a) *and* b). It is possible to subdivide processors in pools assigning different bands to each pool and spreading bands over processors within each pool, exploiting the benefits of the linearity of the size-bands relation, and avoiding the redundancy of the charge density allocation [26]. However the resulting algorithm and communications in this case are tightly linked to the underlying architecture, since in order to have a real improvement of the communication performance, the topology has to be taken into account while designing the code. In fact, processors inside a pool have to be physically close.

Note that in those cases where more than one k-point is used for the Brillouin-zone sampling, an additional way of distributing the workload is possible [27]. In fact, most of the operations (in particular the most time consuming ones, as FFT and orthogonalization of the wave-functions) are k-point independent, hence wave-functions with different k-points could be assigned to different processors to perform these operations concurrently. It is also possible to mix the

k-points distribution with one of the other distribution method, in particular codes combining b) and k-points distribution show good scaling performance and do not have memory redundancy problems [29]. However, for a large system the number of k-points needed is usually small (in our case we restrict to the Γ-point only), and does not allow an efficient implementation on a large number of processors.

We have chosen, for our parallel implementation, the distribution method b) because it is theoretically bottle-neck free, and thus well suited for all system sizes and processor numbers. Although method c) shares the same property, its communications have to be tuned on the underline hardware, which is against our purpose to have an architecture-free code with the best possible performances.

The code has been written in such a way to satisfy as much as possible the following guidelines: *portability*, *load balancing*, *minimization of communications*, *maximization of parallelism*.

Since different parallel machines are available on the market with different architectures, and since the underlying technologies are rapidly evolving without a leading standard, we believe that developing a portable code will be extremely useful and time saving.

To make the code as portable as possible we have designed it to have a layer structure (see Fig. 3.2). The topmost layer, containing all CP subroutines, is written in plain F77-F90 without any architecture-dependent specific calls or data structures; below this layer, there is a layer containing communications routines, architecture-dependent routines and blas lapack routines. In the code hierarchy, under the communication layer there is the communication library, that is completely isolated from the CP subroutines. In this way the communi-

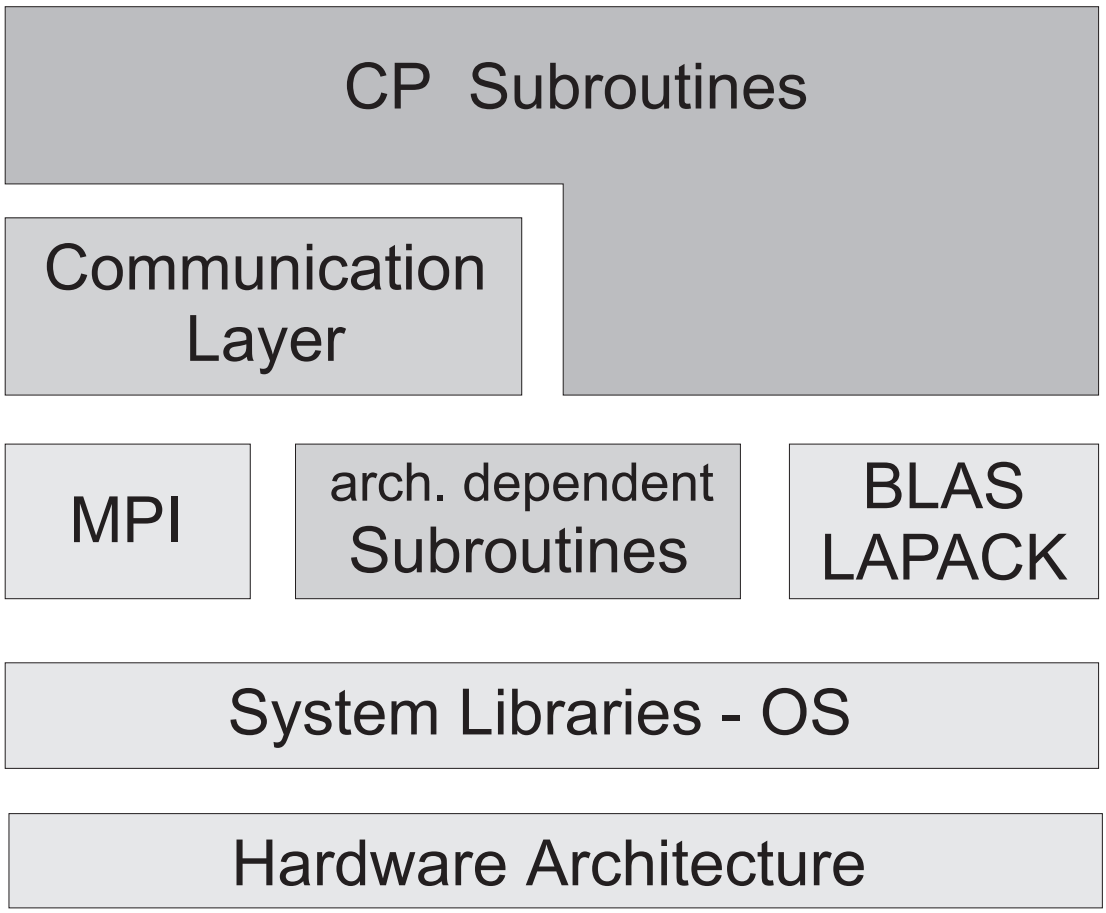

Figure 3.2: Structure of our code. The topmost layer, containing all CP subroutines, is written in plain F77-F90 without any architecture-dependent specific calls or data structures; below this layer, there is a layer containing communications routines, architecture-dependent routines and blas lapack routines. In the code hierarchy, under the communication layer there is the communication library, that is completely isolated from the CP subroutines.

cation library could be substituted (i.e. changing from PVM to MPI[1]), without modifying the CP subroutines, improving the portability of the code itself. The architecture-dependent subroutines are reduced to a minimal set, and only few hours of work are needed to rewrite them for a new architecture. However, for testing purposes, it is also possible to substitute the communication layer with a dummy layer, and to compile the code on a standard scalar workstation with only a very little overhead, due to calls to these dummy subroutines. It is important to note that in NUMA (Non Uniform Memory Access like SGI Origin2000) and UMA (Uniform Memory Access like SUN Ultra HPC 10000) machines, where a processor could address all the memory, explicit communication routines, contained in the communication layer, could be substituted by pointers exchanges. This is expected to give an improvement in the performance for a small number of CPUs, i.e. smaller than eight or sixteen.

In order to maximize parallelism we distribute, across the processors grid, all arrays storing quantities that are function of real and reciprocal space coordinates, $\mathbf{r}$ and $\mathbf{G}$. Only arrays storing positions and forces on ions are not distributed, and redundantly present on all processors. Their size is however always very small (few thousands of elements) for *ab initio* simulations, representing a very small fraction of the total allocated memory, that could easily reach several GigaByte. In particular we distribute wave-functions, charge density and all their related quantities; the resulting code shows good scaling properties (see Appendix 6.2).

The minimization of communications and the load balancing are often antagonist goals. Balancing the load in fact involves redistribution of data between processors (see for example the FFT section below). In designing the code we

[1]PVM (*Parallel Virtual Machine*) [30] and MPI (*Message Passing Interface*) [31] are two popular communication subsystem present on many parallel machines.

have assigned to the load balancing a higher priority with respect to the reduction of the total amount of data communications. As stated above, optimizing load balancing implies heavier communications, which in turn imply a larger number of synchronization points. Since in modern parallel computers the data transfer rate is usually very high, while synchronization could be time consuming, a large part of the work was dedicated to the reduction of the number of synchronization points (coarse-graining). In fact, while the mean performances of a single processor are obviously the same, locally (in time) the performances of more processors could be very different, especially when a large number of Processing Elements (PEs) is used, mainly due to different use of cache and memory accesses. Therefore, too many synchronization points could level off the performance of processors to that of the locally slowest one. This problem is dramatic when there are both many synchronization points and a non perfect load balancing.

3.3 Data distribution

As already stated, we need to represent physical quantities in both spaces because some of them are diagonal (local) in reciprocal space (as the kinetic energy), and others instead are diagonal in real space (as the exchange correlation potential). This determines the presence of two types of arrays in the code: 3D arrays to represent quantities in real space, and 1D arrays for quantities in reciprocal space, where $\mathbf{G}$ vectors are ordered according to their length. A fast Fourier algorithm (FFT) is used to transform quantities from one space to the other.

While in real space there is a unique 3D mesh for charge density and potentials, in reciprocal space there is a mesh for wave-functions ($\mathbf{G}$ vectors up to

$|\mathbf{G}|^2/2 = E_c$) and a larger one for potentials ($\mathbf{G}$ vectors up to $|\mathbf{G}|^2/2 = 4E_c$). Potentials span a larger space since they are function of the charge density which, in reciprocal space, is a convolution of wave-functions :

$$\rho_e(\mathbf{G}) = \frac{1}{\Omega} \sum_i^{N_b} f_i \sum_{\mathbf{G}'} c_i\left(\mathbf{G}'\right) c_i\left(\mathbf{G}-\mathbf{G}'\right) e^{i(\mathbf{G}-\mathbf{G}')\cdot\mathbf{r}}. \tag{3.4}$$

The presence of quantities spanning both reciprocal meshes, implies a careful data distribution to balance the workload. In Fig. 3.3 we show how reciprocal vectors are distributed in our code, for an example with four ($N_p = 4$) PEs; N_g and N_{gw} are the number of vectors whose kinetic energies are smaller than $4E_c$ and E_c respectively. Vectors up to E_c are divided among processor with a blocking factor of N_{gw}/N_p (the first N_{gw}/N_p $\mathbf{G}$ vectors to the first processor, the second N_{gw}/N_p $\mathbf{G}$ vectors to the second processor, and so on); the remaining ($N_g - N_{gw}$) vectors up to $4E_c$ are distributed with a blocking factor $(N_g - N_{gw})/N_p$. This distribution balances perfectly all loops within both meshes and eliminates any redundancy for quantities in reciprocal space.

Real space 3D arrays are subdivided by planes across processors (see Fig. 3.4), with the only limitation that optimal performance is achieved when at least one of the dimensions of the 3D array is a multiple of the number of processors. However, in most cases this is not a real limitation, because typical dimensions of the 3D real space mesh are three or four times the number of processors available (in a massively parallel computer).

With real and reciprocal meshes distributed in this way it is possible to confine communications and then synchronizations (see Fig. 3.5) only to FFT routines, orthogonalization and global reduction operations (such as those required to obtain global quantities as total energy or total forces).

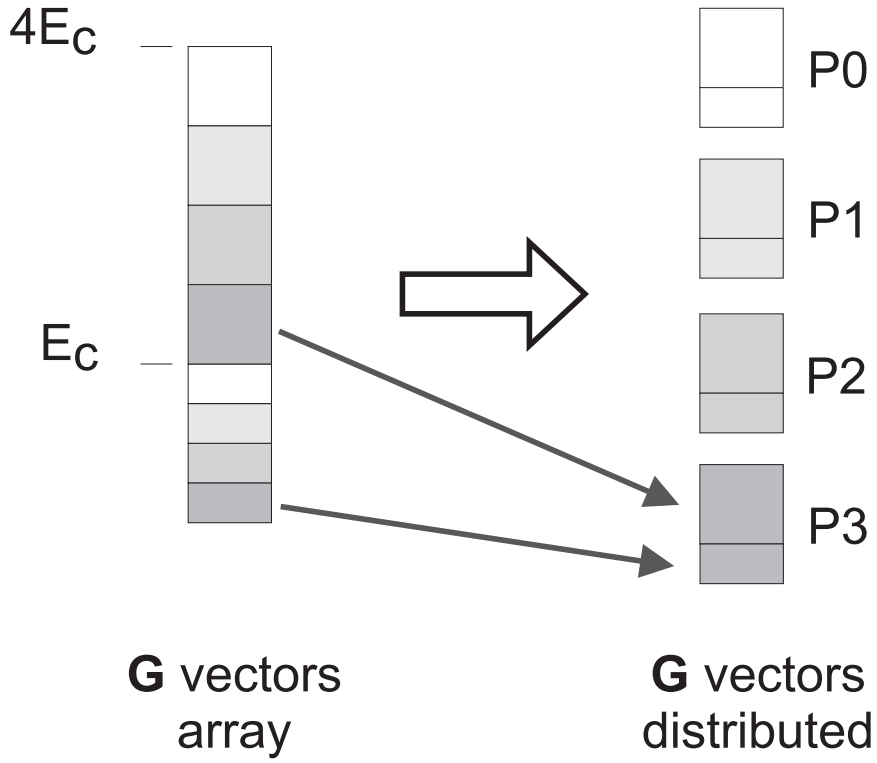

Figure 3.3: G vectors distribution. Left: G vectors stored in a one dimensional array ordered according to their modules. Right: G vectors distributed across four processors.

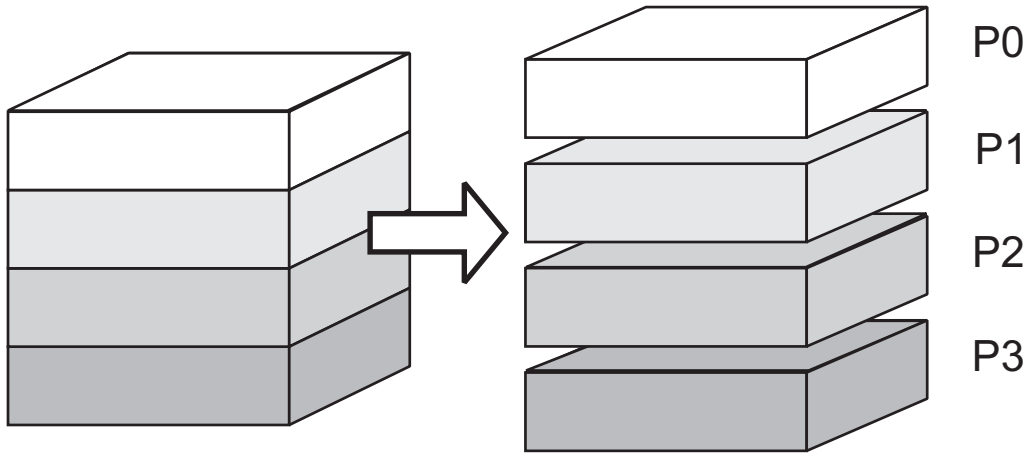

Figure 3.4: Real space 3D mesh data distribution. Left: 3D array storing the real space **r** vectors mesh. Right: The real mesh distributed by planes across four processors.

3.4 The FFT routine

The FFT routine, in the code, is called a number of times to transform wave-functions, charge density and potentials back and forward between reciprocal and real space (for many systems almost half of the time is spent performing this task). The size of the real space mesh is fixed by the charge density, and corresponds, in reciprocal space, to the mesh containing the sphere of G vectors smaller than $4E_c$. Wave-functions, whose elements are smaller than E_c, must be transformed on the same real mesh as the charge density. Since standard FFT algorithms operate between meshes of the same size, in our case the wave-functions should be copied into a bigger mesh, and then transformed. It is clear that in this way, a lot of time is wasted in transforming elements whose value is zero. To optimize this operation, we adopt an *ad hoc* FFT algorithm for wave-functions.

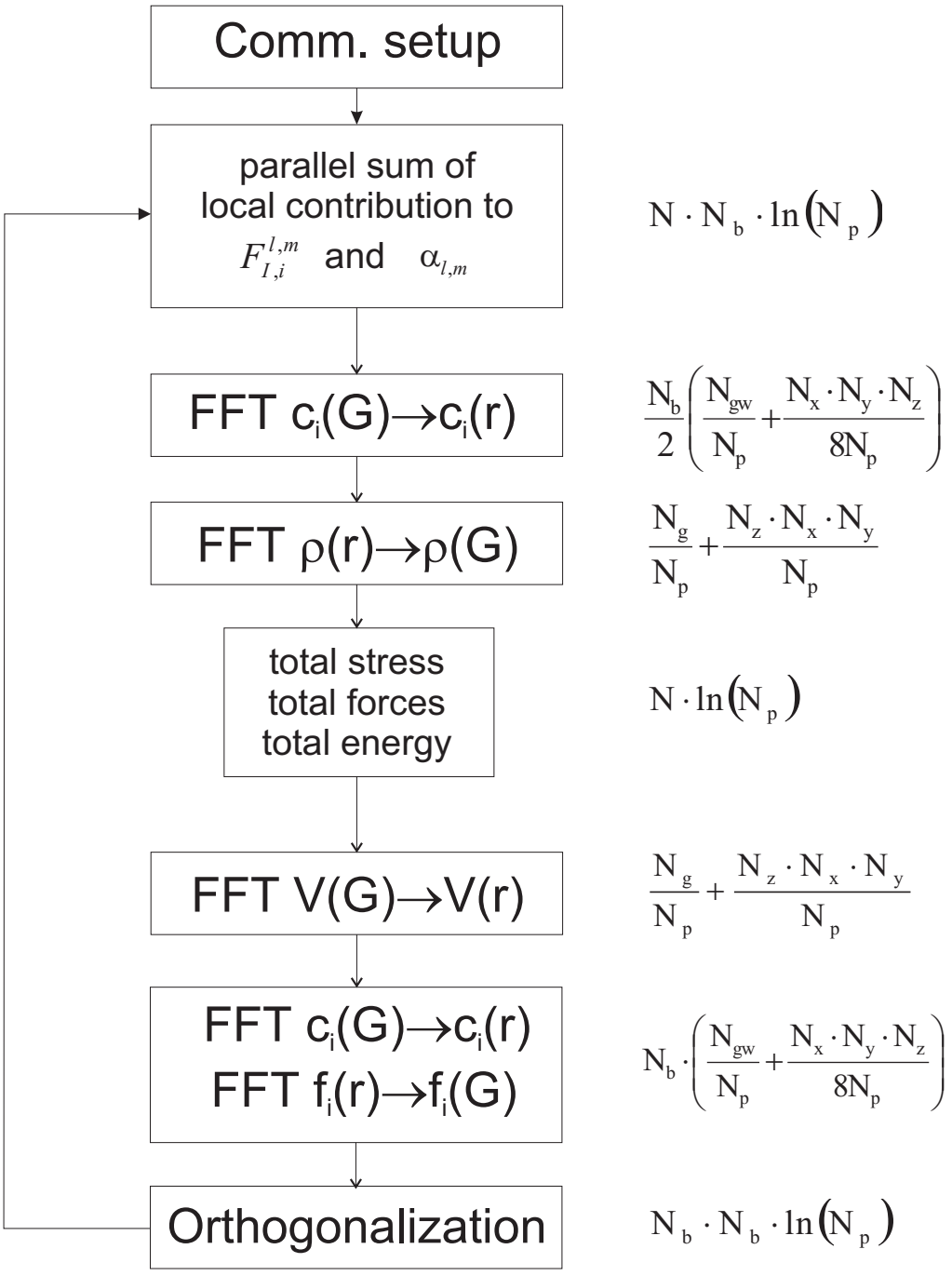

Figure 3.5: Communications Flow chart. Left: Computations involving communications and synchronization. Right: complexity of the communications (per processor). Here N, N_b, N_p are the number of atoms, electronic states and processors respectively; N_g and N_{gw} are the number of G vectors up to $4E_c$ and E_c. N_x, N_y, N_z are the sizes of the FFT mesh.

The algorithm we have implemented is sketched in Fig. 3.6, for the case of four PEs ($N_p = 4$) and transformation form reciprocal to real space. It takes advantage of the fact that a 3D FFT is a linear superposition of three subsequent series of 1D FFTs, along the Cartesian coordinates. For each series, only those 1D FFTs containing non zero elements are evaluated. In the upper panel of Fig. 3.6 a top view of the FFT grid (N_x, N_y, N_z) together with the cut-off radius are shown. In this example we consider the case in which we start transforming from the 1D FFTs along the z direction. Columns (xy small squares) are allocated by the processors only if they contain at least one G vector of the inner sphere. Allocated columns are assigned to the processors (see colors code) in such a way that the number of FFTs per processors differs at maximum by one (in the case that the number of columns is not a multiple of the number of processor). Since G vectors are distributed as shown in Fig. 3.3, the columns for a given processor could result incomplete, and exchange of data is needed before starting the FFT. The total number of 1D FFTs calculated in this step is approximately $1/8$ ($N_x N_y/8$) the number of a standard 3D FFT algorithm ($N_x N_y$). The transformed columns are then transposed to distribute the z direction across processors by planes, giving rise to the correct data distribution as for the real 3D arrays. After that, only those xz columns that contain at least one element different from zero are transformed along the y direction (Fig. 3.6 middle panel). Here the number of 1D FFTs is reduced by $1/2$ ($N_x N_z/2$) with respect to standard routines. Finally all yz columns are transformed along x direction. The complexity (order of the number of operations) of the above algorithm is :

$$N_y N_z N_x \left\{ \frac{\ln(N_z)}{8} + \frac{\ln(N_y)}{2} + \ln(N_x) \right\},$$

It is then convenient to choose N_z as the largest dimension and N_x as the smallest

one. This algorithm is obviously used also in the backward direction from the real to the reciprocal space.

FFTs on the bigger mesh used to construct the potential from the charge density, are instead performed using a standard 3D parallel FFT algorhitm. In this case, in fact, the number of zero elements is low and the gain obtained with the previous algorithm usually is less than the gain obtained using optimized FFT subroutines available from machine libraries.

Communications within the FFT are quite complex and for this reason a communication setup has been introduced in the initialization part of the code. Through an index array, each G vector is associated to the ID (identification number) of its source and destination PEs. In this way, during the communication event, vectors could be packed and exchanged without computations. The use of buffers and global gather scatter communication operations allowed us, in our *ad hoc* FFT, to introduce only two synchronization-communications points, at the beginning and between the first and second series of 1D FFT.

3.5 Orthogonalization

The orthogonality constraints for the wave-functions ψ_i at time $t + \Delta t$, are satisfied by solving a matrix equation of size N_b^2 (see Appendix 6.1), where N_b is the number of electronic states. Terms entering this equation are calculated through scalar products between wave-functions, so that the computational complexity of these operations is $N_{gw}N_b^2$. The solution of the matrix equation has instead a complexity N_b^3 and involves both matrix multiplications and a matrix diagonalization.

The procedure has been fully parallelized writing parallel versions of the

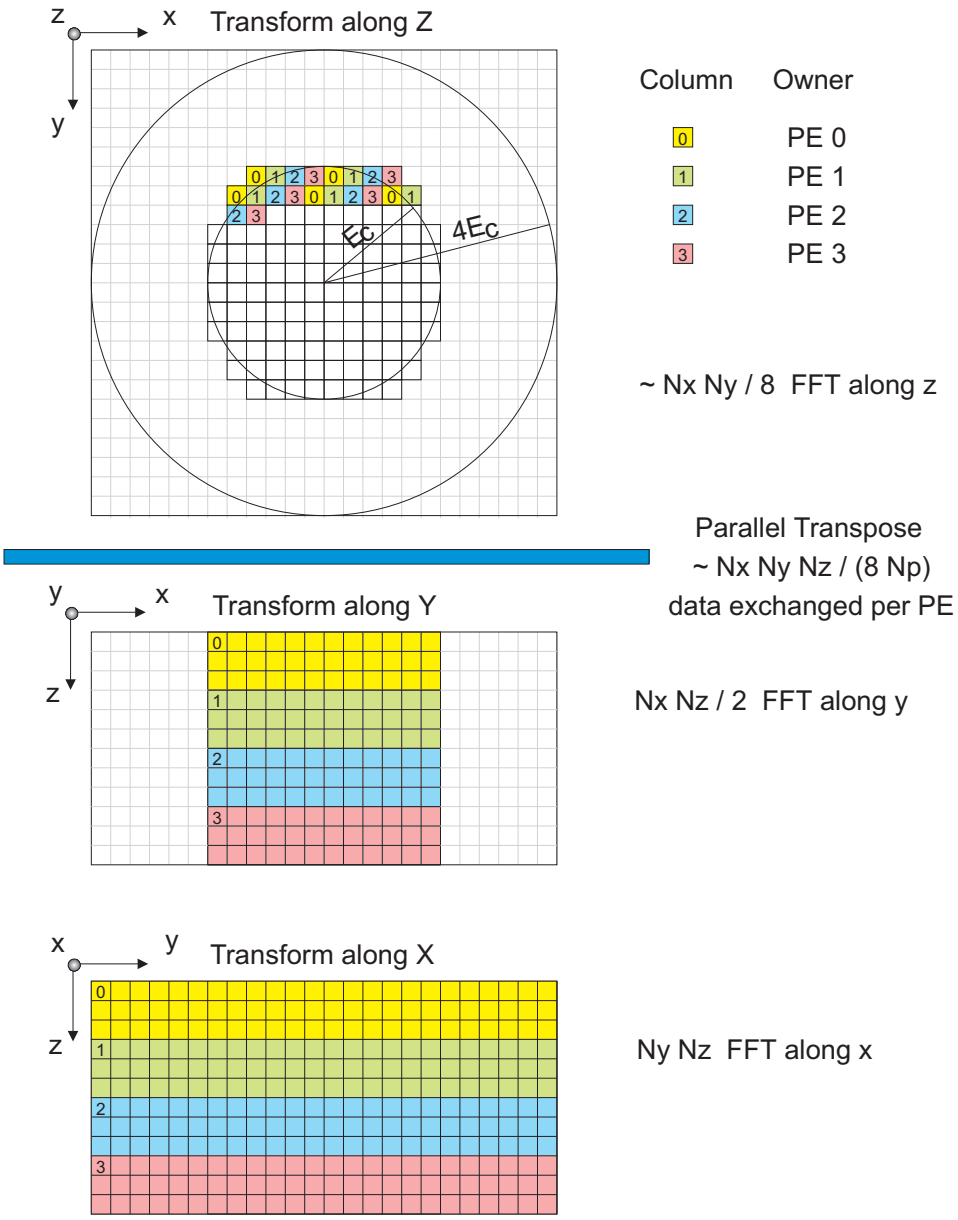

Figure 3.6: Scheme of our *ad hoc* FFT routine. Upper grid: top view of the FFT reciprocal space mesh, the xy columns are distributed across four processors according to the color code scheme. Each processor performs its 1D FFTs in the z direction. Middle grid: lateral view of the FFT grid, the xy columns are transposed in order to distribute the FFT grid by plane across processors. Each processor performs its 1D FFTs in the y direction. Lower grid: lateral view of the FFT grid, no communication is needed, each processor performs its 1D FFTs in the x direction.

above matrix operations. The computational complexity per processor is

$$\frac{N_b^2 \left(N_b + N_{gw}\right)}{N_p},$$

while the communication complexity per processor is

$$\frac{N_b^2 \log N_b}{N_p}.$$

It is remarkable to observe that, in the limit of large size problems the communications become negligible with respect to the computations.

Chapter 4

Water and Ammonia

In this chapter we present the results of *ab initio* simulations done on water and ammonia in the pressures and temperatures range 30–300 GPa and 300–7000 K. The simulations were aimed to study the behavior of the high-pressure high-temperature phases of these simple molecules, with particular attention to the properties of interest in high-pressure and planetary physics.

In the last years, in fact, a large number of shock-wave and diamond anvil cell experiments have been carried out in these range of pressures and temperatures on hydrogen-bounded systems, raising a number of new and interesting questions.

The high-pressure phase diagram of water at room temperature is quite well understood. At 2 GPa the water crystalline structure is the so called ice VII [32]. Recent studies have shown that ice VII transforms at about 70 GPa, into sym-

metric ice X, where hydrogen and covalent bond distances between H and O become identical, so that the molecular character is lost [33]. This phase is stable up to 300–400 GPa where a transition to a new phase has been predicted [34].

The room temperature phase diagram of ammonia has also been investigated up to 80 GPa [35, 36, 37]. Above 3 GPa the crystalline structure of ammonia is the orientationally ordered orthorhombic pseudo-hcp (Ammonia IV, see Fig. 4.2). This phase has been found to be stable in the range 3–15 GPa [38]. Above 15 GPa the crystalline structure is still unknown, and different structures have been proposed [35, 36]. Claims of hydrogen bond symmetrization at 60 GPa, have been made [35], but they have not been confirmed by subsequent studies [38, 36].

At higher temperature, a recent study has shown a high proton conductivity in water at 2000 K and 300 GPa [34]. However, no detailed study has been made on the behavior of the hydrogen bond in water and ammonia in the range of pressure and temperature of interest in planetary physics. Moreover, the melting line and the properties of both molecules in the fluid phase at these pressures are not known.

Many open questions in planetary physics related to the properties of water and ammonia at these extreme conditions exist. In particular, Uranus and Neptune density profiles suggest that, buried between a rocky core and a gaseous atmosphere, their interiors are mostly composed of a thick intermediate layer of "hot ices", predominantly water, hydrocarbons and ammonia (Fig. 4.1) in solar proportions (molar fractions: 56 % H_2O, 36 % CH_4 and 8 % NH_3) [40]. Pressure and temperature conditions within the ice layer range from 20 GPa – 2000 K, to 600 GPa – 7000 K [39], along the planetary isentrope[1]. Many observable

[1]The ice layer is supposed to be almost adiabatic (provided it is uniformly mixed and convective),

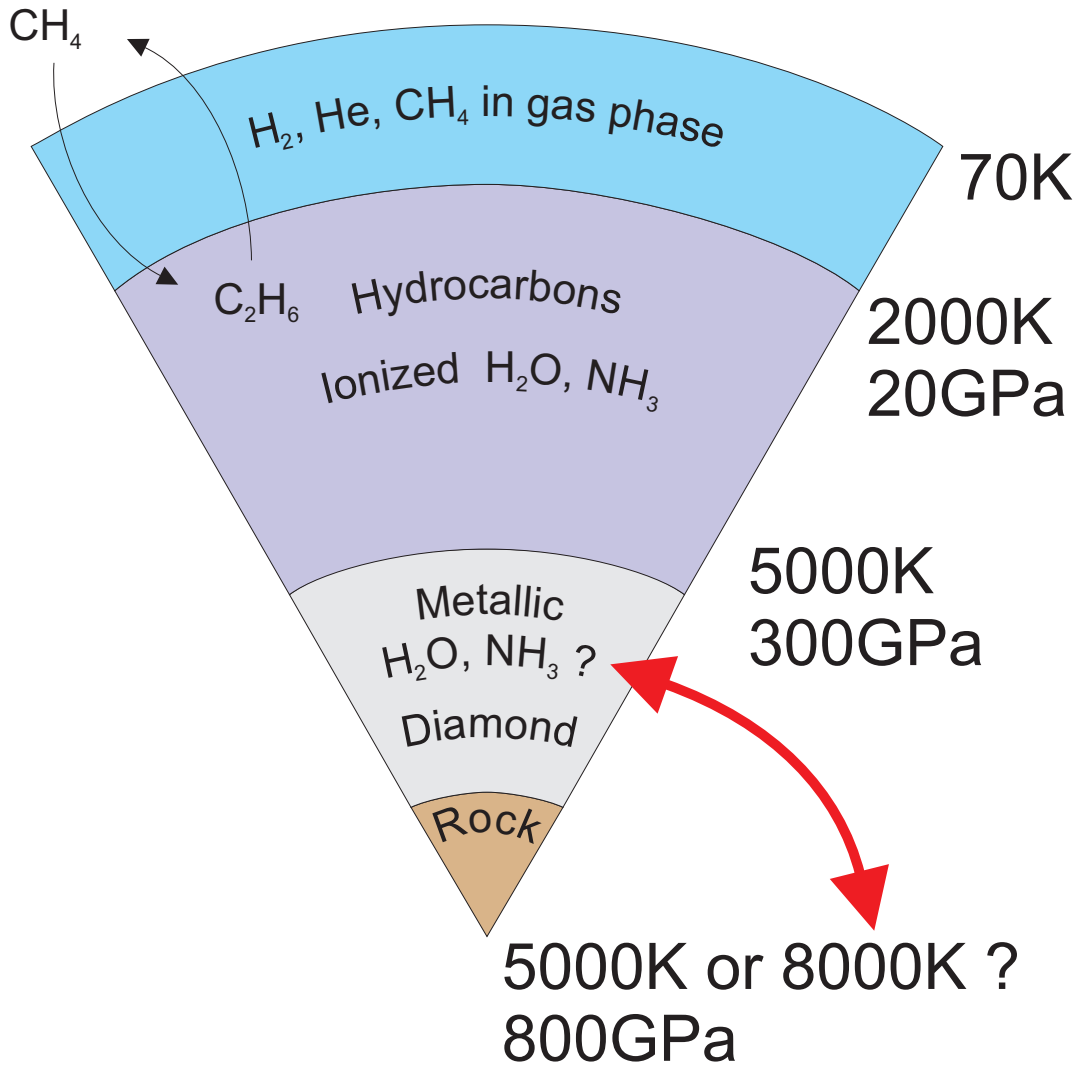

Figure 4.1: Sketch of the internal structure of Neptune and Uranus. Three layers model [39]: external gaseous layer, middle ice layer and rocky core. Using constant pressure *ab initio* molecular dynamics, Ancilotto *et al.* [1] have shown that, in the ice layer, methane dissociates into hydrocarbons of higher molecular weight, suggesting that this could be the source of the anomalous atmospheric abundance of ethane observed by the Voyager II spacecraft. In this thesis, using the same tool, we predict the ionization of water and ammonia in the ice layer and, if temperature are sufficiently high ($\sim$7000 K), near to the ice-core boundary we predict water and ammonia to be metallic.

properties of these planets, such as gravitational moments, and partially also their atmospheric composition, are thought to be determined by the physical and chemical properties of matter within this layer. In particular the ice layer is considered to be the source of the strong magnetic field measured by the Voyager II spacecraft on Uranus and Neptune [41]. Electrical conductivities in the ice layer of the order of 10 $(\Omega\, cm)^{-1}$ are necessary to sustain the planetary dynamo mechanism for the generation of such a magnetic field [42]. Since water is by far the most abundant component of the mixture, it has been suggested [42, 43] that the large conductivity may arise from nearly complete ionization of H_2O. However, water metalization can not be ruled out at the extreme conditions of the deeper regions of the ice layer. If this is the case, electronic conduction may also contribute [44].

The only non-astronomical data available on the behavior of ices at these extreme conditions come from shock-wave experiments. The equation of state of both water and ammonia and of a mixture of water, ammonia and isopropanol dubbed "synthetic Uranus" have been measured in shock-wave conditions up to 200 GPa [43, 45]. The shock-wave measurements provide constraints on the density profiles of Uranus and Neptune [46] and show that the electrical conductivity in water and ammonia increases exponentially along the shock Hugoniot [2] up to $\sim$ 20 GPa and then levels off [43, 45]. These data are consistent with activated molecular dissociation at low pressure, whereas the high-pressure plateau suggests a nearly constant concentration of dissociated species. The measured value of the conductivity of water above 20 GPa (10 $(\Omega\, cm)^{-1}$) was also shown to support planetary dynamo models [43]. However, the absence of conductiv-

the values of pressure and temperature, as functions of the distance from the center of the planet, lay on a curve of constant entropy.

[2] In a shock-wave experiment the thermodynamic variables are related to the kinematic parameters of the shock-wave itself through the Rankine-Hugoniot relations [47].

ity data above 77 GPa (i.e. below 0.7 planetary radii) and the uncertainty on the conduction mechanisms largely prejudice the construction of reliable models for the origin of the planetary magnetic field. Moreover, shock-wave experiments provide information on the equation of state only along the shock Hugoniot which of course does not uncover the full phase diagram.

Looking at the high-pressure experimental data on ammonia and water it emerges that between the room temperature diamond anvil cell data and the thousands Kelvin shock-wave data, there is a vast region of the PT phase diagram yet unexplored.

Computer simulations can be extremely effective to explore regions of the phase diagram not directly accessible by experiment, providing a detailed picture of the behavior of matter under extreme conditions. Use of *ab initio* is essential to describe hydrogen bonding and molecular dissociation in water and ammonia [48]. *Ab initio* simulations have already been used to clarify the high-pressure, high-temperature behavior of methane [1] (that together with water and ammonia is supposed to form the planetary ice layers), and to study the structural phase transitions of ices at high pressure [34].

Several *ab initio* molecular dynamics simulations have been performed to gauge the phase diagrams of ammonia and water at planetary conditions of temperature and pressure. Water has been simulated at 60, 150 and 300 GPa, with a super-cell of 32 molecules, while for ammonia simulations have been performed at 5, 30, 60, 150, 300 GPa with a super-cell of 64 molecules. A larger super-cell for ammonia is needed to obtain a satisfactory convergence of the calculated quantities with size. Temperature in all simulations was varied between 300 and 7000 K. In all simulations we have used Martins Troullier norm-conserving pseudopotentials [49], and gradient corrections to the local-density

approximation in the form proposed by Becke [50] for the exchange energy and by Lee-Yang-Parr [51] for the correlation energy which describe well the hydrogen bonding [48, 52]. Electronic wave-functions were expanded in plane wave up to a kinetic energy cutoff of 80-100 Ry, while the Brillouin zone sampling was restricted to the Γ point. The time step for the integration of the equation of motion was in the range 1-6 atomic units depending on the temperature of the simulated system.

In the following part of this chapter we analyze the results for ammonia (section 4.1), for water (section 4.2), and their implications for planetary physics (section 4.3).

4.1 Ammonia

Ammonia (NH_3) like water, is a polar hydrogenous molecule. With respect to water, however, ammonia has a weaker hydrogen bond, that in the solid phases becomes shared, with three hydrogen atoms bonding to a single lone pair (see Fig. 4.2). The crystal structure of the solid phases, and the molecular interactions in the fluid phases of these two simple molecules are determined by the properties of their hydrogen bond. Of fundamental interest, therefore, is to understand its behavior under different conditions of pressure and temperature and how this bond determines the physical properties of the systems.

The low-pressure low-temperature phase diagram of ammonia is shown in Fig. 4.3 and the corresponding crystal structures are listed in Tab. 4.1. The high-pressure side of the phase diagram has been fully characterized up to ammonia IV, which has an orthorhombic pseudo-hcp crystal structure with four molecules per unit cell and $P2_12_12_1$ space group (see Fig. 4.2), and it is stable in the range of pressure 3–15 GPa. Two further phases have been proposed for ammonia

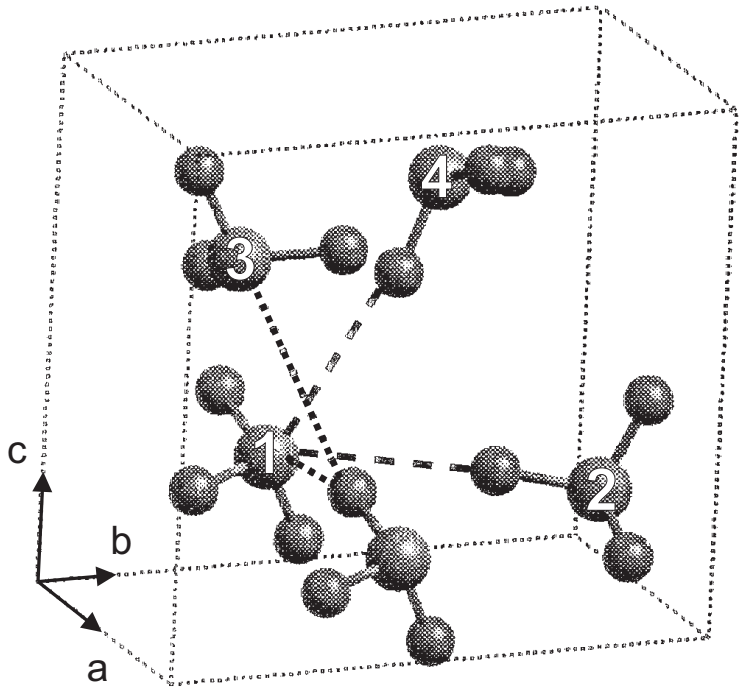

Figure 4.2: Ammonia IV orthorhombic unitary cell, small and big balls represent hydrogen and nitrogen atoms respectively. Molecules labeled 1-4 are within the cell. Sheared H-bond geometry : each hydrogen is H-bonded to two nitrogens (dotted lines), while each nitrogen is H-bonded to three hydrogen (dashed and dotted lines starting from nitrogen labeled 1).

Phase	Structure	Symmetry
I	Cubic (pseudo fcc)	$P2_13$ Ordered
II	HCP	$P6_3/mmc$ Disordered
III	FCC	Fm3m Disordered
IV	Orthorhombic (pseudo hcp)	$P2_12_12_1$ Ordered
V	Cubic (?)	I43m Ordered
VI	Cubic (?)	Pn3m or Pm3m Ordered

Table 4.1: Structure and space group of ammonia known phases.

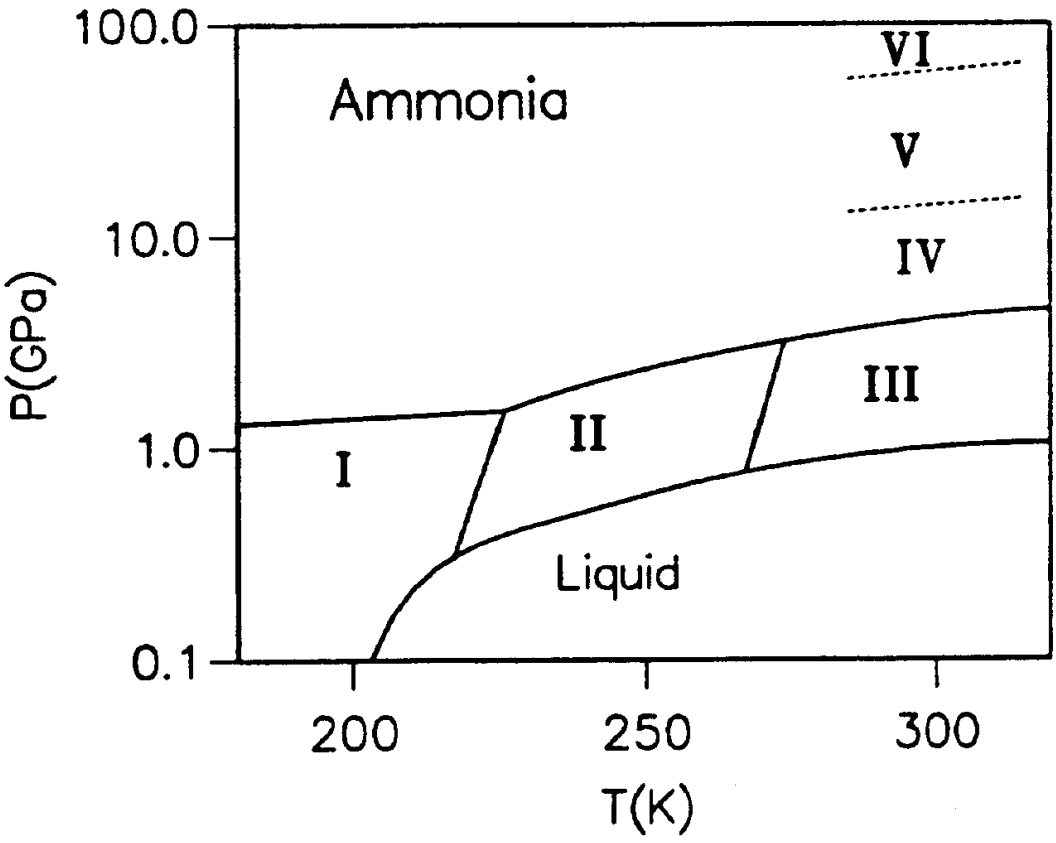

Figure 4.3: Experimental P-T Phase Diagram of Ammonia (from Loveday *et al.* [38]). The structure of the phases is reported in Tab. 4.1

Lattice parameters	Theory	Experiment
a	6.16	6.142
b	10.65	10.693
c	10.20	10.122

Table 4.2: Theoretical and experimental [38] lattice parameters of ammonia IV at 5 GPa.

on the basis of Raman scattering [35]: one with cubic structure and symmetry $I\bar{4}3m$ above 15 GPa, and the other with cubic structure and symmetry Pn3m or Pm3m above 60 GPa. In this last phase hydrogen bonds were suggested to be symmetrical [35] with bond angles H-N-H of 90 degrees. A subsequent X-ray diffraction study by Otto *et al.* found, in contrast, that ammonia IV is stable up to 60 GPa [36].

Before starting simulations at higher pressures, we tested our "machinery" on ammonia IV at 5 GPa and room temperature, where data on the values of the lattice parameters and atomic positions are well established. A satisfactory agreement with experimental data has been obtained with a super-cell of 64 atoms and an energy cut-off of 100 Ry. Values of lattice parameters are reported in Tab. 4.2 while in Fig. 4.4 the experimental (upper panel) and the theoretical (lower panel) structure factors are compared.

It is well known that at low pressure van der Waals interactions are important in determining the structure of molecular crystal [53, 54]. However in this calculation we do not include any van der Waals corrections to the molecular interactions. The good agreement with experimental results might mean that in this pressure regime van der Waals interactions are already negligible. Neglecting van der Waals interactions is even more justified at higher pressure where electronic wave-functions overlap increases and covalent and ionic interactions

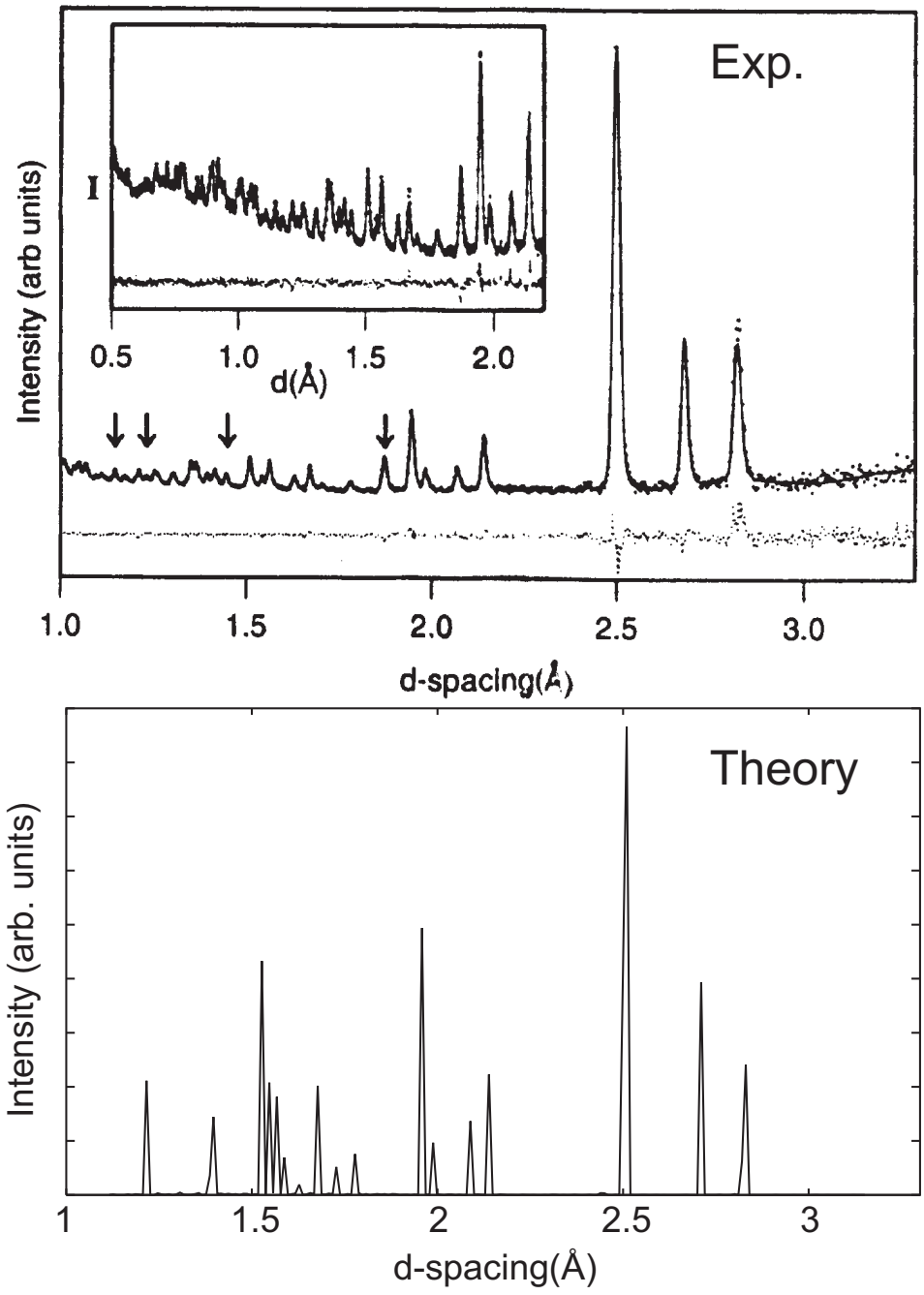

Figure 4.4: Comparison of the experimental [38] (upper panel) and calculated (lower panel) structure factors of Ammonia IV at 5 GPa. The arrows mark the reflections from the tungsten carbide anvils.

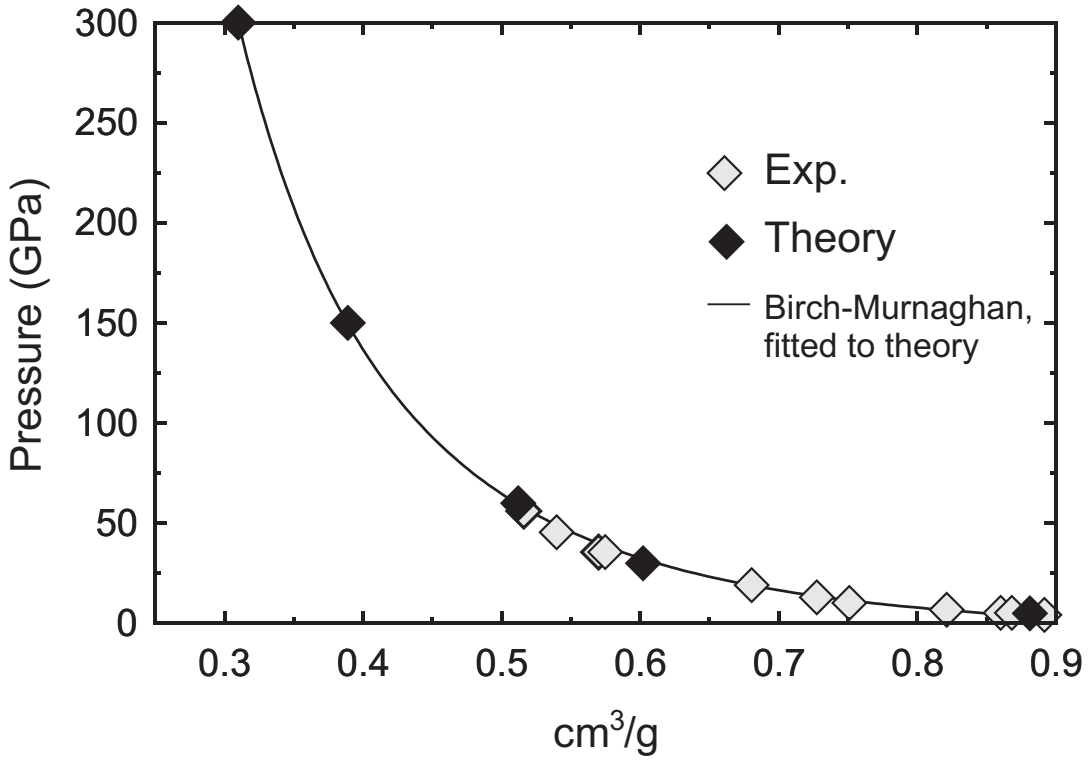

Figure 4.5: Pressure vs. Volume Equation of State of ammonia IV at 300 K. Calculated values of the volume (black diamonds), Birch-Murnaghan curve fitted to the calculated values (continuous line), experimental [36] X-ray values (gray diamonds).

become stronger.

Other runs at 30, 60, 150, 300 GPa and room temperature have been made to calculate the low temperature equation of state (Fig. 4.5) and to look for an hypothetical hydrogen-bond symmetric phase, that, as already mentioned, has been claimed to occur around 60 GPa. Upon compression, distortions of ammonia IV from the ideal hcp structure was found to decrease. For example, at 300 GPa we find c/a=1.634 and b/a=1.726, to be compared with those at 5 GPa: c/a=1.648 and b/a=1.741, and with those of an ideal hcp lattice: c/a=1.633 and b/a=1.732. No sign of hydrogen bond symmetrization has been observed. Even

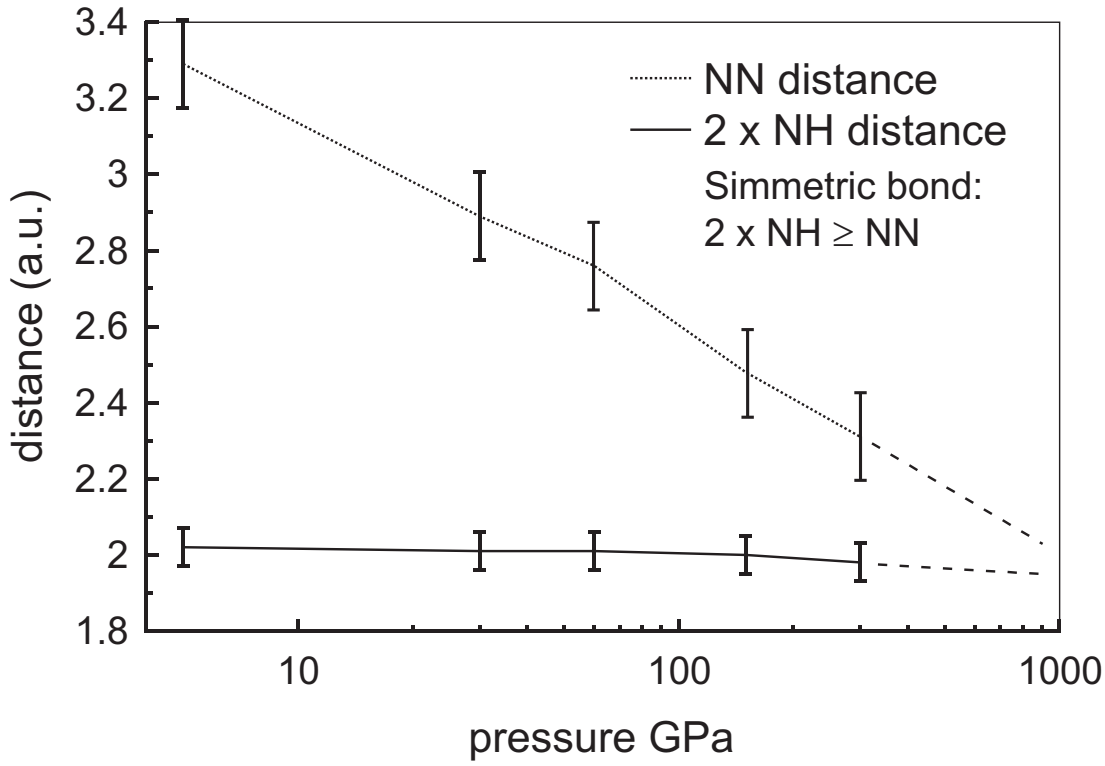

Figure 4.6: Pressure dependence of the nitrogen-nitrogen nearest neighbor distance (dotted line), and two times the nitrogen-hydrogen molecular bond distance (continuous line). In a symmetric arrangement the relation 2xNH$\geq$NN must be satisfied, the inequality ($>$) referring to the case in which the two N-H bonds are not collinear.

at 300 GPa molecules are quite distinct objects, with hydrogens far from any bond center position. If we consider the distance between nearest neighbor nitrogens d(N-N) and the distance between nitrogen and its neighbor hydrogens d(N-H), in a symmetric arrangement the relation 2d(N-H)$\geq$d(N-N) must be satisfied, the inequality ($>$) referring to the case in which the two N-H bonds are not collinear. In Fig. 4.6 we plot the d(N-N) and 2d(N-H) vs. pressure for Ammonia IV. As can be seen, in this structure, symmetrization becomes geometrically possible only at pressures of the order of 10 Mbar. This is of course an upper limit and does not role out symmetrization at lower pressure, in a phase different from ammonia IV. However if the symmetrization process is similar to that of water, the actual transition could be expected to be not too far from this limit [33, 55]. In order to answer to the question about the possibility of other structures for ammonia with symmetric bond, we tried to optimize the simple cubic structure proposed by Gautier *et al.* [35] at 300 GPa. The cubic structure resulted energetically disfavored with respect to pseudo-hcp (by about 4 eV / molecule) and the bond-center positions for H atoms are not in stable equilibrium. In fact, relaxing the structure, H atoms go off center and, in a constant pressure simulation, the system transforms into an fcc structure, with a sliding of the (100) planes along the [110] direction and a large volume reduction ($\sim$3 a.u. / molecule). The energy of this new fcc phase at 300 K is comparable, within our accuracy, to that of the pseudo-hcp structure. We have also tried the fcc symmetric structure proposed by Gautier *et al.* at 300 GPa, but relaxing the structure we again find that the hydrogens leave the bond center positions and form ammonia molecules. However, in a constant pressure simulation the structure remains fcc. The energy of this structure is again comparable with that of the pseudo-hcp structure. These two results make the fcc an alternative

candidate structure for ammonia at 300 GPa. This is not a surprise because hcp and fcc structures differ only starting from the third nearest neighbor, and both structures are present in the phase diagram of ammonia. We conclude stating that our short simulation times and small cell sizes are not sufficient, in this case, to discriminate between fcc and hcp, but do safely rule out the occurrence of hydrogen bond symmetrization.

The first simulation exploring the high-pressure high-temperature phase diagram of ammonia has been performed at 60 GPa. The super-cell of 64 molecules with the structure of ammonia IV has been first equilibrated at 300 K. We found that both the geometry of the cell and the relative orientation of the molecules did not change significantly with respect to that at 5 GPa. In particular, the relative position of the peaks in the structure factor did not change. As the temperature was increased, the system transforms, between 500 and 1000 K into an hcp plastic phase with free rotating molecules. This is not a surprise, as also the low pressure hcp solid phase, at room temperature (see Tab. 4.1) is orientationally disordered. This implies that in a close packed configuration forces on the molecules have a low degree of directionality even at high pressure. Between 1000 K and 1200 K the system becomes superionic. Hydrogen atoms break their covalent bonds and start diffusing through the lattice while nitrogen atoms are still vibrating around their hcp equilibrium positions. We have located the phase transition looking at the mean square displacement (m.s.d.) of N and H independently. In Fig. 4.7 (upper panel) we report the m.s.d. during a simulation at 60 GPa; diffusion clearly starts slightly above 1000 K. A subsequent visual inspection of the atomic positions for the same run validates the high mobility of diffusing hydrogens. In Fig. 4.7 (lower panel) the trajectory of an H through the N crystal lattice during the same simulation of the upper panel is reported.

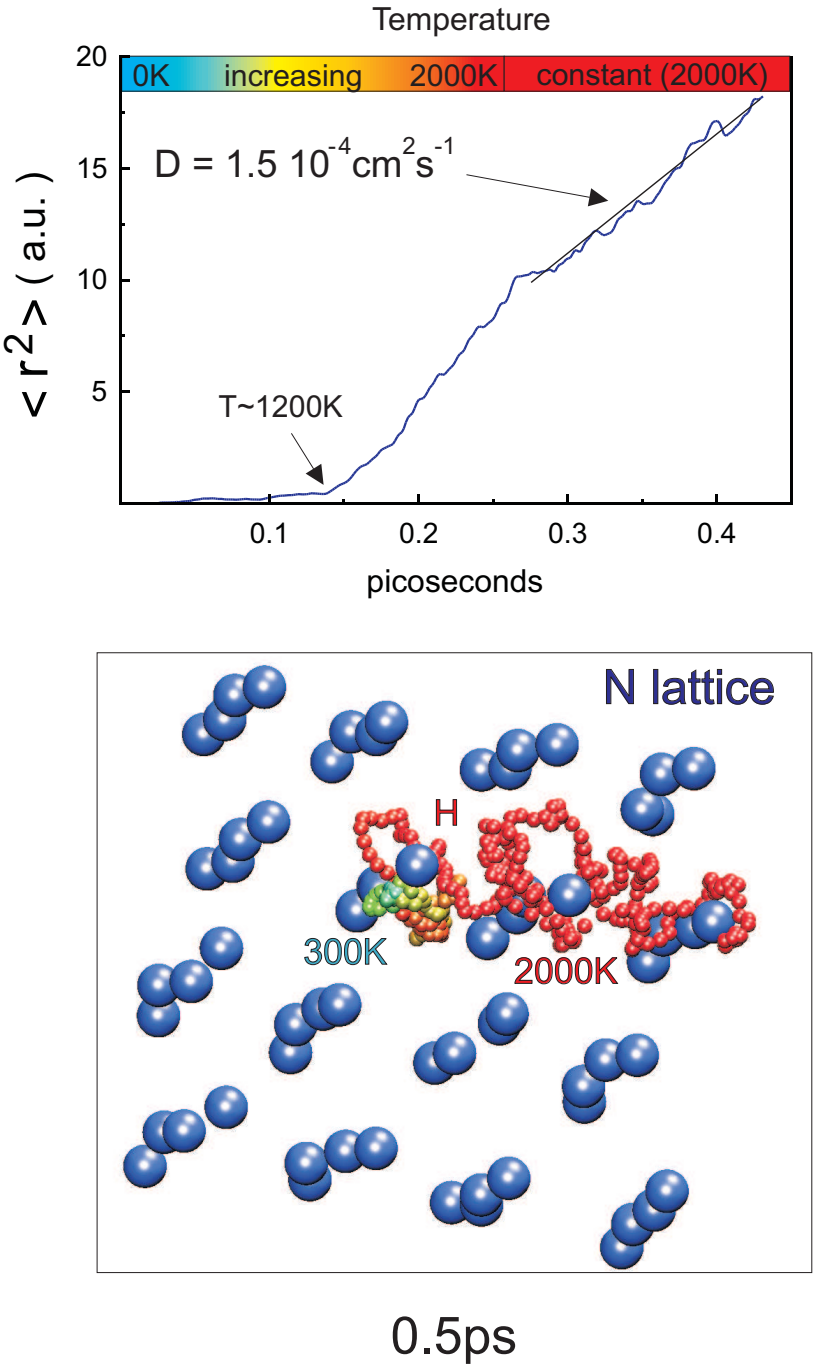

Figure 4.7: Upper Panel: Mean Square Displacement of hydrogen atoms in a simulation run at 60 GPa where temperature has been increased up to 2000 K. Lower Panel: typical trajectory of a diffusing hydrogen atom through the nitrogen sublattice, recorded during the same simulation of the upper panel. The color of the hydrogen match the temperature color code of the upper panel.

Work is still in progress with the aim of clarifying the statistics of the diffusion process in the superionic phase. Visual inspection of the trajectories reveals that the motion of the hydrogens is quite correlated; in fact, in spite of the large diffusivity of hydrogens, nitrogen atoms are on average coordinated with three hydrogens. The lattice parameters of the superionic phase are those of an ideal hcp (c/a=1.63 and b/a=1.73), possibly a consequence of the quasi-spherical distribution of the hydrogens around each nitrogen.

Around 2000 K also the N sublattice melts and the system transforms into a superprotonic fluid, the diffusion constant of nitrogen and hydrogen being at 3000 K $1 \pm 0.3 \cdot 10^{-4} cm^2 s^{-1}$ and $6.5 \pm 0.5 \cdot 10^{-4} cm^2 s^{-1}$ respectively. In the superprotonic fluid phase the observed correlations between hydrogen jumps are lost. This phase is electronically an insulator with a gap between valence and conduction band of 3–4 eV, but its electrical conductivity is expected to be high due to the high mobility of protons.

We calculate the conductivity $\boldsymbol{\sigma}_{\nu\mu}$, in the linear response approximation, where conductivity is related to the fluctuations of the polarizability via the Green–Kubo formula [56]:

$$\boldsymbol{\sigma}_{\nu\mu} = \frac{1}{k_b T V} \int_0^\infty \left\langle \dot{P}_\nu (t)\, \dot{P}_\mu (0) \right\rangle dt, \tag{4.1}$$

where T is the temperature and P_ν the polarizability vector in Cartesian components. Since ammonia in this phase is electronically insulating, we can calculate the polarizability through the method proposed by King-Smith and Vanderbilt through the Berry–phase formalism [57, 58, 59]:

$$P_\nu = \frac{2\,|e|}{|\mathbf{G}_\nu|\, V} \operatorname{Im} \ln \det \langle c_i | \exp\left(-\mathrm{i}\mathbf{G}_\mu \mathbf{r}\right) | c_j \rangle\,, \tag{4.2}$$

where $\mathbf{G}_\nu$ are the reciprocal lattice basis vectors and c_i are the Γ-point electronic wave-functions. Expression 4.1 can be simply rewritten, in the limit $t \to \infty$, as

the Einstein relation:

$$\boldsymbol{\sigma}_{\nu\mu} = \lim_{t\to\infty} \frac{1}{2tk_bT} \left\langle \left[P_\nu\left(t\right) - P_\mu\left(0\right)\right]^2 \right\rangle, \tag{4.3}$$

where only the polarization itself (and not its derivative) is present. Unfortunately, the values of P_ν calculated *ab initio* through Eq. 4.2 are subject to large fluctuations related to the fact that, within the CP scheme, wave-functions oscillate around the BO surface, and are not instantaneously in the ground state. In order to get rid of such unphysical fluctuations we compute the conductivity using Eq. 4.3, but expressing the polarization as:

$$P_\nu = \frac{1}{V}\left(q_+ \sum_I^{N_H} R_I^\nu + q_- \sum_I^{N_N} R_I^\nu\right), \tag{4.4}$$

where q_+ and q_- are mean effective charges for the two species, and are related by $3q_+ + q_- = 0$ through the charge neutrality. We estimate q_+ and q_- by averaging their values as obtained, at each MD step, equating the change in polarization computed *ab initio* with that computed using 4.4 . With this procedure we obtain for ammonia $q_+ = +0.6e$ and consequently $q_- = -1.8e$ in the superionic phase, and $q_+ = +e$ and $q_- = -3e$ in the fluid phase, indicating that in the fluid phase hydrogens move as bare protons and the system resembles a two component ionic liquid, where anions and cations are hydrogen and nitrogen atoms, respectively.

We then compute the conductivity using 4.3 and 4.4 for the fluid phase. Results are shown in Fig. 4.9 and can be compared with shock-wave experimental data. The agreement is rather good.

Since, as already observed, the ionic motion in the fluid phase is highly uncorrelated the conductivity obtained through the simple Nerst-Einstein relation:

$$\sigma = \frac{q_+^2 n_H D_H}{k_bT} + \frac{q_-^2 n_N D_N}{k_bT}, \tag{4.5}$$

where q, n and D are the charge, density and diffusivity of carriers, turn out to be at most 10% different from the reported values. This is however not true in the superionic phase, where hydrogens jumps are highly correlated. This forbids the evaluation of the conductivity for the superionic phase using 4.5. On the other hand, evaluating σ using 4.3 in the superionic phase, that is including correlations, was found to be unreliable because of large statistical fluctuations.

In order to find out a lower boundary for the pressure at which the superionic and superprotonic phases start to appear, we simulated ammonia at 30 GPa. Again, the system becomes plastic above 500 K, but increasing temperature further, contrary to what occours at 60 GPa, solid ammonia transforms directly into a molecular liquid around 1500 K. This places the triple point between liquid, superionic and solid between 30 and 60 GPa, and between 1000 and 1500 K.

Further simulations at 150 and 300 GPa have been made in order to complete the phase diagram. At both pressures the superionic phase boundary appears, within our resolution, at the same temperature as observed at 60 GPa. This suggests that, according to the Clausius-Clepeyron relation, the phase transition does not imply an appreciable volume change. The plastic phase, present at 30 and 60 GPa, did not appear in simulation runs at 150 and 300 GPa, where in fact no complete molecular rotations have been observed. However large random reorientations are still present above 500 K, making the system at least orientationally disordered.

A simulation, with a super-cell containing 31 molecules and a vacancy, has been done at 150 GPa to check the stability of the superionic phase against melting. Up to 2500 K the system was stable with the mean square displacement of nitrogen almost constant. However as soon as the temperature was increased to 3000 K the nitrogen lattice melts. Upon a subsequent cooling, the nitrogen

	30 GPa	60 GPa	150 GPa	300 GPa
ordered-plastic	~ 500K	~ 500K	—	—
plastic-molecular fluid	~ 1500K	—	—	—
plastic-superionic	—	~ 1000K	~ 1000K	~ 1000K
superionic-ionic fluid	—	~ 2000K	~ 3000K	~ 4000K
ionic fluid-metallic	—	—	—	~ 5500K

Table 4.3: Calculated phase boundaries.

lattice frizes below 3000 K, although not in a crystalline structure, while hydrogens continue to diffuse.

Melting temperatures values are reported in Tab. 4.3 together with other phase boundary temperatures.

In Fig. 4.8 we sketch the high-pressure high-temperature ammonia phase diagram as results from our simulations. Gray regions represent our uncertainty obtained cycling between the two phases (hysteresis loop). They are mainly due to the small cell size and short simulation time.

At pressures above 60 GPa the melting line is much higher than that extrapolated from low pressure data, possibly due to the presence of the superionic phase and the changes in the hydrogen bond interaction.

It is interesting to note that the fluid phase is characterized by three different regimes: molecular, ionic and metallic. In the molecular regime molecules are intact, while in the ionic one they are completely dissociated, resembling a molten salt. The crossover between the two regimes is characterized by an exponential increase in the number of dissociated molecules, and thus of the protonic carriers. The metallic regime is characterized by the closure of the electronic gap induced by the temperature. This regime is certainly characterized by an electronic conductivity which is typically a few orders of magnitude higher than in the ionic regime. However a precise calculation of the conductiv-

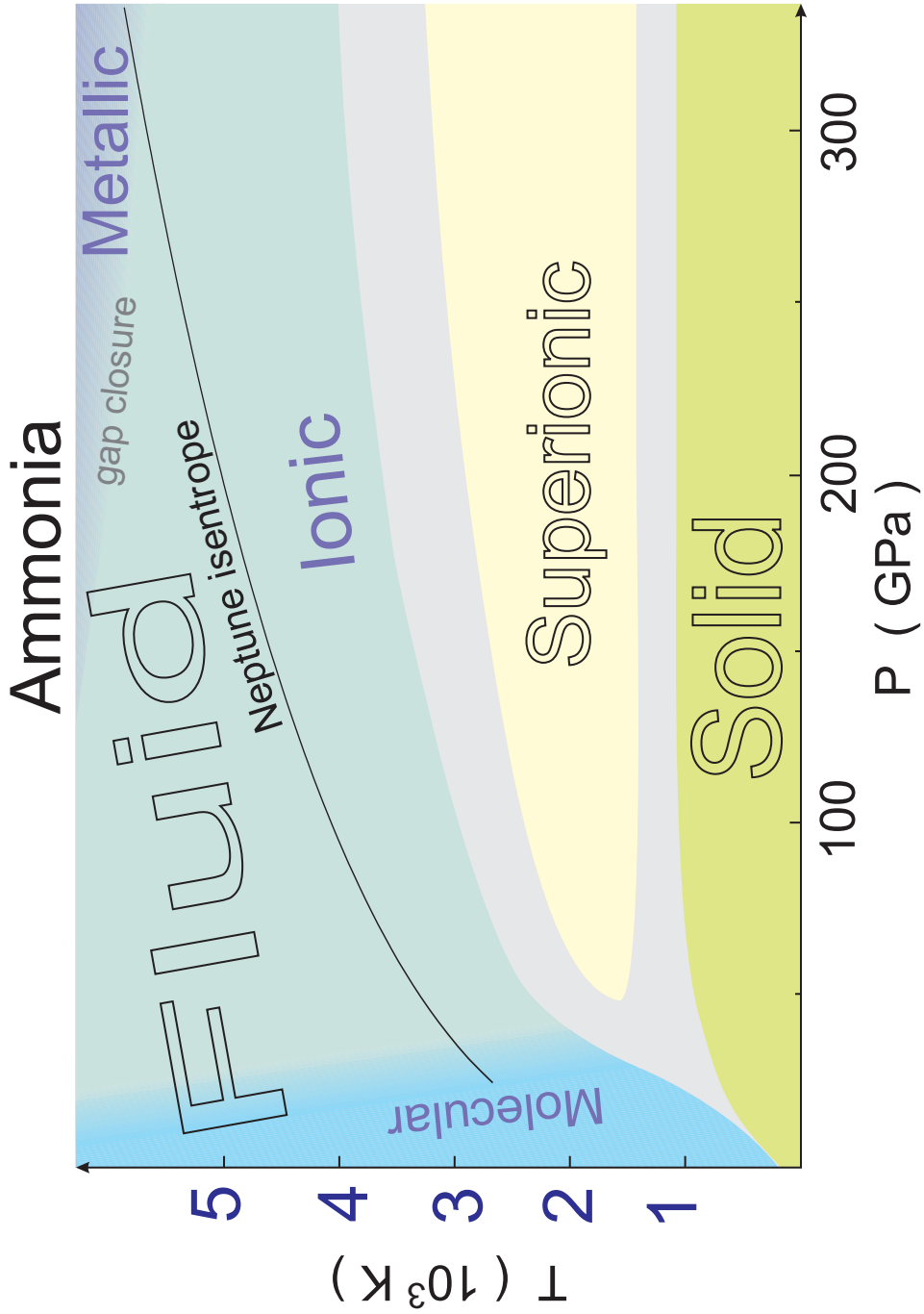

Figure 4.8: Phase diagram of Ammonia as emerged from the *ab initio* simulations. At fixed pressure the temperature has been increased from 300 to 7000 K. The gray regions indicate the error bar on the predicted phase boundaries, their size is estimated from the simulated hysteresis loop.

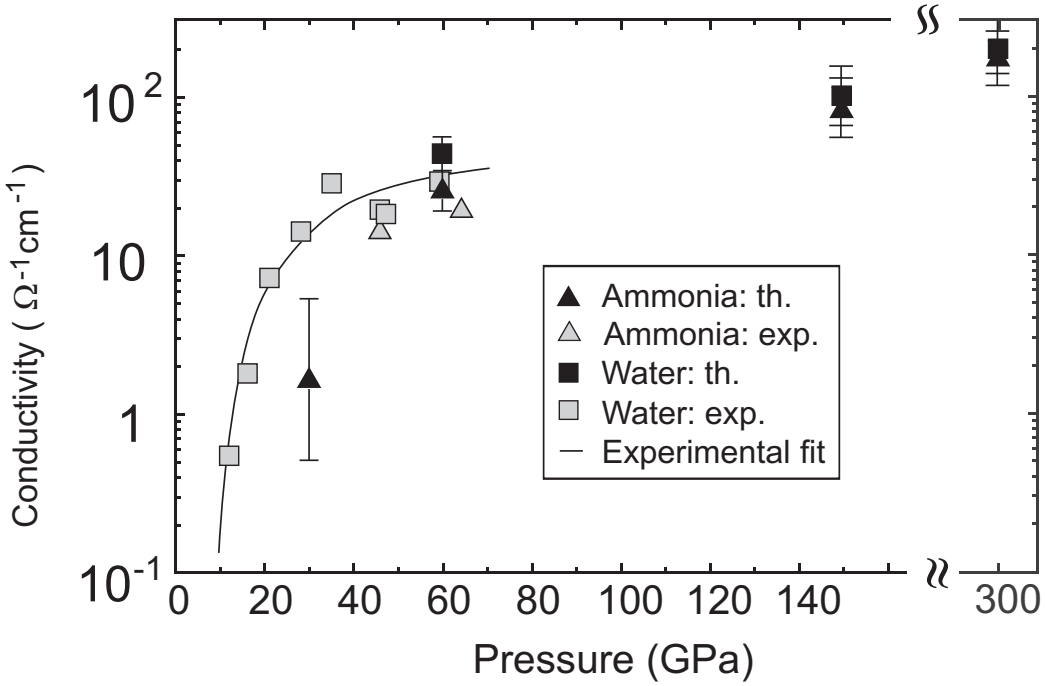

Figure 4.9: Ionic conductivity data for water and ammonia, as computed in the simulation and measured in shock-wave experiments (water Ref. [47], ammonia Ref. [45]). The continuous line is an experimental fit of the conductivity of water [43]. The experimental data are taken along the shock-Hugoniot which is close to the Uranus isentrope. Theoretical data at 60 GPa and 150 GPa correspond to 3000 K and 4000 K respectively. Experimental temperatures are: 3500 K at 48 GPa and 4400 K at 61 GPa in ammonia [60], and 3800 K at 59 GPa in water [61].

ity, in the metallic regime has not been attempted yet.

4.2 Water

Water is by far one of the most studied molecules in nature, and its high-pressure high-temperature behavior is particularly relevant in planetary physics. For a detailed overview of the high-pressure low-temperature behavior of water we refer to the article of M. Bernasconi *et al.* [62]. The high-pressures high-

temperatures region of the phase diagram has been investigated experimentally through shock-waves. Conductivities up to ~ 80 GPa and the equation of state up to ~ 150 GPa have been measured [43, 47, 61, 60].

The low temperature crystal structure of water up to 300 GPa is known from previous theoretical and experimental work. The crystalline structure at room temperature and for pressure in the range 2-60 GPa is ice VII [32, 63, 64]. Above 60-80 GPa ice VII is believed to transform into the symmetric hydrogen-bonded ice X structure (space group $Pn\bar{3}$) [33, 65, 55]. In this phase the crystal structure is of the cuprite type and the picture of ice as a molecular crystal breaks down entirely. Both in ice VII and ice X oxygen atoms form a body-centered-cubic (bcc) sublattice (Fig. 4.10 a, red circles). Hydrogens, that in ice X sit in the middle of the O-O separation and are slightly off-center in ice VII, occupy four of the eight allowed nearest neighbor distances, designing an ideal tetrahedron. Two of such tetrahedron are possible (Fig. 4.10 b, blue and green tetrahedron), and the structure of the ice X can be seen as the compenetration of two simple cubic oxygen sublattices, the first with nearest hydrogens in a given tetrahedron configuration and the second with nearest hydrogens in the other one (see Fig. 4.10 a, A and B sublattices). The existence of ice X, first inferred from spectroscopy [65] but not yet observed directly, has been confirmed by *ab initio* molecular dynamics, that yielded a transition pressure of 102 GPa by treating the protons as a classical particles [33], and of 72 GPa treating them as quantum particles [34].

Three runs has been performed in the high-pressure high-temperature region of the PT phase diagram, at 60, 150 and 300 GPa. Our low temperature starting configuration has been the ice VII structure at 60 GPa and ice X phase at 150 and 300 GPa. After an equilibration at 300 K, by increasing temperature at all

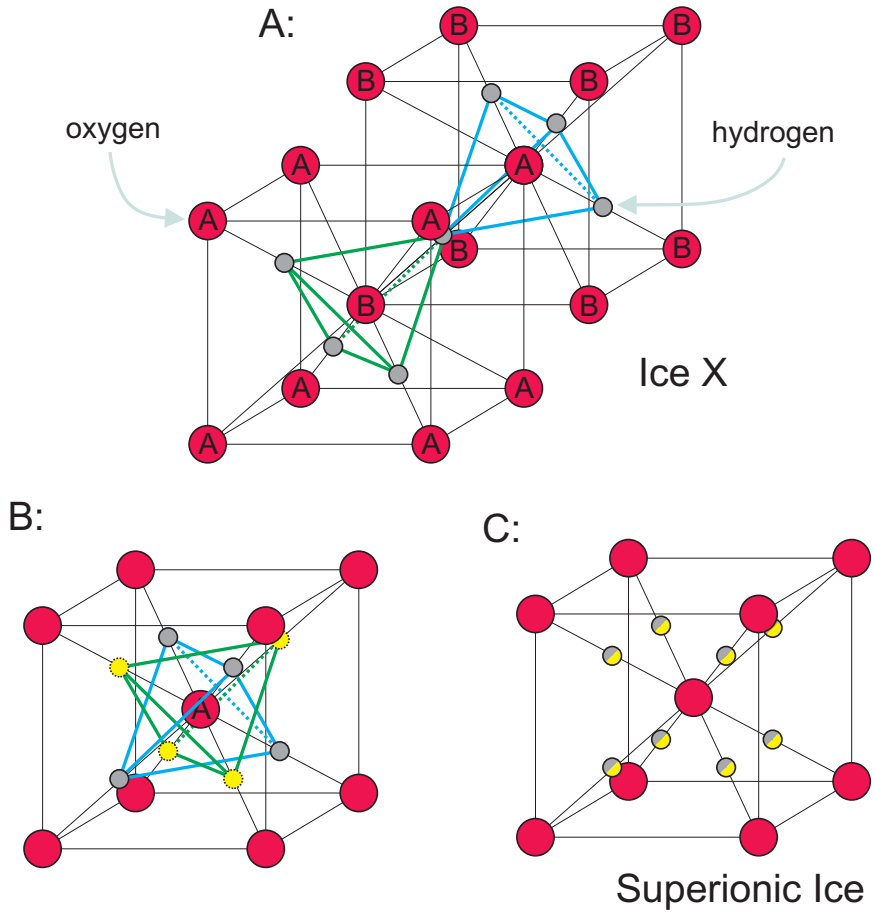

Figure 4.10: Symmetric and Superionic Ice X structures. A: cuprite structure of ice X with oxygen atoms forming a bcc lattice and with hydrogens sitting on the bond center position. B: the two possibles tetrahedral configuration of hydrogens around an oxygen atoms. C: Structure of Superionic Ice X, all allowed bond symmetric site are visited with equal probability by diffusing hydrogens.

three pressures we have seen an abrupt transition taking place around 2000 K, after which the protons become highly diffusive ($D_H^{water}(150\,GPa, 2500\,K) = 6 \cdot 10^{-4} cm^2/s$), similarly to what observed in ammonia. Again we have located the transition looking at the m.s.d. of hydrogen and oxygen atoms separately, and with a subsequent visual inspection of the trajectories.

In this superionic phase the oxygen atoms still vibrate around the bcc lattice positions of crystalline ice VII and X. Proton diffusion occurs via jumps among equivalent site along the O-O separation (Fig. 4.10 c, gray-white circles). At 150 GPa in the superionic phase all sites of both tetrahedra are equally visited by hydrogens leading to the $Pn\bar{3}m$ space group. This can easily be monitored, across the phase transition, with the help of the following order parameter:

$$\eta = \frac{1}{N_o c_h} \sum_{i=1}^{N_o} (h_i^{occ.} - h_i^{unocc.}) \,, \tag{4.6}$$

where N_o is the number of oxygens in the simulation cell, c_h is the coordination of hydrogens with respect to oxygen, that is always 4. As already stated, the hydrogens, in ice X, can be arranged in two different tetrahedral configurations (blue and green tetrahedron in Fig. 4.10a) around the oxygens. An oxygen atom, therefore, is classified (A or B type) depending on the configuration of its nearest hydrogens. Oxygens of type A and B (see Fig. 4.10a) form two simple cubic compenetrating sublattices. We mark as occupied site the blue(green) tetrahedron vertices around an oxygen of type A(B) (gray circles in Fig. 4.10a), and as unoccupied site the green(blue) tetrahedron vertices around an oxygen of type A(B) (yellow circles in Fig. 4.10a). In Eq. 4.6 $h_i^{occ.}$ and $h_i^{unocc.}$ for each oxygen in the simulation cell are the number of hydrogens in sites marked as occupied and unoccupied. This can be understood with the help of Fig. 4.10b where the oxygen type is A, $h_i^{occ.}$ is the number of hydrogens occupying gray

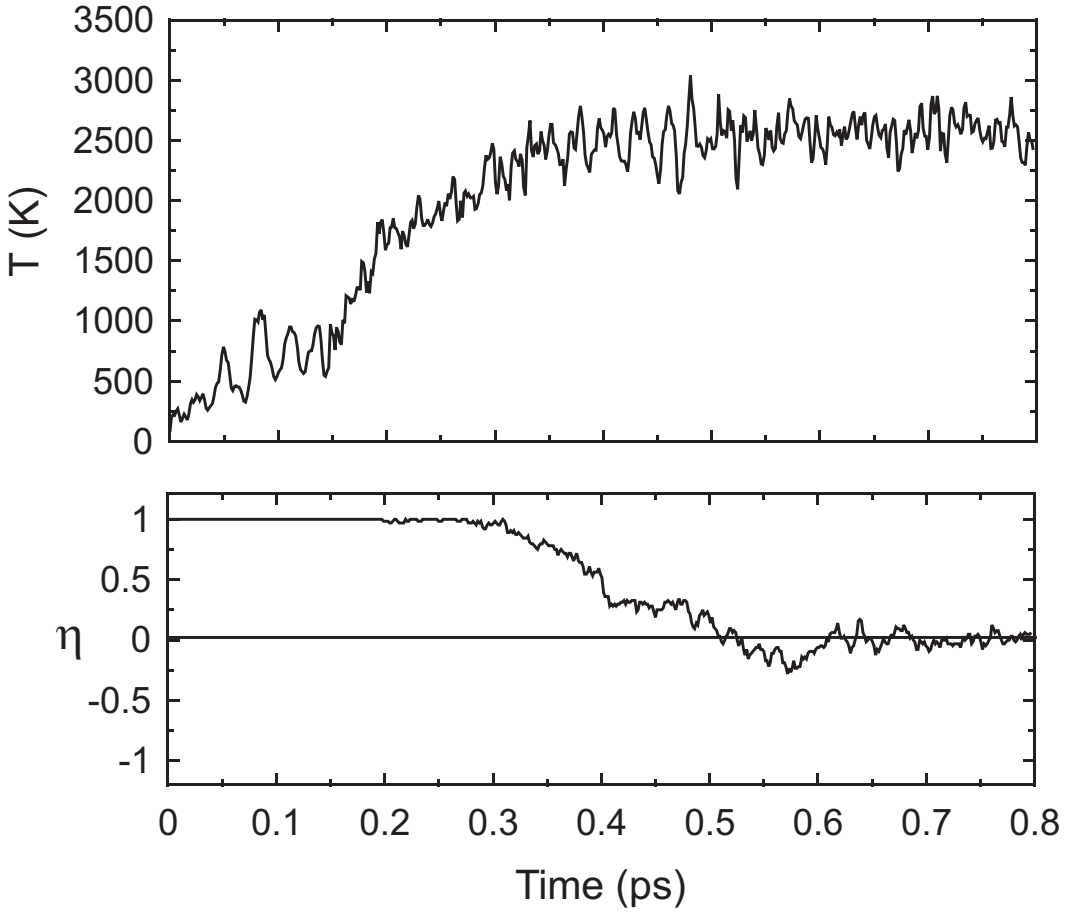

Figure 4.11: Simulation run of water at 150 GPa across the solid-superionic phase boundary. Upper panel: temperature of the system, lower panel: order parameter of the Eq. 4.6 .

circles positions and $h_i^{unocc.}$ is the number of hydrogens occupying white dotted circles. With this definitions $\eta = 1$ for the ice X configuration (all hydrogens in sites marked as occupied), $\eta = -1$ for its complementary configuration (all hydrogens in sites marked as unoccupied), i.e. exchange oxygen sublattice type, and $\eta = 0$ for a configuration were all eight sites are occupied with equal probability independently on the sublattice type (Fig. 4.10c). In Fig. 4.11 we report the values of η during a run at 150 GPa where the system becomes superionic. Within this phase η approaches zero indicating that in the system there is no memory of the sublattices type A and B, i.e. all sites allowed for hydrogen are equally visited. In order to confirm that the preferred position for hydrogens are still the bond centers we record the positions of oxygens and hydrogens in the superionic phase and we plot the mean density of hydrogens and oxygens in 3D, see Fig. 4.12. As expected oxygens are still in their equilibrium positions while the density of hydrogens is peaked at the middle of any O-O distance. At 60 GPa, instead, water is in the ice VII structure, and along the O-O distance there are two equilibrium positions allowed to hydrogens. This slightly complicates the situation because it doubles the number of sites between which hydrogen jumps occur. If one considers the two neighboring sites along O-O distance to be the same site [3], and performs the same analysis as above the overall picture is unchanged. Actually, inside the superionic phase there is a smooth transition between the two regimes while the barrier at the middle of O-O distance is lowering due to volume decrease.

At 300 GPa the transition to the superionic phase involves also a change in the crystalline structure of oxygen sublattice from ice X to ice XI. Ice XI has been discovered and characterized by Benoit *et al.* [33], using *ab initio* constant

[3] this approximation is correct as long as the energy barrier between neighboring sites along the same O-O distance is much lower than the energy barrier between sites on different O-O distances

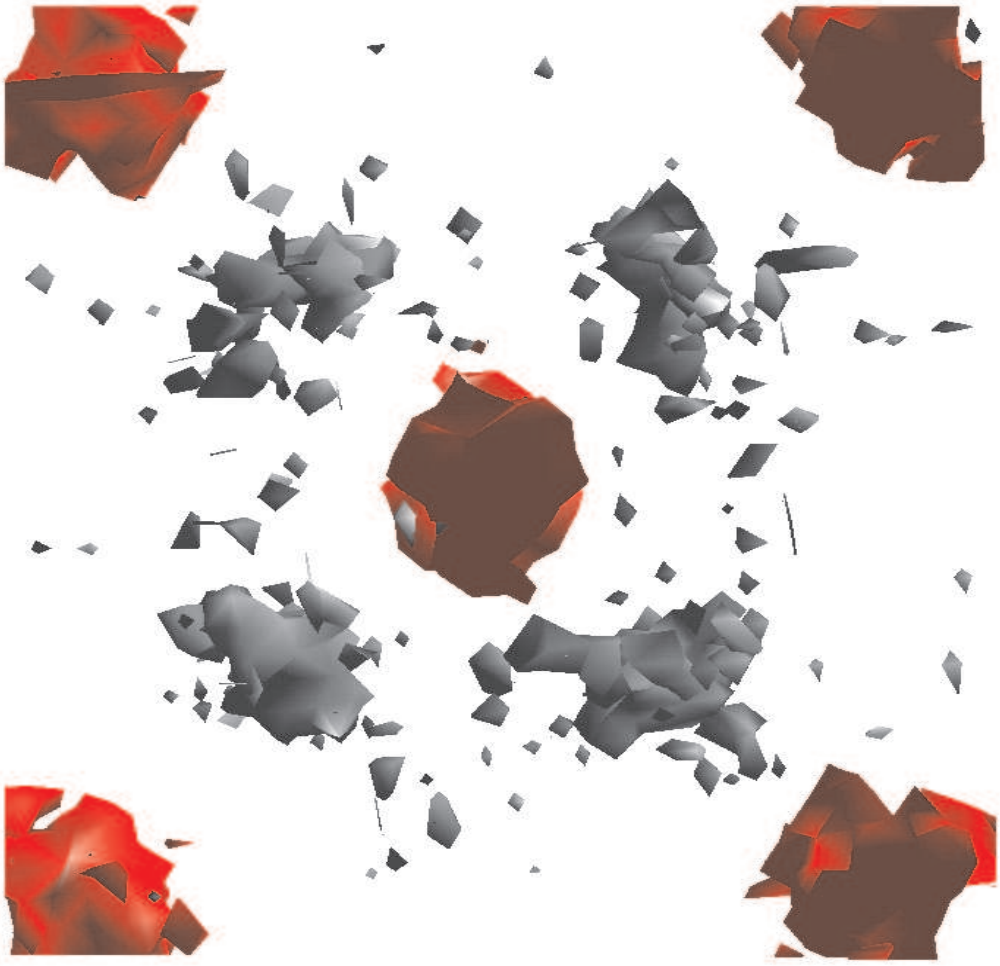

Figure 4.12: Density of hydrogens (gray) and oxygens (red) in the superionic phase of water at 150 GPa.

pressure molecular dynamics. In particular they found a transition from ice X to ice XI at room temperature between 300 and 400 GPa. Figure 4.13 shows the calculated oxygen-oxygen and oxygen-hydrogen pair correlation functions at 300 GPa of: ice X at 1000 K (solid phase), ice X at 2000 K before the transition and superionic ice again at 2000 K after the transition. During the superionic phase the positions the peaks in the oxygen-oxygen pair correlation function, move from those of ice X to those of ice XI (see Figs. 4.15 and 4.14 lower panel), and the coordination with the nearest neighbor changes from 8 to 12 (see Figs. 4.15 and 4.14 upper panel).

A further increase in temperature ($T > 3500\,K$ depending on the pressure) leads to the melting of the oxygen sublattice, ($D_O^{water}\ (150\,GPa, 4000\,K) = 3 \pm 1.5 \cdot 10^{-5} cm^2/s$), but only to a slight increase in the proton mobility ($D_H^{water}\ (150\,GPa, 4000\,K) = 1.8 \cdot 10^{-3} cm^2/s$), which varies with continuity across the melting line. As in the case of ammonia this fluid is dissociated, and resembles a two-component ionic liquid (molten salt). As anticipated in the previous section cross correlation between atoms displacements are negligible in the fluid phase, and the mean effective charge of the hydrogens is e. Using the relation 4.3 we calculate the conductivity of water, near to the planetary isentrope, its values are reported in Fig. 4.9, and the agreement with the experimental data, where they exist, is rather good. It has to be noted that if we use the expression 4.5, in the fluid phase, the contribution coming from the diffusivity of oxygen atoms is about the 10% that of the hydrogens (protons) ($D_H^{water}(300\ GPa, 5000\ K) = 2 \cdot 10^{-3} cm^2/s$) ($D_O^{water}\ (300\ GPa,\ 5000\ K) = 8 \cdot 10^{-5} cm^2/s$). At 300 GPa and 5000 K along the planetary isentrope, the predicted conductivity of water and ammonia are $200\ (\Omega\,cm)^{-1}$ and $170\ (\Omega\,cm)^{-1}$ respectively.

With decreasing pressure in the fluid phase a cross-over from ionic to molec-

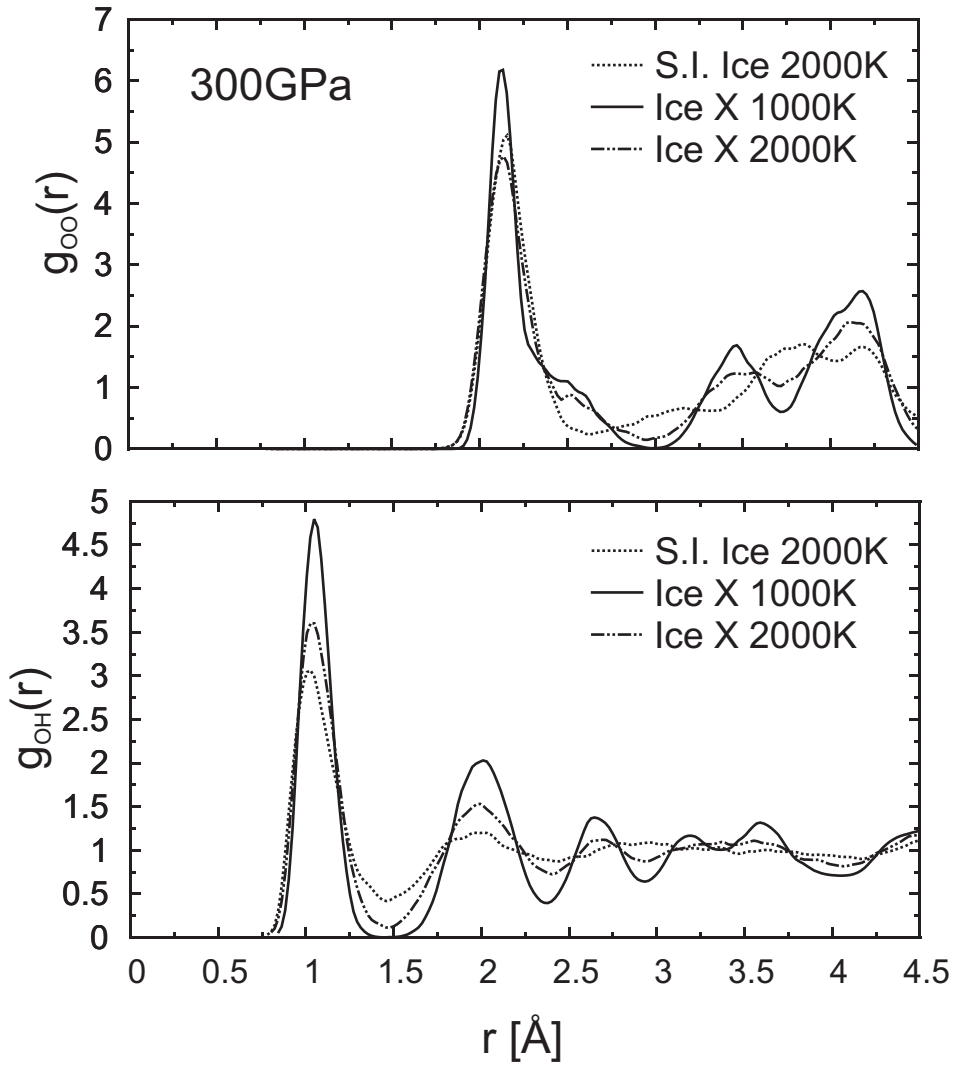

Figure 4.13: Oxygen-oxygen (upper panel) and oxygen-hydrogen (lower panel) pair correlation functions at 300 GPa of: ice X at 1000 K (solid phase), ice X at 2000 K before the transition and superionic ice again at 2000 K after the transition.

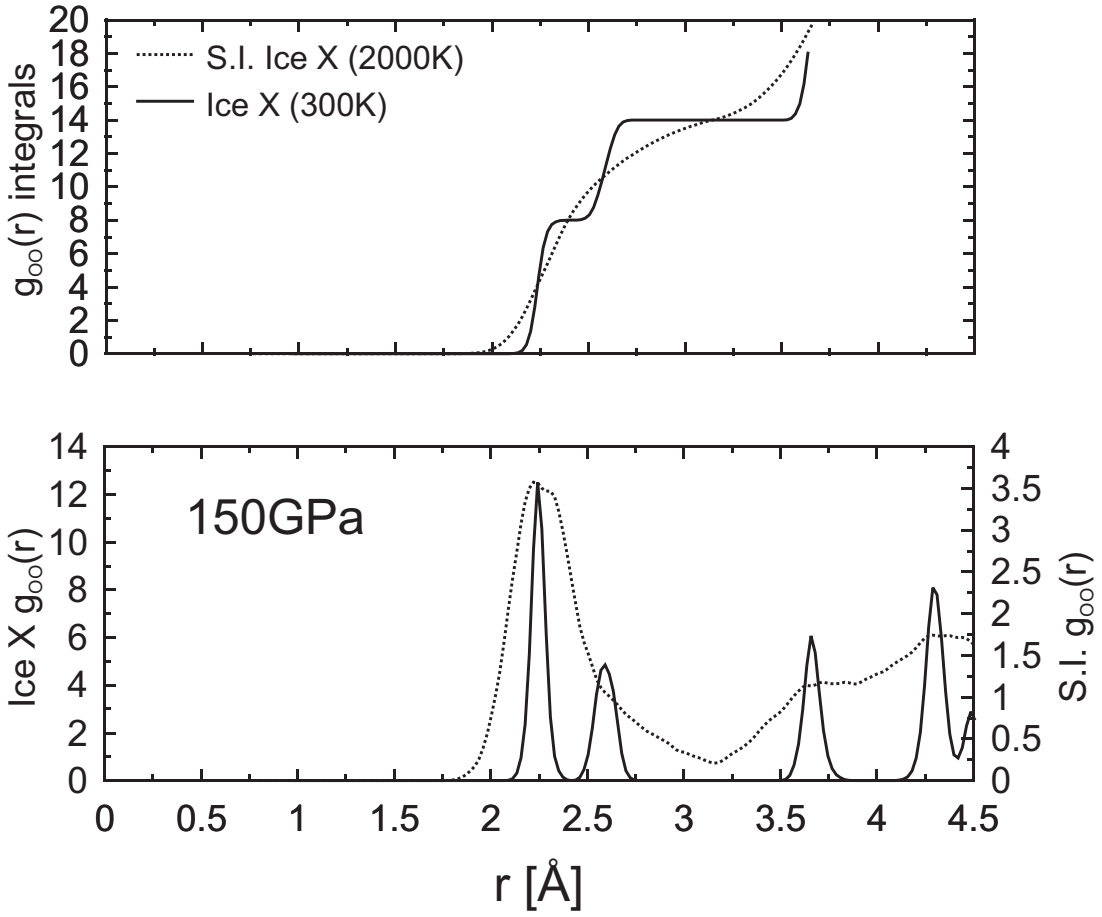

Figure 4.14: Ice X (solid phase, 300 K) and superionic ice X (2000 K) oxygen-oxygen pair correlation functions (lower panel) and its integral (upper panel) at 150 GPa.

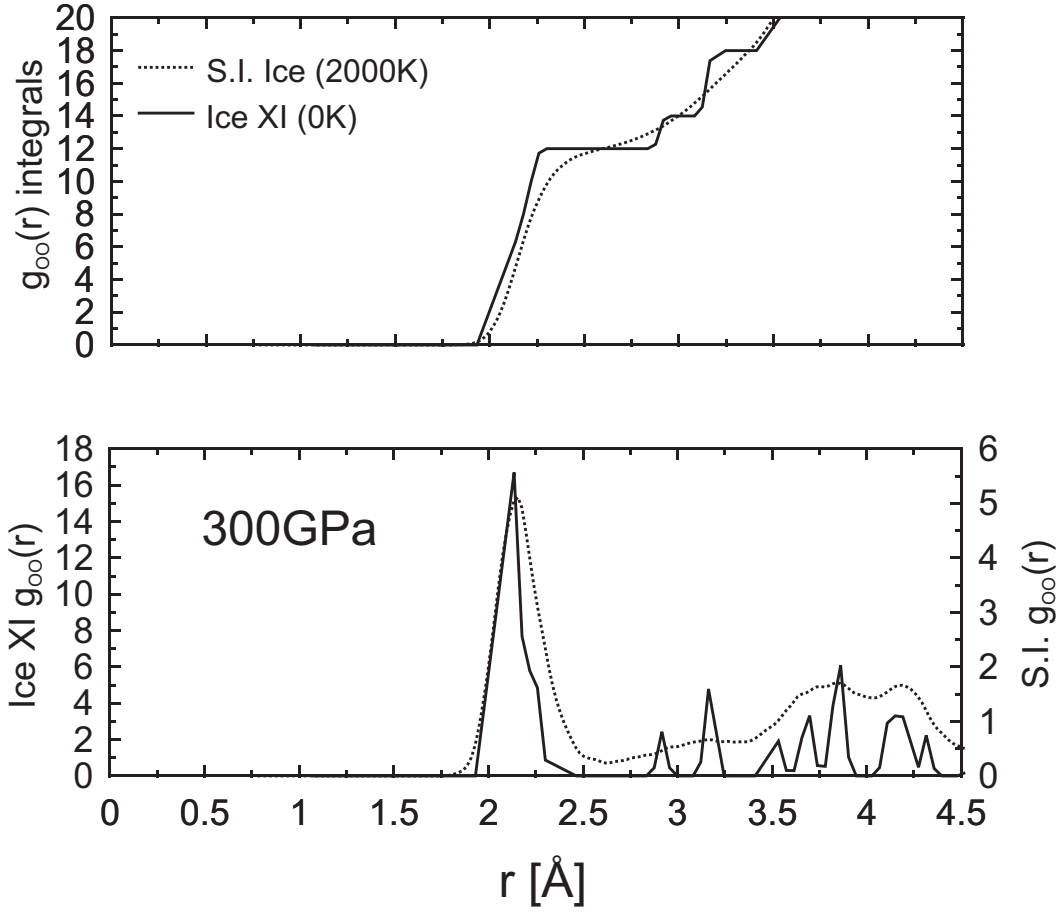

Figure 4.15: Ice XI (solid phase, 0 K) and superionic ice XI (2000 K) oxygen-oxygen pair correlation functions (lower panel) and its integral (upper panel) at 300GPa.

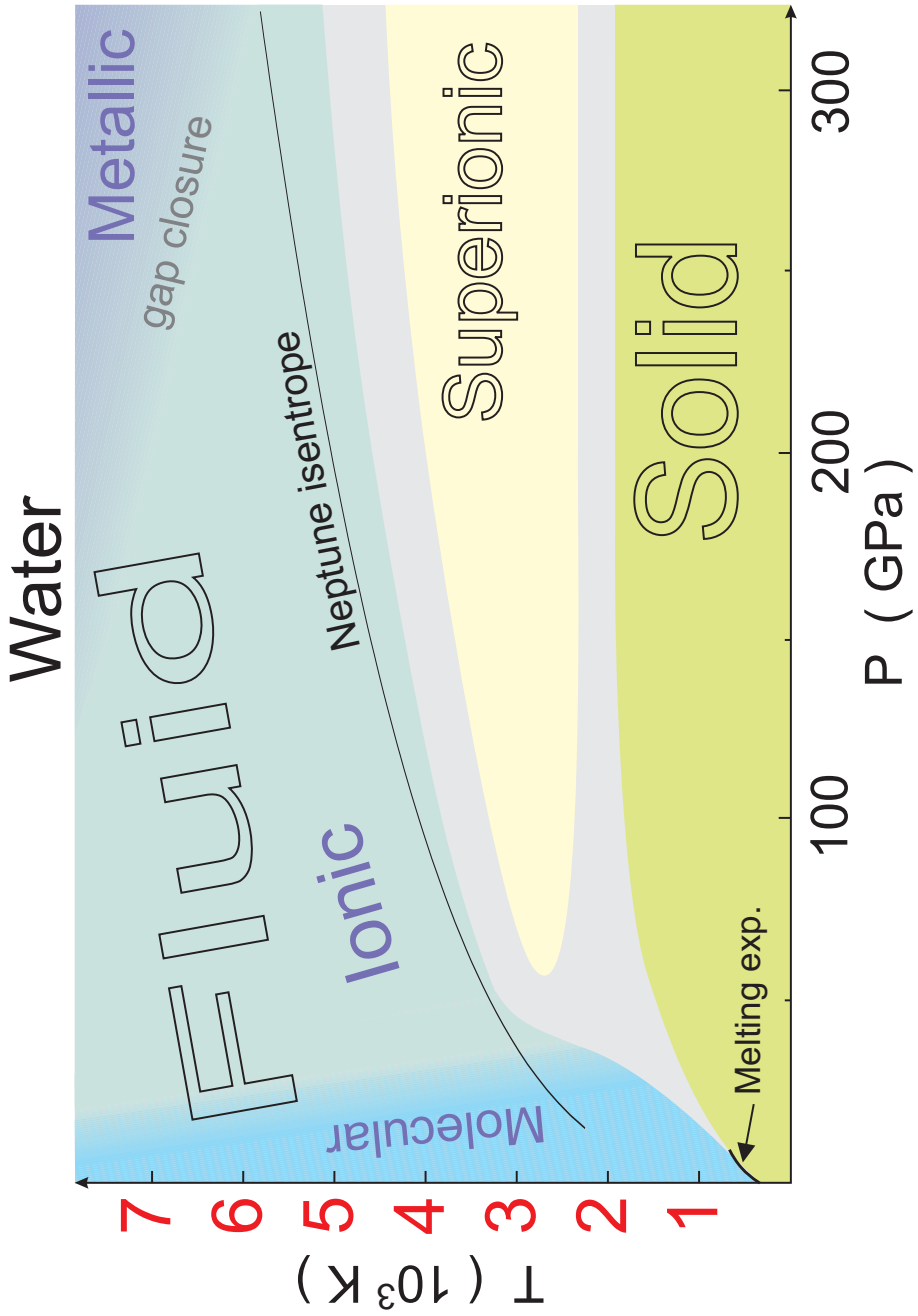

Figure 4.16: Phase diagram of Water as emerged from the *ab initio* simulations. At fixed pressure the temperature has been increased from 300 to 7000 K. The gray regions indicate the error bar on the predicted phase boundaries, their size is estimated from the simulated hysteresis loop. The Neptune isentrope is taken from Ref. [39]. The experimental melting line of water at low pressure is taken from Ref. [66]

ular liquid is obviously expected. In ammonia (see above) the cross-over lies between 30 and 60 GPa. We have not attempted to simulate water at pressures below 60 GPa and therefore the position of the molecular-ionic boundary in the fluid region of Fig. 4.16 is somehow arbitrary and chosen to be the same as in ammonia. Our results provide also a simple interpretation of the experimental pressure dependence of the conductivity. At low pressures molecular water exhibits a low ionic conductivity arising from dissociated molecules. By increasing pressure the number of dissociated molecules (and thus of the protonic carriers) increases exponentially across the molecular-ionic cross-over. In the ionic regime all the protons contribute equally to the conductivity and a further increase in pressure increases only slightly the proton mobility and concentration, without changing the number of carriers .

Both the superprotonic solid state and the ionic liquid state reveal an electronically insulating character, as shown by the electronic density of states at 300 GPa, reported in Fig. 4.18. At low temperatures filled and empty states are separated by a gap 10 eV wide, which decreases continuously with increasing temperature in the superionic (2500 K) and fluid (5000 K) phases. Finally at 7000 K the fluid gradually turns metallic, as suggested by the finite density of states at the Fermi level in Fig. 4.18. The same behavior is observed at lower pressures (150 GPa), where the metalization temperature is found to be slightly higher. In Fig. 4.17 (lower panel) we also report the energy of the highest filled states (continuous lines) and of the lowest empty states (dotted lines) for our simulation cell, as a function of time, during a simulation run. Again this points to a value of about 7000 K for the metalization temperature at 300 GPa.

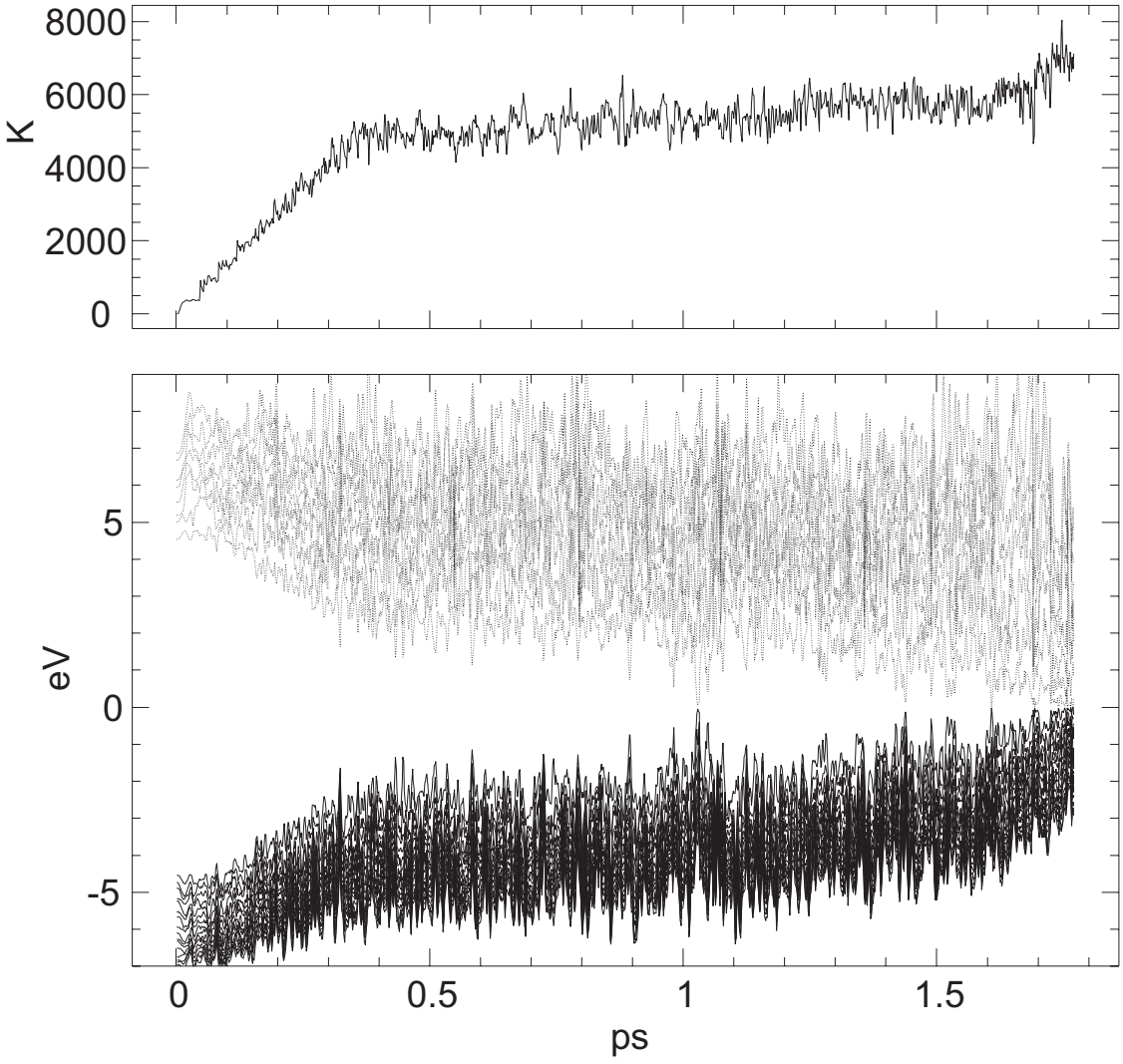

Figure 4.17: Evolution of the Kohn-Sham electronic states in water at 300 GPa in the heating process. Upper panel : temperature during the simulation run. Lower Panel : last 16 filled (continuous lines) and first 8 empty (dotted lines) Kohn-Sham states.

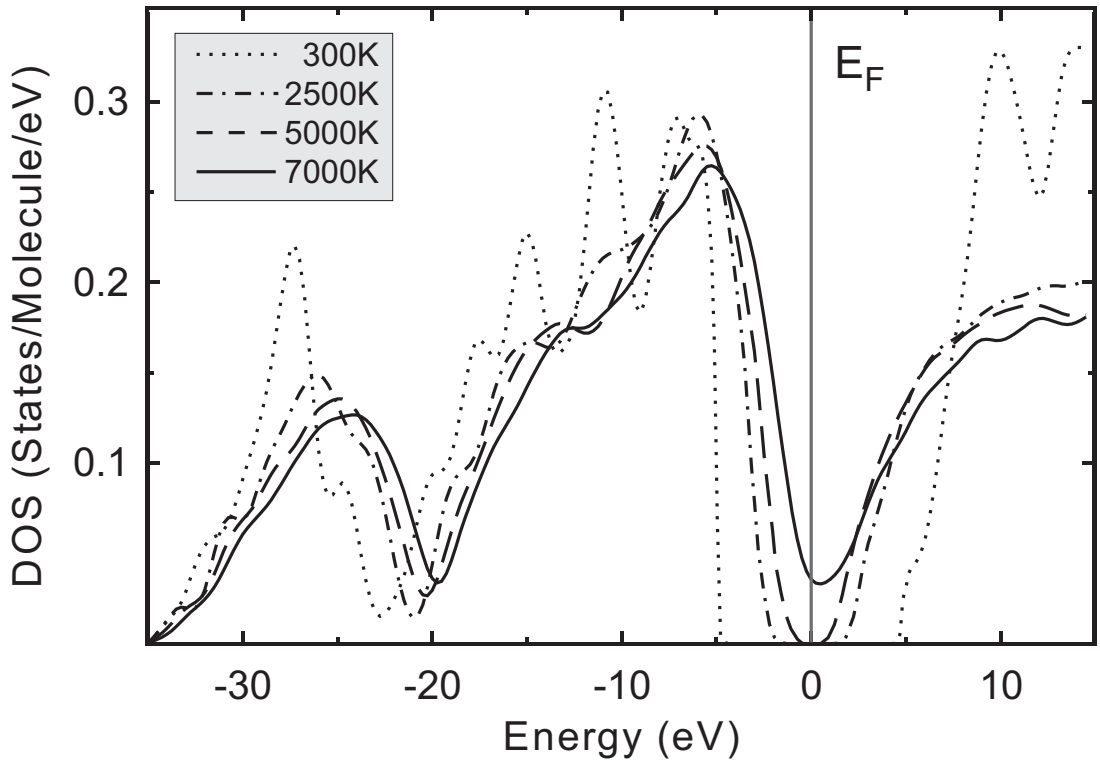

Figure 4.18: Electronic density of states of water at 300 GPa in solid ice X, superionic ice, ionic fluid and metallic phases.

4.3 Planetary physics

In the previous sections we have presented *ab initio* molecular dynamics simulations aimed at gauging the phase diagram of water and ammonia in the range of pressure and temperature of the planetary ice layer. The simulations also yield the equation of state (pressure-vs-density) of water and ammonia (Fig. 4.19) needed for the calculation of the radial density distributions to be compared with those derived from the gravitational field measured by spacecraft. Moreover, the simulations provide data on the electrical conductivity needed for the calculation of the magnetic field generated by the planetary dynamo. At the conditions of the Neptune isentrope both species are fluid and fully dissociated in a two component plasma. In the fluid phase both species display a protonic conductivity of the order of 10-100 $(\Omega\, cm)^{-1}$, sufficiently large to sustain the dynamo generation of the planetary magnetic field. Only at higher temperatures ($\geq$ 7000 K in water and $\geq$ 5500 K in ammonia at 300 GPa) do the fluids become metallic.

The computed equations of state of water and ammonia close to the Neptune isentrope are compared in Fig. 4.19 with shock-wave data. Previous theoretical results on methane [1] and the shock-wave measurements on "synthetic Uranus" [43] are also included. By using the additive volume law [67] we estimated the pressure versus volume curve of the mixture of water, ammonia and methane in solar proportions. The results (crosses in Fig. 4.19) are in good agreement with shock-wave data available for "synthetic Uranus" and provide an estimate of the equation of state of ices mixture at higher pressure and temperature.

We can now outline the consequences that the above results may have on the

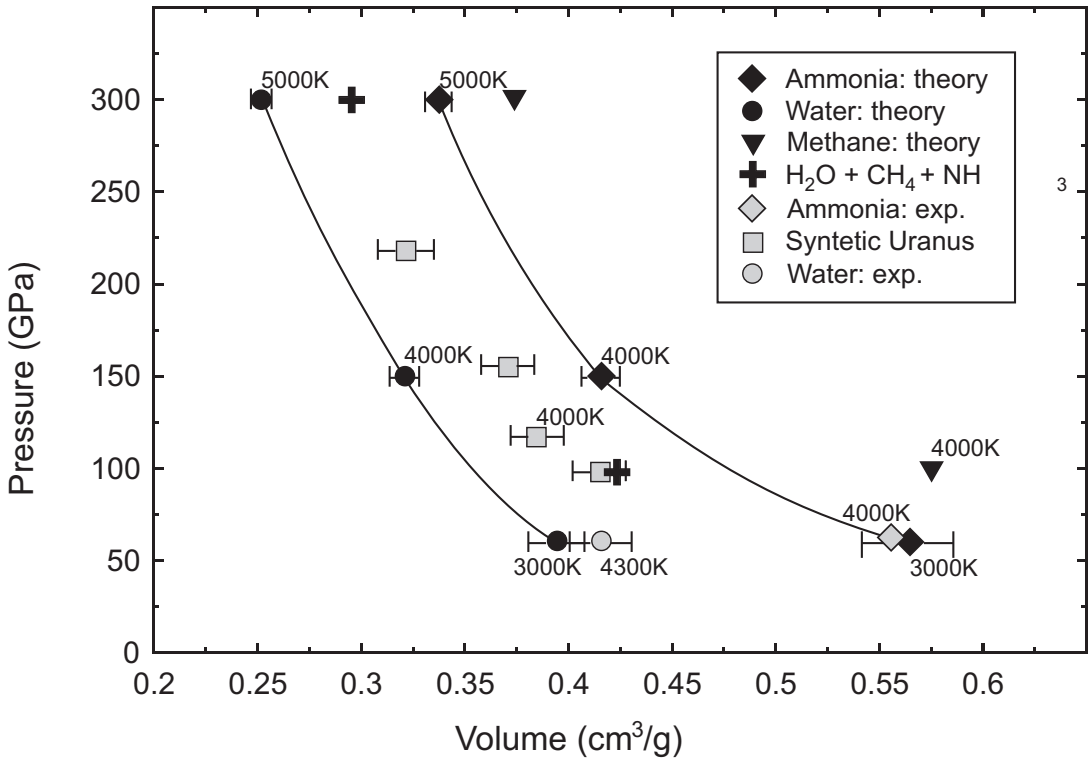

Figure 4.19: Pressure versus volume curves of water and ammonia along the planetary isentrope from shock-wave experiments and the present simulations. Theoretical data for methane from Ref. [1] are also reported. Shock-wave data of "synthetic Uranus" (Ref. [43], see text) are compared with the equation of state obtained from the theoretical points of methane, ammonia and water in the figure and by using the additive volumes law [67]. Experimental data of ammonia and water are from Ref. [45] and Ref. [47] respectively.

understanding of the ice layers of Uranus and Neptune. The precise location of the planetary isentrope in Fig. 4.16 is subject to large uncertainties depending on the model of the planet's interior. Within the uncertainties of our simulations, we find that the melting line runs below all the presently accepted planetary isentrope of Neptune [39, 68] (see Fig. 4.16), confirming that planetary ices are in the fluid state. Within the fluid phase three distinct behaviors have been observed: a molecular regime at low pressure, a non-metallic ionic regime at intermediate pressure and temperature and a metallic regime at high pressure and temperature. Along the Neptune isentrope both NH_3 and H_2O components of the ice layer are predicted to be electronically insulating up to 300 GPa. Thus the electrical conductivity in the outer part of the ice layer can only come from the large proton mobility in the ionic liquid phase. Indeed our computed ionic conductivity is in excellent agreement with shock-wave data measured up to 60 GPa, as shown in Fig. 4.9. The simulation further allows us to compute the ionic conductivity at higher pressures not reached in shock-wave experiments.

Moving deeper into the planet, the ice-core boundary is met at 600 GPa and 7000 K according to the presently accepted Neptune isentrope [39]. At these conditions we predict water and ammonia to be metallic. A model of the dynamo generation of the magnetic field should therefore include both the contribution of the high electronic conductivity due to the metallic H_2O and NH_3 liquid in the inner part, and the lower electrical conductivity due to the proton mobility in the H_2O and NH_3 electronically insulating ionic liquid in the outer part of the ice layer. However, it must be noted that alternative models of the giant planets have been proposed which assume that above 150 GPa the interior is isothermal at a temperature of $\sim$5000 K [69]. In this latter case the ices will keep electronically insulating in the whole planet.

Chapter 5

Conclusions

The main result of this thesis is the determination of the very-high-pressure and temperature phase diagram of water and ammonia by means of *ab initio* constant-pressure molecular dynamics.

A new superionic phase has been found above 60 GPa between the solid and the fluid phases, both in water and ammonia. Due to the presence of this new phase, the melting lines of water and ammonia are pushed at much higher temperature than those predicted by extrapolating available low pressure data, and the melting line of water lies near the planetary isentrope. In the fluid phase of both molecules we have found and characterized an insulating ionic regime with complete molecular dissociation, that becomes metallic upon heating at very high pressure ($T>7000$ K for water and $T>5500$ K for ammonia, at 300 GPa).

The simulations also show that at room temperature hydrogen bonds in ammonia remains asymmetric up to a pressure of at least 300 GPa. This is at variance with water, where hydrogen bonds symmetrization occurs at $\sim$300 GPa.

The conditions of pressure and temperature considered in this thesis are typical of the interior of giant planets Uranus and Neptune. Implications on the physics of these planets have been discussed.

In particular, we have shown that the planetary isentrope (according to the current planetary models) runs above the melting line of water and ammonia, which implies that the middle ice layer is in the fluid state. In this state the molecules are fully dissociated and the electrical conductivity arising from the mobility of protons is large enough to sustain the dynamo mechanism for the generation of the planetary magnetic field. The theoretical results on the equation of state and electrical conductivity are in good agreement with experimental data available at low pressure (up to 60 GPa) and provide reliable predictions of the behavior of water and ammonia at the conditions of the inner part of the ice layer (300 GPa and 5700 K) not reached in shock-wave experiments. Near the ice-core boundary (600 GPa and 7000 K) we predict water and ammonia to be metallic. Moreover our results allow a simple explanation of the experimentally observed behavior of the conductivity as a function of pressure.

All the above results were made possible by the development of a highly efficient parallel code for the *ab initio* molecular dynamics, capable of exploiting the computational power of present supercomputers. The code has been designed as architecture-free, and displays an almost linear speed-up, in a wide range of number of processors, on many massively parallel supercomputers.

We conclude with a few perspectives for future work. A better characterization of the superionic phase, mainly of the mechanism of proton diffusion

would be required, especially in the range of pressures and temperatures nowadays accessible experimentally by laser-heated diamond anvil cell techniques. Moreover, a study of the properties of binary and eventually ternary mixtures of water, methane and ammonia at planetary conditions would be extremely important to confirm that the present understanding of planets interior, based on the separate study of the three species, is not affected by their mutual interaction. Of particular relevance would be, for example, the case of the ternary mixture of solar proportions, that should closely resemble the composition of the ice layers of Uranus and Neptune.

Chapter 6

Appendix

6.1 Orthogonalization and Parallel Diagonalization

In this brief appendix we will explain how the orthogonalization of the wave-functions is performed assuming velocity Verlet algorithm [70] and Fourier acceleration [71] for time integration, and using the method of Ryckaert*et al.* [72] for constrained dynamics.

The constraints to be satisfied during the dynamics are the set of equations:

$$< \psi_i(t+\Delta t)|\psi_j(t+\Delta t) >= \delta_{ij}, \tag{6.1}$$

where $\psi_i(t+\Delta t)$ are the wave-functions at time $t+\Delta t$, obtained as:

$$\psi_i(t+\Delta t) = 2\psi_i(t) - \psi_i(t-\Delta t) - \frac{(\Delta t)^2}{\mu}\left[\frac{\delta E_{tot}(t)}{\delta \psi_i^*} - \sum_j \Lambda_{ij}(t+\Delta t)\psi_j(t)\right]. \tag{6.2}$$

Λ is the matrix of the Lagrange multipliers and μ is the fictitious electronic mass. Substituting Eq. 6.2 into 6.1 we obtain the matrix equation for the Lagrange multipliers:

$$A + \lambda B + B^{+}\lambda^{+} + \lambda C \lambda^{+} = 1 \tag{6.3}$$

with

$$\lambda = \Delta t^2 \Lambda^{*}(t + \Delta t)/\mu, \tag{6.4}$$

$$A_{ij} =< \bar{\psi}_i | \bar{\psi}_j >, \tag{6.5}$$

$$B_{ij} =< \psi_i(t) | \bar{\psi}_j >, \tag{6.6}$$

$$C_{ij} =< \psi_i(t) | \psi_j(t) >, \tag{6.7}$$

where

$$\bar{\psi}_i = 2\psi_i(t) - \psi_i(t - \Delta t) - \frac{(\Delta t)^2}{\mu} \frac{\delta E_{tot}(t)}{\delta \psi_i^{*}} \tag{6.8}$$

are the unconstrained wave-function at time $t + \Delta t$. With the introduction of the Fourier acceleration the fictitious mass μ is no more a constant but a matrix in the Fourier space whose element are

$$\Theta_{GG'} = \frac{\mu}{min\{\mu, \mu_c/G^2\}} \delta_{GG\prime}, \tag{6.9}$$

where μ is the electronic mass without Fourier acceleration, μ_c is a cut-off (as a lower bound) on the wave-function to be accelerated and G, G' are reciprocal space vectors. We could still use the equation 6.3 redefining the various quantity in the following way:

$$\lambda = \Delta t^2 \Lambda^{*}(t + \Delta t), \tag{6.10}$$

$$B_{ij} =< \Theta^{-1} \psi_i(t) | \bar{\psi}_j >, \tag{6.11}$$

$$C_{ij} =< \Theta^{-1}\psi_i(t)|\Theta^{-1}\psi_j(t) > \tag{6.12}$$

and

$$\bar{\psi}_i = 2\psi_i(t) - \psi_i(t-\Delta t) - (\Delta t)^2\Theta^{-1}\frac{\delta E_{tot}(t)}{\delta\psi_i^*}. \tag{6.13}$$

Here all products involving Θ are matrix products among quantities stored in reciprocal space, therefore equation 6.3 is evaluated in reciprocal space.

Eq. 6.3 is solved iteratively [73]. If we decompose matrix B into Hermitian (B_h) and anti-Hermitian (B_a) parts,

$$B = B_h + B_a \tag{6.14}$$

it is straightforward to see that B_a vanishes in the limit of small Δt. In the first iteration $\lambda^{(0)}$ can thus be obtained from

$$\lambda^{(0)}B_h + B_h\lambda^{(0)} = 1 - A, \tag{6.15}$$

where the C-dependent term has been neglected because of higher order in Δt. Equation 6.15 can be solved exactly introducing the unitary matrix U, which diagonalizes B_h ($UB_hU = D$, where $D_{ij} = d_i\delta_{ij}$). The solution to Eq. 6.3 can be obtained by iterating

$$\lambda^{(n+1)}B_h + B_h\lambda^{(n+1)} = 1 - A - \lambda^{(n)}B_a - B_a^\dagger\lambda^{(n)} - \lambda^{(n)}C\lambda^{(n)}.$$

The parallelization of this algorhitm is quite straightforward, in fact only two parallel tasks are present: parallel matrix multiplication and parallel matrix diagonalization. Both operations are available in machine libraries of many vendors. Their interfaces however in many cases are different. Moreover we observed that, especially for the parallel diagonalization, in all tested cases, the data distribution required to obtain the highest performance changes with

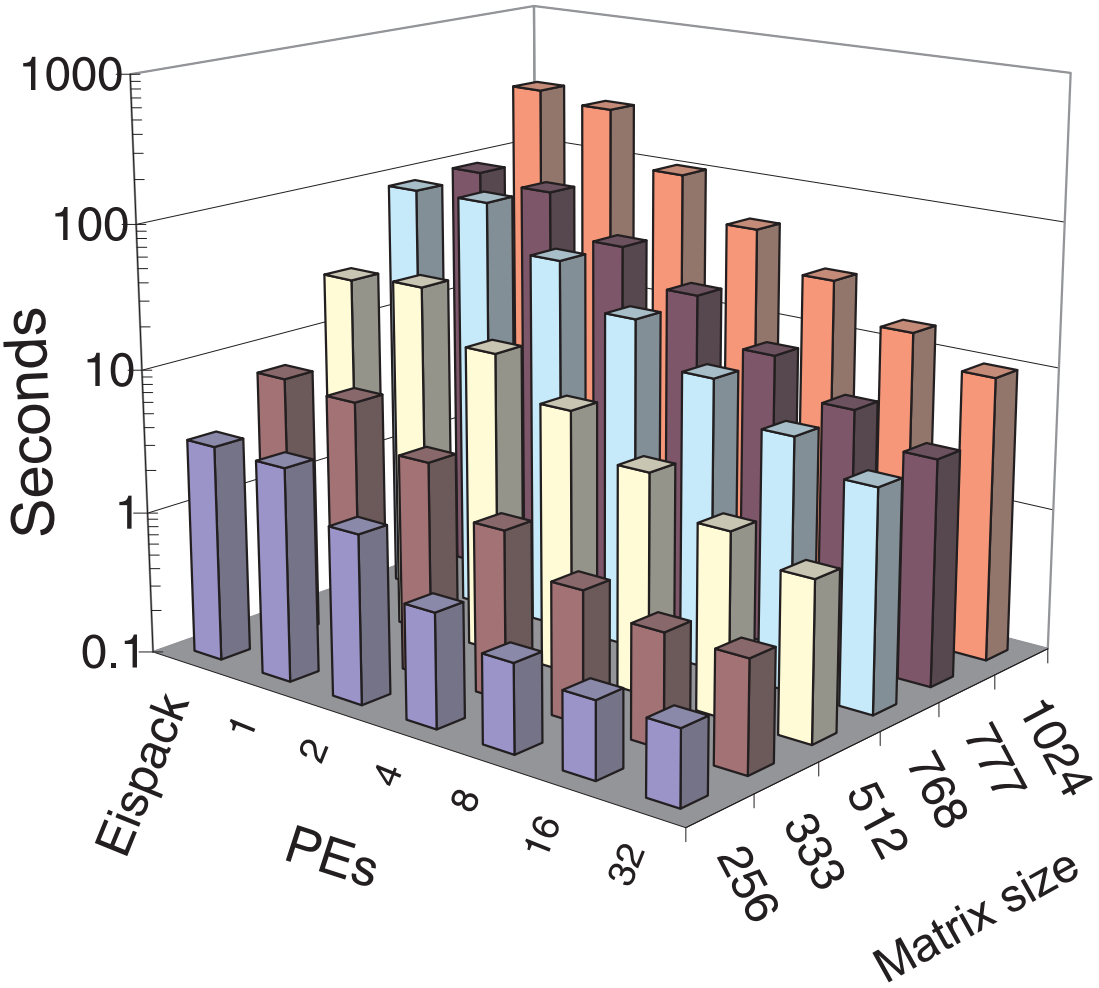

Figure 6.1: Parallel diagonalization routine execution time for different matrix sizes and number of processors, compared to the standard Eispack routine.

the number of processors. This is not acceptable, since, a part special cases, the required data distribution is not compatible with our fixed one. We decide, hence, to rewrite a parallel version of these two routines, working at a given data distribution. The overall performance of our routines are now slightly worse than that of the library routines with optimal data distribution, but dramatically better by considering our particular data distribution (the rows of a matrix are distributed with a blocking factor of one: the first row to the first processor, the second one to the second processor, and so on).

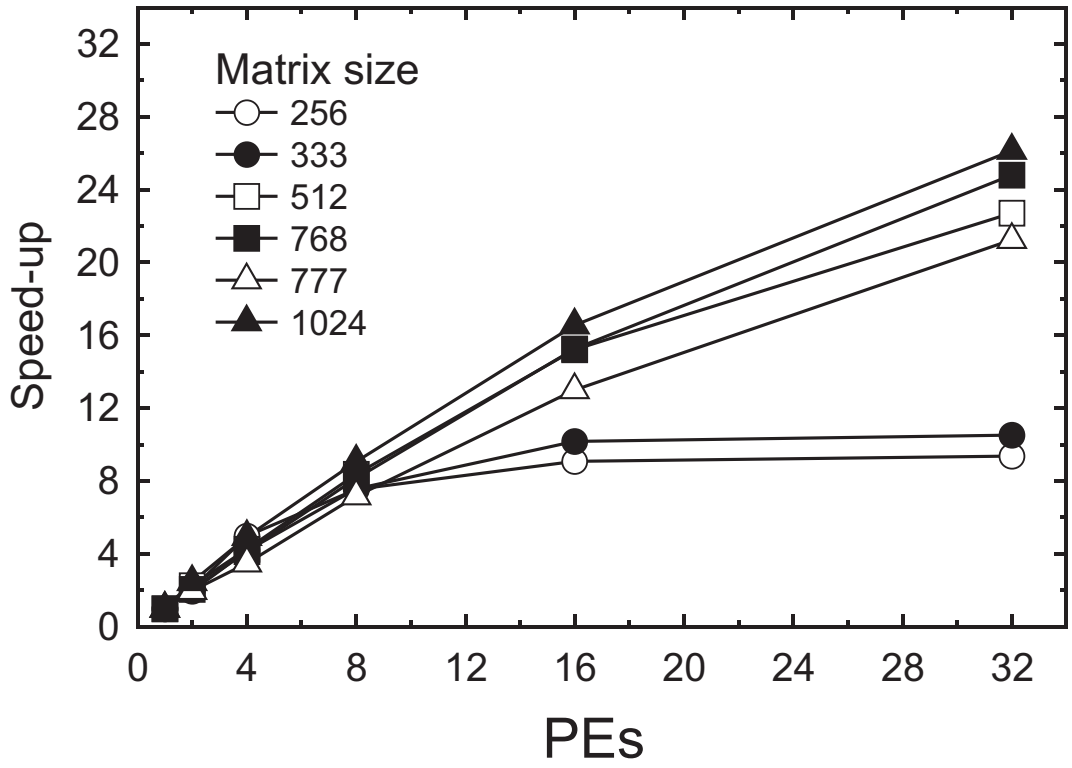

Figure 6.2: Parallel diagonalization routine speed-up for different matrix sizes and number of processors. When the ratio matrix size / number of processor is less than 16, the speed-up of the routine start saturating

For the practical implementation of the two algorithms we refer to reference [74]. Here we only point out that the matrix diagonalization has been implemented using the Householder algorhitm. In Fig. 6.1 the performance on a T3E600, of the diagonalization subroutine for different matrix sizes and different number of processors is compared with the standard scalar Eispack routine (the two codes have been compiled with the same compiler options). Note that the parallel routine running on a single processor has the same performance as the Eispack one.

In Fig. 6.2 the speed-up is shown [1] . This reveals that for each matrix size

[1] defined as $S_p = T_1/T_p$, with T_1 and T_p being the execution time on one and p processor respectively; sometime this definition is also known as the *algorithmic speed-up*, not to be confused with the *speed-up ratio* which compares the best possible scalar algorhitm with the parallel algorhitm.

there is a limit for the number of processors above which the routine speed-up saturates, due to the communication and synchronization overheads. The empirical role:

$$\frac{\text{matrix size}}{\text{number of processors}} < 16, \tag{6.16}$$

can be derived and has to be taken into account in choosing the number of processors for a particular run, in order to obtain optimal performance.

6.2 Code benchmarks

In this appendix code benchmarks on different architectures are presented and discussed.

In Fig. 6.3 we report the execution time of a molecular dynamics step as a function of the number of processors, while in Fig. 6.4 the correspondent speed-up is shown. The system considered is a super-cell (15, 19.5 and 15 atomic units) containing 16 ammonia molecules with an energy cut-off of 100 Ry., gradient corrections and pseudopotentials in the Kleinman-Bylander [24] form with s and p non-locality. At each time step the forces on atoms, on electrons and the stress on the cell have been calculated. The version of the code used for this benchmark does not include the *ad hoc* fast Fourier transform described in chapter 3, because that was implemented later.

Note that, apart the absolute speed which is dependent on the architecture, the speed-up is the same on all architectures tested. This demonstrates that our code is not only portable, but, most important, it does not loose in parallel performance from one architecture to another. Therefore, our implementation requirement to build an architecture-free parallel code is fulfilled.

The graph 6.4 also shows that the code speed-up is almost linear for a given

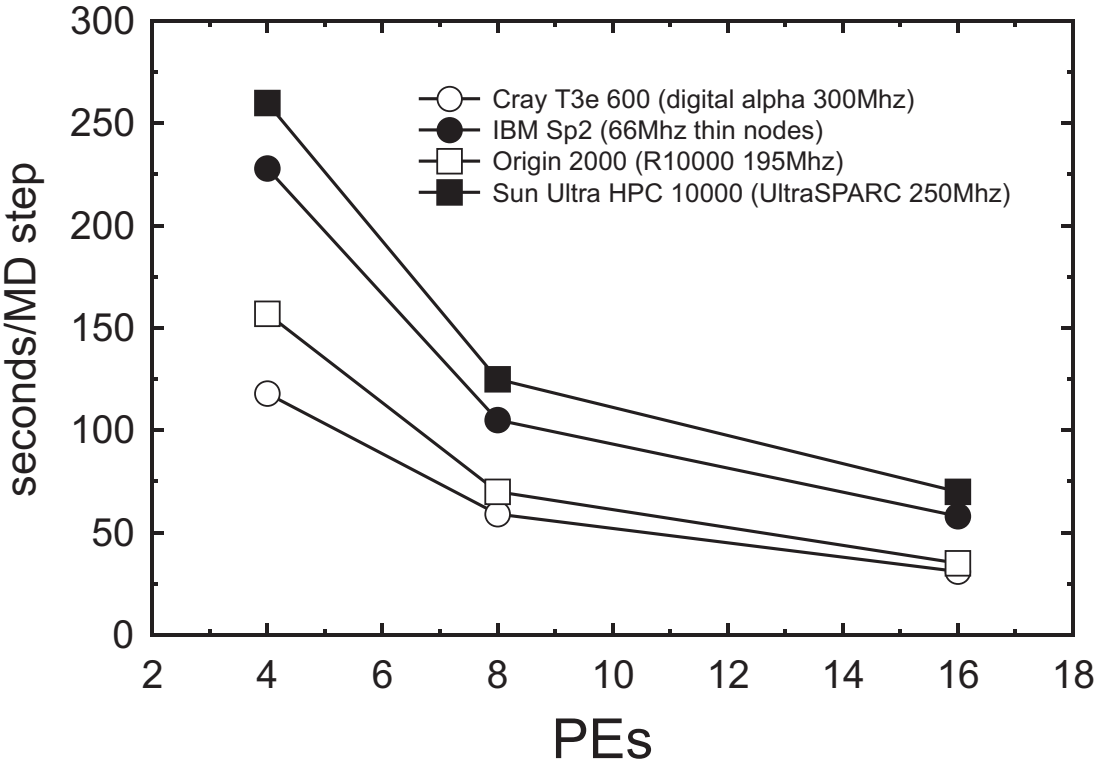

Figure 6.3: Benchmark of the code on different architectures, for the details on the system size used see text.

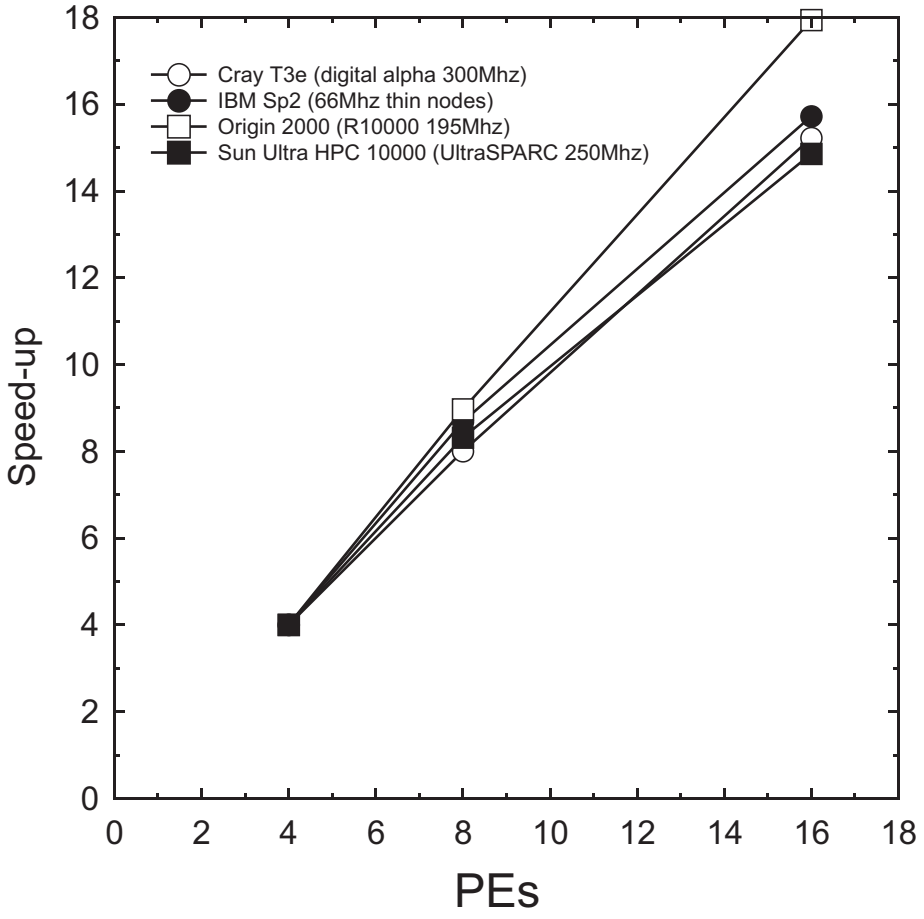

Figure 6.4: Code Speed-up (assuming the speed-up of 4 processors being 4) on different architectures.

problem in a wide range of number of processors, clear evidence of a good load balancing and an efficient implementation of the communications.

It is remarkable that in Fig. 6.4, for some architectures, the speed-up is super-linear. This apparent violation of the Amdahl's law [75] (well known law of parallel programming stating that the algorithmic speed-up of a code can never be super-linear because of communication overheads), is a consequence of the presence of caches on processors. In nowadays computers the importance of the cache is increasing and a good use of it could improve the speed of the code. While on a scalar computer little could be done a part for a careful writing

of the code, in a parallel computer the local size of the arrays can be changed by increasing the number of processors. In fact, as in our case, the reduction of the size of local arrays could reduce also the cache miss events, giving rise to a gain in computational speed greater than that lost in the communication overhead due to the larger number of processors.

Another important part of the computational work done on the code, is the effort devoted the code optimization, after its implementation. A careful analysis of the performances using both profiler system tools and timing routines has been carried out. This has helped us in tuning load balancing and communications, and in optimizing numerical algorithms. At the end of this work the execution time of the code decreased, on average, by more than 40% [76].

To conclude this section, we present in Figs. 6.5 and 6.6. our very last benchmark on T3E 1200 machine with the last revision of the code (including the *ad hoc* fast Fourier transform routine) The benchmark has been performed with a square super-cell (20x20x20 atomic units) containing 64 ammonia molecules, all other details are the same as for the previous benchmark. Note the high efficiency of the code (almost linear speed-up obtained using the same data for all numbers of PEs) in the whole range from 8 to 128 PEs.

6.3 Forces and Stress.

In this section we report the full expression of the forces on ions, electrons and cell (stress) as they are implemented in the scalar and parallel code (for a more detailed derivation and description of these quantities we address the reader to Ref. [3]). The computational effort needed to calculate the main contributions to these quantities is also reported.

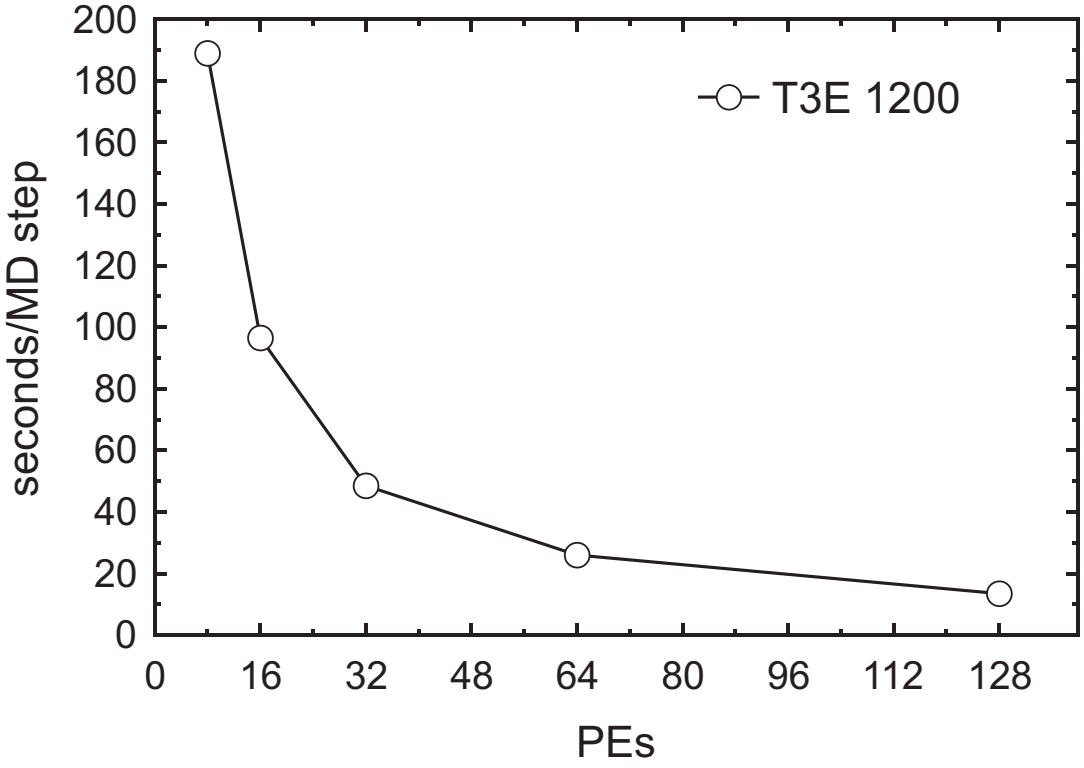

Figure 6.5: Execution time for a MD step, on Cray T3E 1200 machine.

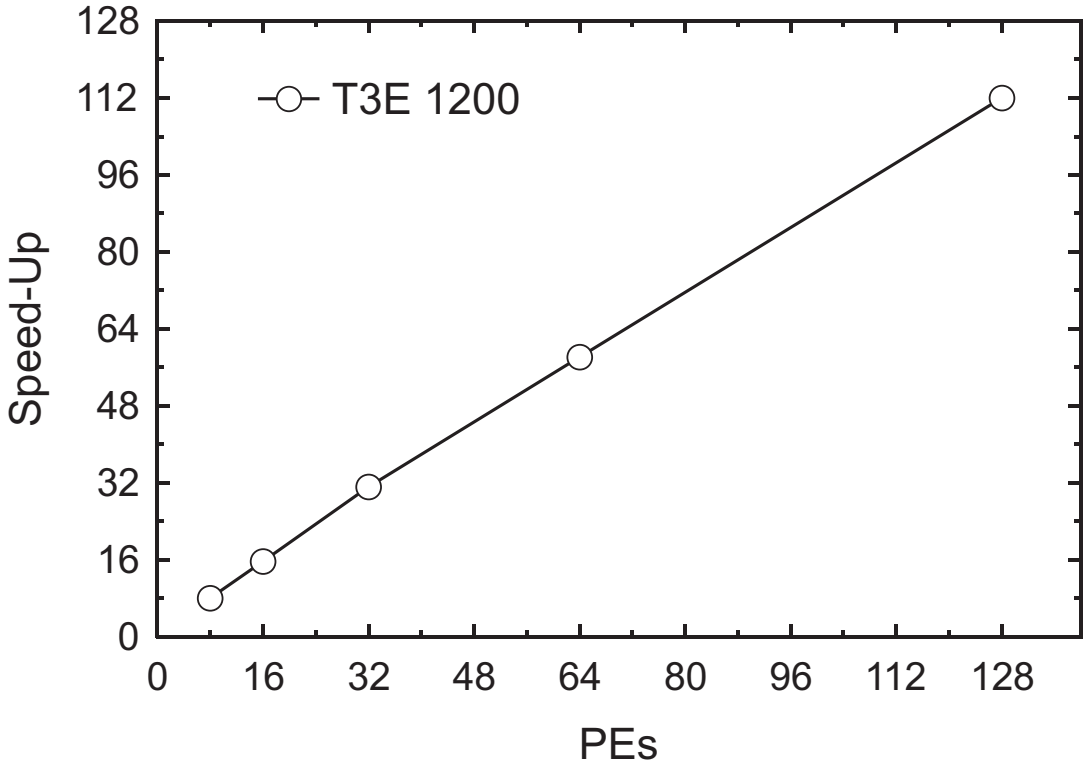

Figure 6.6: Code Speed-Up on Cray T3E 1200 machine (assuming the speed-up of 8 processors being 8).

Starting from ions, the expression of the force on ion I is:

$$F_I = -\frac{\partial E}{\partial \mathbf{R}_I} = \frac{\partial (E_{ke} + E_{xc} + E_{loc}^{ps} + E_{nl}^{ps} + E_H + E_{sr} - E_{self})}{\partial \mathbf{R}_I},$$

where

$$\frac{\partial (E_{ke} + E_{xc} - E_{self})}{\partial \mathbf{R}_I} = 0,$$

$$\begin{aligned}
\frac{\partial E_{loc}^{ps}}{\partial \mathbf{R}_I} &= \Omega \sum_{\mathbf{G}} -i\mathbf{G} e^{i\mathbf{G}\cdot\mathbf{R}_I} \rho_e^*(\mathbf{G}) v_{loc}(|\mathbf{G}|), \\
\frac{\partial E_{nl}^{ps}}{\partial \mathbf{R}_I} &= 2\,\mathrm{Re}\{\sum_{i=1}^{N_b} \sum_{l,m} f_i \alpha_{l,m} F_{I,i}^{l,m} \sum_{\mathbf{G}} (-i)\, \mathbf{G} e^{-i\mathbf{G}\cdot\mathbf{R}_I} c_i^*(\mathbf{G}) \left\langle \mathbf{G} | \delta v_{nl} \varphi_{l,m} Y_{l,m} \right\rangle\}, \\
\frac{\partial E_H}{\partial \mathbf{R}_I} &= \frac{4\pi\Omega}{2} \sum_{\mathbf{G}\neq\mathbf{0}} \rho_T^*(\mathbf{G}) i \frac{\mathbf{G} e^{-i\mathbf{G}\cdot\mathbf{R}_I}}{\mathbf{G}^2} \frac{Z_v}{\Omega} \exp\left[-\frac{R_c^2 \mathbf{G}^2}{4}\right] + c.c., \\
\frac{\partial E_{sr}}{\partial \mathbf{R}_I} &= -Z_v^2 \sum_{J\neq I}^{N} \left\{ \frac{\mathrm{erf\,c}\left(\frac{|\mathbf{R}_I - \mathbf{R}_J|}{R_c\sqrt{2}}\right)}{|\mathbf{R}_I - \mathbf{R}_J|^3} + \frac{\sqrt{2}}{R_c\sqrt{\pi}} \frac{\exp\left(-\frac{|\mathbf{R}_I - \mathbf{R}_J|^2}{2R_c^2}\right)}{|\mathbf{R}_I - \mathbf{R}_J|^2} \right\} (\mathbf{R}_I - \mathbf{R}_J).
\end{aligned}$$

The meaning of all quantities appearing in these expressions is reported in chapter 3. In the parallel code, the sums over the $\mathbf{G}$ vectors, of the first three expressions, are evaluated only over the $\mathbf{G}$ vectors of the local processor, while the arrays f_i, $\alpha_{l,m}$ and $\mathbf{R}_I$ are shared. In the fourth expression, the array $\mathbf{R}_J$ is temporarily distributed across the processors (with a blocking factor of one) and each processor sums only on its own $\mathbf{R}_J$. At the end of these sums each processor has only a partial value of the forces, then a global parallel sum of the N forces is performed. In table 6.1 the order of the number of operations required for the computation of the forces, on the scalar and parallel code are shown.

The Fourier components of the forces on the i electronic state are obtained from:

$$F_i(\mathbf{G}) = -\frac{\partial E}{\partial \boldsymbol{\psi}_i^*},$$

expanding E and calculating the derivatives one obtains:

$$\frac{\partial E_{self}}{\partial \boldsymbol{\psi}_i^*} = 0,$$

	Scalar Complexity	Parallel Complexity
$\partial E_{loc}^{ps}/\partial \mathbf{R}_I$ and $\frac{\partial E_H}{\partial \mathbf{R}_I}$	$N \cdot N_g$	$N \cdot N_g/N_p$
$\partial E_{nl}^{ps}/\partial \mathbf{R}_I$	$N \cdot N_b \cdot N_{gw}$	$N \cdot N_b \cdot N_{gw}/N_p$
$\partial E_{sr}/\partial \mathbf{R}_I$	$N \cdot N$	$N \cdot N/N_p$
communications		$N \cdot N_p \log N_p$

Table 6.1: Computational complexity for the determination of the Forces on the atoms. N is the number of atoms, N_b the number of electronic states, N_{gw} and N_g the number of $\mathbf{G}$ vectors up to E_c and $4E_c$ respectively, and N_p the number of processors.

$$
\begin{aligned}
\frac{\partial E_{ke}}{\partial \boldsymbol{\psi}_i^*} &= \frac{1}{2} f_i \mathbf{G}^2 c_i(\mathbf{G}), \\
\frac{\partial E_H}{\partial \boldsymbol{\psi}_i^*} &= 4\pi f_i \sum_{\mathbf{G}' \neq 0} \frac{\rho_T(\mathbf{G}')}{\mathbf{G}'^2} c_i\left(\mathbf{G}-\mathbf{G}'\right), \\
\frac{\partial E_{xc}}{\partial \boldsymbol{\psi}_i^*} &= FFT\left\{\frac{\partial E_{xc}}{\partial \boldsymbol{\psi}_i^*}(r) = f_i\left[\epsilon_{xc}(\mathbf{r}) + \frac{\partial \epsilon_{xc}}{\partial \rho_e(\mathbf{r})}\rho_e(\mathbf{r})\right]\boldsymbol{\psi}_i(r)\right\}, \\
\frac{\partial E_{loc}^{ps}}{\partial \boldsymbol{\psi}_i^*} &= f_i \sum_{\mathbf{G}'} S\left(\mathbf{G}'\right) v_{loc}(\left|\mathbf{G}'\right|) c_i\left(\mathbf{G}-\mathbf{G}'\right), \\
\frac{\partial E_{nl}^{ps}}{\partial \boldsymbol{\psi}_i^*} &= f_i \sum_I \sum_{l,m} \alpha_{l,m} F_{I,i}^{l,m} e^{-i\mathbf{G}\cdot\mathbf{R}_I} \left\langle \mathbf{G} | \delta v_{nl} \varphi_{l,m} Y_{l,m} \right\rangle.
\end{aligned}
$$

In both codes, to calculate the contributions from E_H, E_{xc} and E_{loc}^{ps}, the Hartree potentials and the local part of the pseudopotentials are calculated in reciprocal space and transformed in real space to be added to the exchange and correlation potentials. Then each wave-function is transformed in real space, multiplied by the potentials and the result ($\partial\left(E_H + E_{xc} + E_{loc}^{ps}\right)/\partial\boldsymbol{\psi}_i^*$) is transformed back in reciprocal space. The computational complexity for the determination of all the Fourier components of all the electronic states is shown in table 6.2. Note that contrary to the case of the forces on ions, where each processor calculates only a part of the total force, here each processor calculates the full force of the Fourier components relative to its $\mathbf{G}$ vectors. No additional global parallel sum is needed.

An explicit derivation of the stress components has been carried out by

	Scalar Complexity	Parallel Complexity
$\partial\left(E_H + E_{xc} + E_{loc}^{ps}\right)/\partial\boldsymbol{\psi}_i^*$	$2N_g + N_b N_x N_y N_z$ $+2N_b$ FFT	$(2N_g + N_b N_x N_y N_z)/N_p$ $+2N_b$ parallel FFT
$\partial E_{nl}^{ps}/\partial\boldsymbol{\psi}_i^*$	$N \cdot N_b \cdot N_{gw}$	$N \cdot N_b \cdot N_{gw}/N_p$
$\partial E_{ke}/\partial\boldsymbol{\psi}_i^*$	$N_b \cdot N_{gw}$	$N_b \cdot N_{gw}/N_p$
communications		$2N_b$ comm. within FFT

Table 6.2: Computational complexity for the determination of all the Fourier component of all the electronic states. Symbols as in Tab. 6.1

Focher *et al.* in the case of both norm-conserving and ultra-soft pseudopotentials. Here we report only the expression of the stress components for the norm-conserving case. As already shown (Chapter 2), the stress tensor is defined as:

$$\Pi = -\frac{1}{\Omega}\frac{\partial E}{\partial \mathbf{h}}\mathbf{h}^t,$$

with:

$$\begin{aligned}
\frac{\partial E_{ke}}{\partial h_{\alpha\beta}} &= -\sum_{i=1}^{N_b} f_i \sum_{\mathbf{G}} G_\alpha G_\gamma \left(\mathbf{h}^t\right)_{\gamma\beta}^{-1} c_i^*\left(\mathbf{G}\right) c_i\left(\mathbf{G}\right), \\
\frac{\partial E_{xc}}{\partial h_{\alpha\beta}} &= \left\{\int d\mathbf{r}\left[\epsilon_{xc}(\rho_e(\mathbf{r})) - v_{xc}(\mathbf{r})\right]\rho_e(\mathbf{r})\right\}\left(\mathbf{h}^t\right)_{\alpha\beta}^{-1}, \\
\frac{\partial E_{loc}^{ps}}{\partial h_{\alpha\beta}} &= -\Omega\sum_{\mathbf{G}} S\left(\mathbf{G}\right)\rho_e^*(\mathbf{G})\left[2\frac{\partial v_{loc}(|\mathbf{G}|)}{\partial G^2}G_\alpha G_\gamma + v_{loc}(|\mathbf{G}|)\delta_{\alpha\gamma}\right]\left(\mathbf{h}^t\right)_{\gamma\beta}^{-1}, \\
\frac{\partial E_H}{\partial h_{\alpha\beta}} &= \left[-E_H\delta_{\alpha\gamma} + 4\pi\Omega\sum_{\mathbf{G}\neq\mathbf{0}}\frac{\rho_T^*(\mathbf{G})}{\mathbf{G}^2}\left(\frac{\rho_T(\mathbf{G})}{\mathbf{G}^2} + \frac{1}{2}\rho_{ion}(\mathbf{G})R_c^2\right)G_\alpha G_\gamma\right]\left(\mathbf{h}^t\right)_{\gamma\beta}^{-1}, \\
\frac{\partial E_{sr}}{\partial h_{\alpha\beta}} &= -\frac{1}{2}Z_v^2\left[\sum_I^N\sum_{J\neq I}^N\left\{\frac{\operatorname{erf c}\left(\frac{|\mathbf{R}_I-\mathbf{R}_J|}{R_c\sqrt{2}}\right)}{|\mathbf{R}_I-\mathbf{R}_J|^3} + \frac{\sqrt{2}}{R_c\sqrt{\pi}}\frac{\exp\left(-\frac{|\mathbf{R}_I-\mathbf{R}_J|^2}{R_c\sqrt{2}}\right)}{|\mathbf{R}_I-\mathbf{R}_J|^2}\right\}\right] \\
&\quad \left(\mathbf{R}_I^\alpha - \mathbf{R}_J^\alpha\right)\left(\mathbf{R}_I^\gamma - \mathbf{R}_J^\gamma\right)\left(\mathbf{h}^t\right)_{\gamma\beta}^{-1}, \\
\frac{\partial E_{nl}^{ps}}{\partial h_{\alpha\beta}} &= 2\sum_{i=1}^{N_b} f_i \sum_{l,m}\alpha_{l,m}\sum_I \mathrm{Re}\left[\frac{\partial\left(F_{I,i}^{l,m}\right)^*}{\partial h_{\alpha\beta}}F_{I,i}^{l,m}\right]
\end{aligned}$$

with

$$\frac{\partial\left(F_{I,i}^{l,m}\right)^*}{\partial h_{\alpha\beta}} = \sum_{\mathbf{G}}(-i)^l c_i^*\left(\mathbf{G}\right)e^{-i\mathbf{G}\cdot\mathbf{R}_I}\frac{4\pi}{\Omega}$$

	Scalar Complexity	Parallel Complexity
$\partial E_{ke}/\partial h_{\alpha\beta}$	$N_b \cdot N_{gw}$	$N_b \cdot N_{gw}/N_p$
$\partial E_{xc}/\partial h_{\alpha\beta}$	$N_x N_y N_z$+FFT	$N_x N_y N_z/N_p$+parallel FFT
$\partial E^{ps}_{loc}/\partial h_{\alpha\beta}and\partial E_H/\partial h_{\alpha\beta}$	N_g	N_g/N_p
$\partial E_{sr}/\partial h_{\alpha\beta}$	$N \cdot N$	$N \cdot N/N_p$
$\partial E^{ps}_{nl}/\partial h_{\alpha\beta}$	$N \cdot N_b \cdot N_{gw}$	$N \cdot N_b \cdot N_{gw}/N_p$
communications		comm. within FFT + $N_p \log N_p$

Table 6.3: Computational complexity for the determination of each of the nine components of the stress. Symbol as in Tab. 6.1

$$\left[\left(\frac{\partial Y_{l,m}}{\partial h_{\alpha\beta}} - \frac{1}{2} Y_{l,m}\left(\mathbf{h}^t\right)^{-1}_{\alpha\beta}\right)\int dx x^2 \varphi_{l,m}(x)\, j_l\left(|\mathbf{G}|\, x\right) + Y_{l,m}\int dx x^2 \varphi_{l,m}(x)\, \frac{\partial j_l\left(|\mathbf{G}|\, x\right)}{\partial h_{\alpha\beta}}\right].$$

Like in the previous cases, in the parallel code, all sums over $\mathbf{G}$ vectors are taken only on the local $\mathbf{G}$ vectors. To evaluate the fifth term ($\partial E_{sr}/\partial h_{\alpha\beta}$), as for the ions, position vectors are distributed. The total stress components are then obtained with a global parallel sum. The computational complexity for each of the nine components of the stress is shown in table 6.3.

Acknowledgments

I would like to thank my supervisors Dr. Guido Chiarotti and Dr. Sandro Scandolo for having introduced me to the exciting world of molecular dynamics simulations, and for constantly reminding me that these tools are aimed also at understanding physics and not only at playing with computers.

Thanks also to Prof. Erio Tosatti, a constant enlightening guide, for his precious suggestions and for his famous stimulating discussions.

The part of the work concerning water was made possible thank to the collaboration with Prof. Michele Parrinello and Dr. Marco Bernasconi, with whom I am really indebted.

I wish to thank also Francesco Ancilotto for the data on methane, Riccardo Valente for useful suggestions, at the beginning of the work, on the parallel code, and Stefano Cozzini for the help in the code optimization and kind hospitality at CINECA.

Many other nice guys not directly involved into this work, I would like to thank for having made these three years of hard work at Sissa pleasant and less heavy. It was a pleasure for me to collaborate with Alessandro Laio, Stefano Serra, Stefan Bernars and Francesco (Franz) Di Tolla. I enjoyed the days with my colleagues and flatmates Claudio Tebaldi, Daniele Passerone, Marco Saitta, Lorenzo Desantis, Stefano Martinelli and Ivan Arisi.

Finally, but not least, I thank my parents, Loredana Garuti and Luciano

Cavazzoni, and my girlfriend, Roberta Tagliagambe, for their support and understanding during these three years.

Bibliography

[1] F. Ancilotto,G. L. Chiarotti, S. Scandolo, and E. Tosatti, Science **275**, 1288 (1997).

[2] P. Focher *et al.*, Europhys. Lett. **36**, 345-351 (1994); M. Bernasconi *et al.*, J. Phys. Chem. Solids, **56**, 510 (1995).

[3] P. Focher and G. L. Chiarotti, in *Progress in Computational Physics of Matter*, ed. by L. Reatto and F. Manghi (World Scientific, 1997); P. Focher, *PhD Thesis*, International School for Advanced Studies - Trieste (1994).

[4] R. Car and M. Parrinello, Phys. Rev. Lett. **55**, 2471 (1985).

[5] M. Parrinello and A. Rahman, Phys. Rev. Lett. **45**, 1196 (1980).

[6] H.C. Andersen, J. Chem. Phys. **72**, 2384 (1980).

[7] M. Parrinello, in *Molecular Dynamics Simulations of Statistical-Mechanical Systems*, ed. by G. Ciccotti and W. G. Hoover (North-Holland, 1986).

[8] J.R. Ray and A. Rahman, J. Chem. Phys. **80**, 4423 (1984).

[9] M. Parrinello in *Molecular-Dynamics Simulations of Statistical-Mechanical System*, Proceedings of the international school of physics

"Enrico Fermi", 204, ed. G. Ciccotti and W. G. Hoover, North-Holland (1986).

[10] R. Car and M. Parrinello, in *Simple Molecular Systems at Very High Density* (Plenum Publishing Corp., 1989) p. 455.

[11] D.K. Remler and P.A. Madden, Mol. Phys. **70**, 921 (1990).

[12] G. Galli and A. Pasquarello, in *Computer Simulation in Chemical Physics*, ed. M.P Allen and D.J. Tildesley (Kluwer Acedemic Publisher, 1993), p.261.

[13] P. C. Hohenberg and W. Kohn, Phys. Rev. **136** B864 (1964).

[14] W. Kohn and L. J. Sham, Phys. Rev. **140**, A1133 (1965).

[15] W. Kohn and P. Vashishta, in *Theory of the Inhomogeneous Electron Gas*, ed. S. Lundqvist and N. H. March, Plenum Publishing Corp., New York (1983).

[16] G. Galli and M. Parrinello in *Computer Simulation in Material Science*, edited by M. Meyer and V. Pontikis (Kluwer, Dordrecht, 1991).

[17] G. Pastore, E. Smargiassi, and F. Buda, Phys. Rev. A, **44**, 6334 (1991).

[18] S. Nosé, Mol. Phys. **52**, 255 (1984).

[19] P. E. Blöchl and M. Parrinello, Phys. Rev. B **45**, 9413 (1992).

[20] O.H. Nielsen and R.M. Martin, Phys. Rev. Lett. **50**, 697 (1983).

[21] O.H. Nielsen and R.M. Martin, Phys. Rev. B **32**, 3780 (1985).

[22] M. Bernasconi, G.L. Chiarotti, P. Focher, S. Scandolo, E. Tosatti, and M. Parrinello, J. Phys. Chem. Solids 56, 501 (1995).

[23] P. Gomes Dacosta, O.H. Nielsen and K. Kunc, J. Phys. C **19**, 3163 (1986).

[24] L. Kleinman e D. M. Bylander, Phys. Rev. Lett. **48**, 1425 (1982).

[25] J. Wiggs and H. Jónsson, Comput. Phys. Commun. **81**, 1 (1994).

[26] J. Wiggs and H. Jónsson, Comput. Phys. Commun. **87**, 1 (1994).

[27] L. J. Clarke, I. Stich and M.C. Payne, Comput. Phys. Commun. **72**, 14 (1992).

[28] J. S. Nelson, S. J. Plimpton and M. P. Sears, Phys. Rev. **B 47**, 1765 (1993).

[29] S. de Gironcoli, private comunication of a benchmark with the parallel plane-wave code developed at SISSA by himself et.al. .

[30] A. Geist, A. Beguelin, J. Dongarra, W. Jiang, R. Mancheck and V. Sunderam, in *PVM: Parallel Virtual Machine*, (The MIT Press, 1994).

[31] Message Passing Interface Forum, *Mpi: A message passing interface standard*, Computer Science Dept. Techmical Report CS-94-230, (University of Tennessee 1994).

[32] P.V. Hobbs, *Ice Physics* (Clarendon, Oxford, 1974).

[33] M. Benoit, M. Bernasconi, P. Focher, and M. Parrinello, Phys. Rev. Lett. **76**, 2934 (1996).

[34] M. Benoit, D. Marx and M. Parrinello, Nature **392**, 258 (1998); M. Bernasconi, P.L. Silvestrelli and M. Parrinello, Phys. Rev. Lett., **81**, 1253 (1998).

[35] M. Gauthier, Ph. Pruzan, J. C. Chervin and J. M. Besson, Phys. Rev. **B 37**, 2102 (1988).

[36] J. W. Otto, R. F. Porter and A. L. Ruoff, J. Phys. Chem. Solids **50**, 171 (1989).

[37] T. Kume, M. Daimon, S. Sasaki and H. Shimizu, Phys. Rev. **B 57**, 13347 (1998).

[38] J. S. Loveday, R. J. Nelmes, W. G. Marshall, J. M. Besson, S. Klotz, and G. Hamel, Phys. Rev. Lett. **76**, 74 (1996).

[39] W. B. Hubbard *et al.*, in *Neptune and Triton*, D. P. Cruikshank, Ed. (Univ. of Arizona Press, Tucson, 1995).

[40] W. B. Hubbard, Science **214**, 145 (1980).

[41] N. F. Ness *et al.*, Science **233**, 85 (1986); *ibidem* **246**, 1473 (1989).

[42] R. L. Kirk and D. J. Stevenson, The Astroph. J. **316**, 836 (1987).

[43] W. J. Nellis, D. C. Hamilton, N. C. Holmes, H. B. Radousky, F. H. Ree, A. C. Mitchell and M. Nicol, Science **240**, 779 (1988).

[44] D. J. Stevenson, Rep. Progr. Phys. **46**, 555 (1983).

[45] W. J. Nellis, N. C. Holmes, A. C. Mitchell, D. C. Hamilton, and M. Nicol, J. Chem. Phys. **107**, 9096 (1997).

[46] W. B. Hubbard, W. J. Nellis, A. C. Mitchell, N. C. Holmes, S. S. Limaye, and P. C. McCandless, Science **253**, 648 (1991).

[47] A. C. Mitchell and W. J. Nellis, J. Chem. Phys. **76**, 6273 (1982).

[48] M. Sprik *et al.*, J. Chem. Phys. **105**, 1142 (1996).

[49] N. Troullier and J. L. Martins, Phys. Rev. **B 43**, 1993 (1991).

[50] A.D. Becke, Phys. Rev. **A 38**, 3098 (1988).

[51] C. Lee, W. Yang, and R. G. Parr,Phys. Rev. **B 37**, 785 (1988).

[52] H. Arstila, K. Laasonen and A. Laaksonen, J. Chem. Phys. **B 108**, 1031 (1998).

[53] R. LeSar, J. Chem. Phys. **86**, 1485 (1987).

[54] M.Bernasconi, M.Parrinello, G.L.Chiarotti, P.Focher, and E.Tosatti Phys. Rev. Lett., **76**, 2081 (1996).

[55] P. Demontis, R.L. LeSar, and M. L. Klein, Phys. Rev. Lett. **60**, 2284-2287 (1988).

[56] J.P. Hansen and I.R. Donald, *Theory of Simple Liquids*,(Academic Press, 1976).

[57] R. D. King-Smith and D. Vanderbilt, Phys. Rev. **B 47**, 1651 (1993).

[58] R. Resta, Rev. Mod. Phys. **136** 51 (1992).

[59] P. L. Silvestrelli, M. Bernasconi and M. Parrinello, Chem. Phys. Lett. **277**, 478 (1997).

[60] H. B. Radousky, A. C. Mitchell, and W. J. Nellis, J. Chem. Phys. **93**, 8235 (1990).

[61] G. A. Lyzenga, T. J. Ahrens, W. J. Nellis and A. C. Mitchell, J. Chem. Phys. **76**, 6282 (1982).

[62] M. Bernasconi, P.L. Silvestrelli, and M. Parrinello, P. R. L. **81**, 1235 (1998).

[63] R.J. Hemley *et al.*, Nature **330**, 737 (1987).

[64] L.g. Liu, Earth planet. Sci. Lett. **61**, 359 (1982).

[65] K. R. Hirsch and W. B. Holzapfel, Phys. Lett. **101 A**, 142 (1984); Ph. Pruzan *et al.*, J. Chem. Phys. **99**, 9842 (1993); K. Aoki *et al.*, Phys. Rev. Lett. **76**, 784 (1996); A. F. Goncharov *et al.*, Science **273**, 218 (1996), and reference therein.

[66] F. Datchi, P. Loubeyre and R. LeToullec, Review of High Pressure Science and Technology **7**, 778 (1998).

[67] W. B. Hubbard and J. J. MacFarlane, J. Geophys. Research **85**, 225 (1980).

[68] The isentropes of Uranus and Neptune are believed to be very similar [46, 77].

[69] W. B. Hubbard, Science **275**, 1279 (1997), W.B. Hubbard, private comunication.

[70] H.C. Andersen, J. of Comput. Phys. **52**, 24 (1983).

[71] F. Tassone, F. Mauri and R. Car, Phys. Rev. B, **50** 10561 (1994).

[72] J. Ryckaert, G. Ciccotti and H.J.C. Berendsen, J. of Comput. Phys. **23**, 24 (1977).

[73] K. Laasonen, A. Pasquarello, R. Car, C. Lee and D. Vanderbilt, Phys. Rev. B **47**, 10142 (1993).

[74] T.L. Freeman and C. Phillips, *Parallel Numerical Algorithms*,(Prentice Hall 1992).

[75] G.M. Amdahl, AFIPS conf. Proc. Spring Jt. Conf. **30**, 483 (1967).

[76] C. Cavazzoni, Cineca Reports (1997).

[77] M. Podolak, A. Weizman, and M. Morley, Planet. Space Sci. **43**, 1517 (1995).